Università degli studi di Roma ”Tor Vergata”

Facoltà di Scienze Matematiche Fisiche e Naturali

Physics Ph.D. Thesis

Measurement of the Beam asymmetry in Deuteron Photodisintegration at GRAAL

Candidato:
Dott. Domenico Franco

Relatori:
Prof. A. D’Angelo

Anno Accademico 2006-2007

Contents

Chapter 1

The Deuteron Photodisintegration

1.1 Introduction

The deuteron, the only $A = 2$ nucleus, provided for many years the simplest microscopic system to test the conventional nuclear model, a framework in which nuclei and nuclear interactions are explained as baryon interacting through the exchange of mesons. More recently with the new available high duty cicle and large solid angle facilities it became an interesting "laboratory" to test modern QCD theories. Due to the small binding energy of the proton and neutron inside this nucleus ($E \sim 2.3\ MeV$), deuteron photodisintegration represents the simplest nuclear reaction induced by photons.

1.2 The deuteron

Deuteron photodisintegration was first investigated in the early 1930s, in order to understand the structure of the neutron. After the discovery of the neutron by James Chadwick, attention turned to its mass and structure. Was the neutron a fundamental particle, like the proton and the electron? Was it a bound state of the proton and the electron, different from the hydrogen atom? How were the electrons confined into the small nuclear volume? The experimental evidence on the neutron mass prevented a solution of the issue until 1934, when Chadwick and Goldhaber used deuteron photodisintegration [1] to determinate that the neutron mass was slightly heavier than that of the hydrogen atom. Thus, the neutron, being heavier than the proton plus electron system confinated, was a fundamental particle and there was no longer any basis for thinking that electrons could be present in nuclei [2].

Subsequently simple analysis of deuteron properties provided many information about strong interaction in nuclei. For example the non-additivity of the magnetic moment of the proton and of the neutron inside the deuteron and its small quadrupole moment, proved that in strong N-N interaction tensorial contributions must be considered over the dominant central interactions.

Information about the nature of strong interactions can be obtained also from scattering experiment in which a probe strikes a deuteron target. Investigation of the p-n bound state with the smaller perturbation possible, qualifies electromagnetic probes (photons or electrons) as the best candidates. The electromagnetic interaction is proportional to the fine-structure constant ($\alpha \sim 1/137$) that is much smaller than the strong interaction coupling constant. Moreover the interaction between an electromagnetic probe and an hadronic target may be summarised by the relation:

$$H_{in} = A_\mu J^\mu \tag{1.1}$$

where A_μ is the electromagnetic 4-potential, well known from the QED theory, and J^μ is the hadronic current in which we are interested to investigate. The unknown hadronic system is the subject of many theoretical models.

1.3 About theory

At present several models of a deuteron as a NN bound state, of deuteron wave function, of its form factors and of the electro or photodisintegration, exist. Many of this models are very complex and their adequate description would require a specific work which is out of the aim of this work. However a very short outlook of the state of art is here presented.

1.3.1 Theories with mesons-baryons degrees of freedom

There have been many attempts to understand low energy deuteron photodisintegration using a conventional meson-baryon framework. Since the Δ resonance is the only nucleon excited state accessible by photons having energy lower than 400 MeV it makes sense to describe the process below 400 MeV using a model of coupled NN, $N\Delta$ and $NN\pi$ channel. Laget [3] showed that the prominent peak in the total cross section (fig:1.3) at $E_\gamma = 300$ MeV can be largely explained by the mechanism in which a Δ resonance is photoproduced on a nucleon followed by the reabsorption of its decaying pion by the other nucleon 1.1(a). He also examined many other mechanism, including rescattering up to second order, but he did not do a full calculation of the final-state interaction. Later Leideman and Arenhövel [4] treated the NN, $N\Delta$ and $\Delta\Delta$ as coupled channels and included final-state effects to all orders. Tanabe and Ohta [5] continued on this idea with a more complete treatment of the final state. In a number of conference talks, Lee [6] reported on a coupled channel calculation using N, Δ and the $P_{11}(1440)$ resonances, and he extended the incoming photon energy range up to $E_\gamma = 2$ GeV (AMEC). His work suggests that the final-state interactions significantly enhance the cross section for photon energies above 1 GeV.

A recent calculation by Schwamb, Arenhövel and collaborators [7] include NN, $N\Delta$ and πd channels, and also contributions from meson retardation, meson exchange current, and the meson dressing of the nucleon current required by unitarity. All parameters are fixed from nucleon-nucleon or π-nucleon scattering and photoreactions such as Δ-excitation from the nucleon, so that no new parameters are introduced into the calculation of the deuteron photodisintegration process itself. A reasonable description of NN scattering up to lab energies of 800 MeV, particularly for the important ${}^1D_2$ partial wave. The authors emphasise that the consistent inclusion of the meson retardation effects improve their results for photodisintegration.

By comparison to the detailed and careful treatment developed for lower energies, calculations specifically designed to describe higher energy photodisintegration are less complete. An unpublished Bonn calculation [8] includes pole diagrams generated from π, ρ, η and ω exchange 1.1(f)-1.1(g), plus the 17 well-established nucleon and Δ resonances with masses less than 2 GeV and $J \leq 5/2$. The calculation uses resonance parameters taken from the Particle data Group.

Nagornyi and collaborators [11], [12] have introduce a covariant model based on the sum of pole diagrams. The latest version [12] gives the photodisintegration amplitude as a sum of contributions only from 4 Feynman diagrams: three pole diagrams coming from the coupling of the photons to the three external legs of covariant dpn vertex plus a contact interaction designed to maintain gauge invariance. This model divides the dpn vertex into "soft" and "hard" parts, with the hard part designed to reproduce the pQCD counting rules (see par 1.3.2) and its strength is determined by a fit to the data at 1 Gev. The model has no final-state interactions or explicit nucleon resonance contributions. There is also a relativistic calculation of the photodisintegration in Born approximation using Bethe-Salpeter formalism [13]. It is found that the cross section is a factor of 2 to 10 times are too small, and that relativistic effects are large.

All of these models are rather crude, and taken together it is not clear what on should conclude of them. Each calculations to emphasises some aspects of what a comprehensive meson-baryon theory of photodisintegration should entail We may say that conventional calculations that neglect final-state interactions seriously underestimate the cross section, but they may be corrected in an approximate manner by introducing diagrams with pole in the s-channel More generally the introduction of pole diagrams may also insure that meson-baryon theory of deuteron photodisintegration has the correct high energy behavior [14].

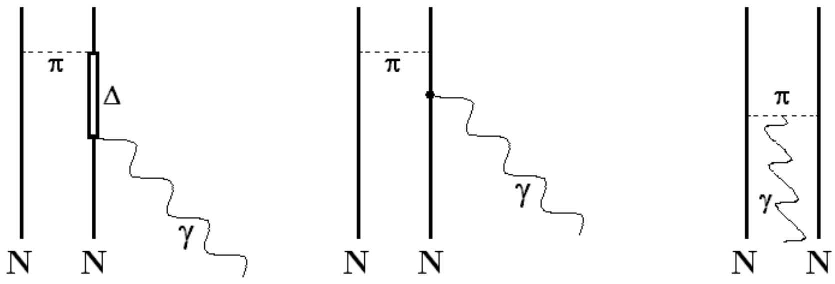

(a) Delta current (b) Meson exchange current (c) Meson exchange current

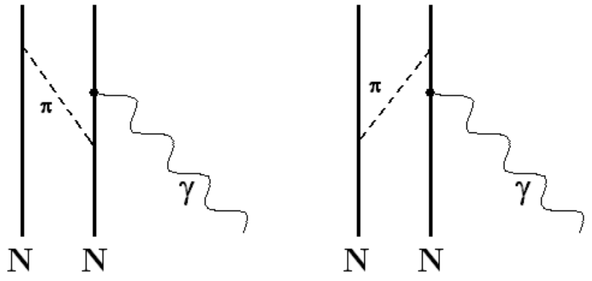

(d) Recoil current (e) Recoil current

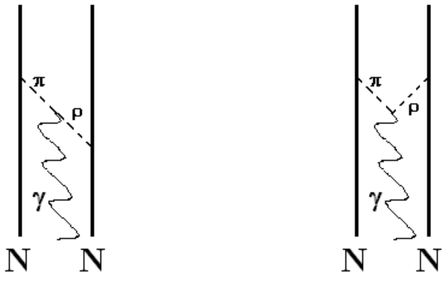

(f) heavy meson exchange (g) heavy meson exchange

Figure 1.1: Typical diagrams using for the deuteron photodisintegration cross section calculations

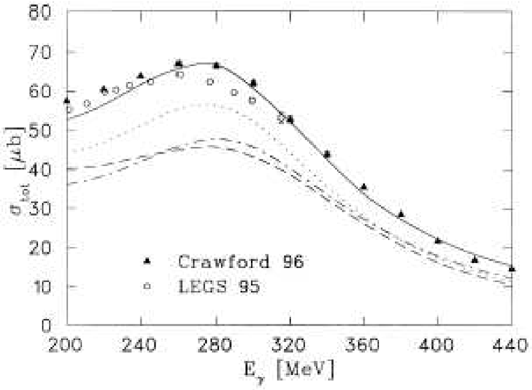

Figure 1.2: Total cross section for $\gamma, d \rightarrow p, n$ as a function of photon energy E_γ in comparison with experiment [9], [10]. Dashed: static calculation of Arenhövel et al. Dotted: static OBEPR-calculation in the meson retardation approach; dash-dot: retardation switched on in the hadronic part only, but static MECs; full: complete calculation including πd-channel and $\rho\pi\gamma/\omega\pi\gamma-$MECs.

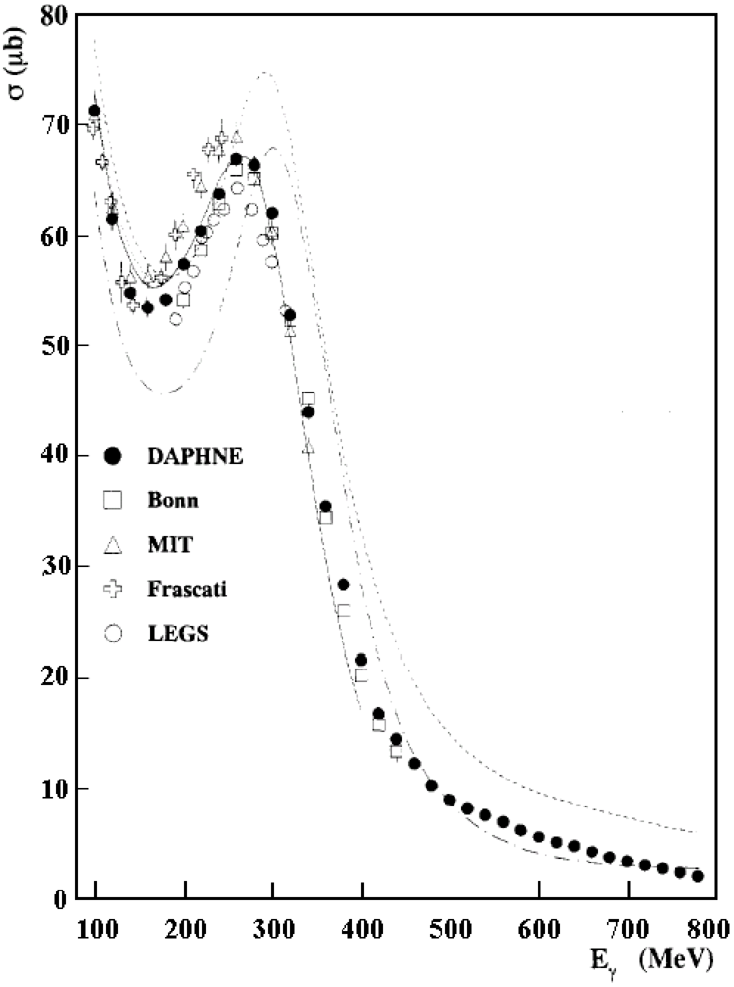

Figure 1.3: The deuteron photodisintegration total cross section. Theoretical calculation are: Arenhövel calculation (dashed line); the diagrammatical approach of Laget (dot-dashed line). Data are from [9], [10],

1.3.2 Theories with quarks degrees of freedom

Calculation based on quark degrees of freedom must take into account the fact that the deuteron is at least a six quark system. If the six quarks are considered identical particles (taking into account internal symmetries) the system must be antisymmetrized, and it is not clear that one nucleon should retain its identity in presence of the other nucleon. How does the clustering of the six quarks in the two three-quark nucleons appear at large distance scales? How do we treat confining forces in the presence of so many quarks? The approach to these issues on whether or not Q^2, the momentum transferred by the gluons, is large enough to justify the use of perturbative QCD (pQCD).

At small Q^2 the momentum transferred by the gluons is small and the QCD coupling is too large to apply perturbative methods. In the non perturbative regime, calculation are based on models. Many papers have been written on the subject and a complete review is beyond the scope of this work. In order to give the taste of the discussion we mention the Maltaman and Isgur work [15] [16]. They studied the ground state of six quarks interacting through a qq potential previously used to explain the spectrum of excited nucleons, and they found that there is a natural tendency for the quarks to cluster into groups of three (i.e. nucleons). They obtained a reasonable description of the deuteron, and confirmed that the short range $N-N$ repulsion could be largely understood in terms of quark exchange.

If the momentum transfer is high enough, perturbative QCD may be used to study the deuteron reactions. It is assumed that the problem naturally factors into hard scattering process in which the momentum transfer is distributed more or less equally to all the six quarks, preceded and followed by soft, nonperturbative scattering that set the scale of the interaction but does strongly influence Q^2 behaviour.

The Q^2 behaviour is determined by the hard scattering, which can be calculated perturbatively. The calculation is extremely complicate and the formalism and method are reviewed in the several papers by Brodsky and Farrar [17] and Lepage and Brodsky [18]. The pQCD provides explicit testable predictions for the cross section and polarisation observable. For example the Brodsky calculation leads to the constituent counting rules (CCR) [19] that predict the energy dependence of scattering cross sections at fixed value of centre of the mass angle ϑ_{cm}:

$$\frac{d\sigma}{dt} = \frac{1}{s^{n-2}} f(\vartheta_{cm}) \tag{1.2}$$

where s is the square of the total energy in the centre of mass and n is the total number of point-like particles in the initial and final state of the reaction. In deuteron disintegration we have 1 photon and 6 quarks in the initial state and only the 6 quarks in the final state, then $n = 13$ and $d\sigma/dt \sim s^{-11}$: this behaviour is called "scaling".

In an attempt to include some of the soft physics omitted from the pQCD, and to extend the region of applicability of pQCD down to lower momentum transfers, Brodsky and Hiller introduced the idea of reduced nuclear amplitude (RNA) [20]. In this model the gluon exchanges that contribute to identifiable subprocesses (such as nucleon form factors) are collected together and their contributions replaced by experimentally determined nucleon form factors (fig: 1.4). The hope is that the resulting expressions will correctly include much of the missing soft physics, and will therefore be valid to momentum transfers lower than the original pQCD expression from which they were obtained. When applied to deuteron photodisintegration, the cross section is written:

$$\frac{d\sigma}{dt} = \frac{m^2}{24\pi^2(s - m_d^2{}^2} \sum |J| \rightarrow \frac{1}{(s - m_d^2)^2} F_p^2(\hat{t}_p) F_n^2(\hat{t}_n) \frac{1}{p_T^2} f^2(\vartheta_{cm}) \tag{1.3}$$

where:
$1/(s - m_d^2)^2$ is the phase space factor;
$f(\vartheta_{cm})$ is the reduced nuclear amplitude;
F_p and F_n are the proton and the neutron form factors where $\hat{t}_p$ and $\hat{t}_n$ are the average momentum transferred to the proton and neutron:

$$\hat{t}_p = (p_p - \frac{1}{2}p_d)^2 \qquad \hat{t}_n = (p_n - \frac{1}{2}p_d)^2 \tag{1.4}$$

where p_p, p_n and p_d are the momenta of the proton, neutron and deuteron respectively;
and the square of the transverse momentum:

$$p_T^2 = \left(\frac{s}{4} - m^2\right) \sin^2 \vartheta_{cm}. \tag{1.5}$$

Alternatively, if the quark mechanism shown in fig: 1.4 is to be taken seriously, a more detailed calculation is possible. In the work of Sargsian, Miller, Frankfurt and Strikman [21] deuteron photodisintegration was studied in the framework of the Hard Rescattering Mechanism (HRM) where the quark exchange diagram is calculated using model wave function for nucleon and deuteron. The matrix element is written as aa convolution of an elementary quark exchange interaction with the initial and the final nucleon wave functions. The final nucleons are free and the distribution of the initial nucleons is given by the deuteron wave function. The elementary interaction in the HRM is a quark exchange between two the nucleons. A quark of one nucleon knocked-out by the incoming photon rescatters with a quark of the other nucleon leading to the production of two nucleons with high relative momentum. Summation of all relevant quark rescattering amplitudes (similar to the one shown in figure 1.5) allows to express the scattering amplitude of the reaction through the convolution of a hard photon-quark interaction vertex, the large angle p-n scattering amplitude and the low momentum deuteron wave function.

The high energy approaches described above all focus on the region where both $\hat{t}_p$ and $\hat{t}_n$ are large (and perturbative arguments can serve as the foundation for the

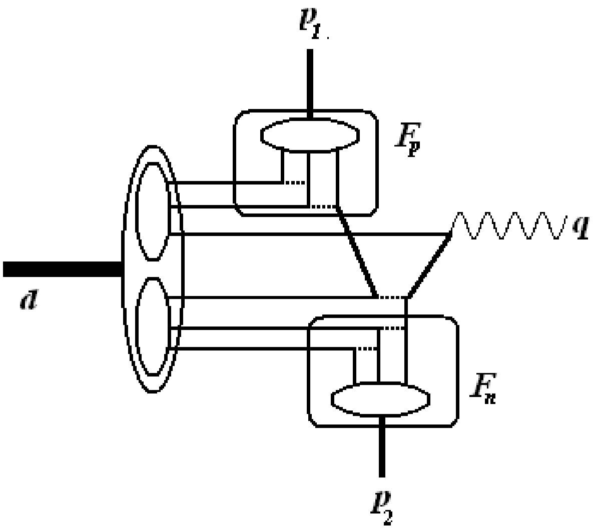

Figure 1.4: A ”typical” pQCD diagram describing photodisintegration. There are 5 hard gluons. The RNA model places the hard gluons in the rectangular boxes within nucleon form factor.

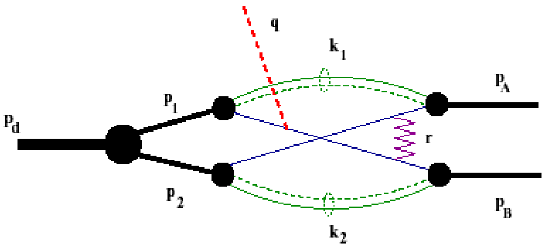

Figure 1.5: Typical quark-rescattering diagram. k_1 and k_2 define the four-momenta of residual quark-gluon system of the nucleons

treatment). Alternatively, we may ask what to expect when one of the momentum transfer is small (but s is large).

We want to recall the Kondratyuk and collaborators work. They developed a model [22] (which they refer to as the ”quark-gluon string model” QGSM) based on the Regge generalisation of the nucleon Born term. The QGSM is a non perturbative approach, which has been extensively used for the description of hadronic reaction at high energies. It is based on a topological expansion in QCD of the scattering amplitudes in power of $1/N$ where N is the number of colors or flavours and it assumes that the scattering amplitudes at high energy is dominant by the exchange of the three valence quarks in the t-channel or u-channel (fig: 1.6(a), 1.6(b)) dressed by an arbitrary numbers of gluons. This picture corresponds to the formation and break up of a quark-gluon string in the intermediate state, leading to the factorization of the amplitudes: the probability for the string to produce different hadrons in the final state, does not depend on the type of the annihilated quarks, but is only determined by the flavour of the produced quarks. The intermediate quark-gluon string can be easily identified with the nucleon Regge trajectory. In this sense, the QGSM can be considered as a microscopic model for the Regge phenomenology. QGSM has been applied for the description of the deuteron photodisintegration reaction [23] using QCD motivated nonlinear barion Regge trajectories [24] with full inclusion of spin variables. The energy dependence of the predicted cross section is:

$$\frac{d\sigma}{dt} \propto \left(\frac{s}{s_0}\right)^{2\alpha_N(t)-2} \tag{1.6}$$

where $\alpha_N(t) = -0.5 + 0.9t + 0.25t^2/2$ is the nucleon Regge trajectory. The model is intended to work for $E_\gamma > 1\ GeV$.

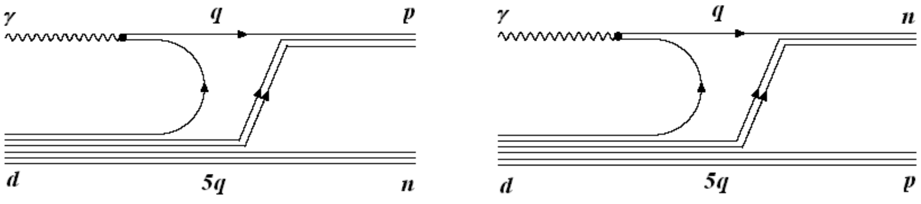

(a) t−channel (b) u−channel

Figure 1.6: QGSM Diagrams describing three valence quark exchanges in t and u channels

Experimental results for the differential cross sections from Stanford laboratories (SLAC), from Jlab and from MAINZ are shown in figure 1.7. The data are in agreement with CCR (scaling appears around 1.5 GeV where the blue arrow is located) and thus with perturbative QCD expectations.

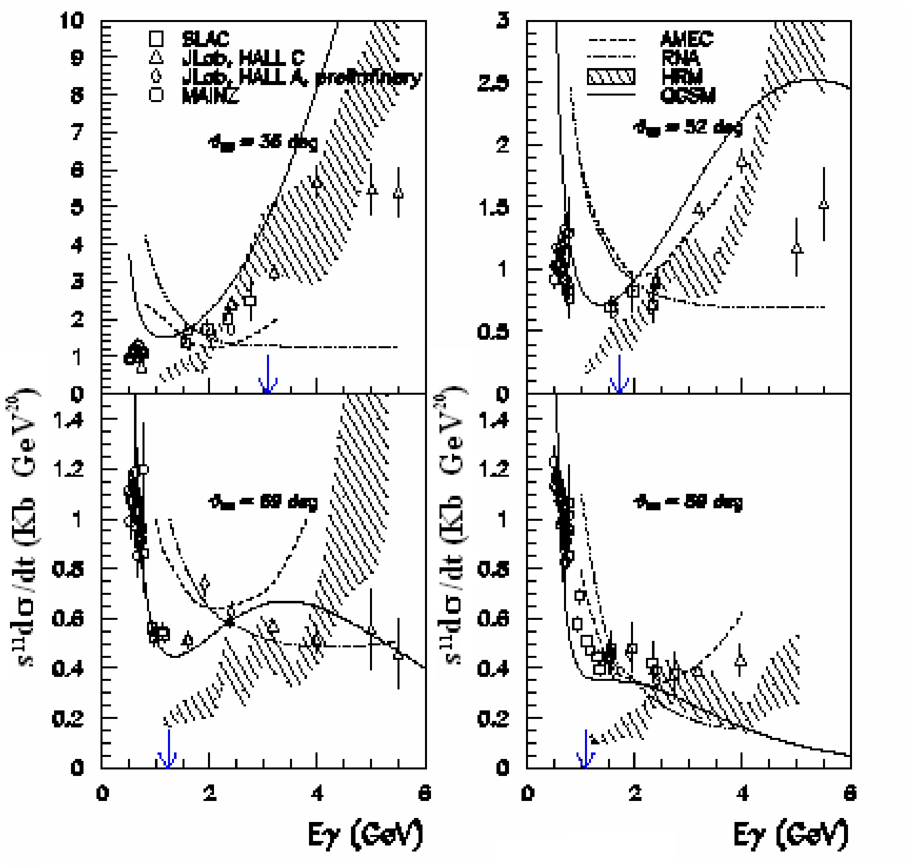

Figure 1.7: Deuteron photodisintegration cross section multiplied by s^{11}. Experimental data are from MAINZ [25], SLAC [26] [27] [28], Hall C of TJNAF [29] [30], and Hall A of TJNAF [31]. The arrows indicate where the onset of CCR scaling is expected. The theoretical curves are: QGSM calculation (solid); RNA (dotted), AMEC (dashed). The band is the HRM; the authors propose to using experimental data for the *pn* cross section, but since data does not exist for the actual kinematic conditions needed, it must be extrapolated, and prediction are given as a band corresponding to the uncertainties introduced by the extrapolation.

1.4 Polarisation observable: Σ the beam asymmetry

The differential cross section of a reaction using a linearly polarised incoming gamma-ray beam can be written as:

$$\left(\frac{d\sigma}{d\Omega}\right)(E_\gamma, \vartheta^p_{cm}, \varphi) = \left(\frac{d\sigma}{d\Omega}\right)_{unp}(E_\gamma, \vartheta^p_{cm}) \cdot \left(1 - P \cdot \Sigma(E_\gamma, \vartheta^p_{cm}) \cos 2\varphi\right) \tag{1.7}$$

where $\left(\frac{d\sigma}{d\Omega}\right)_{unp}(E_\gamma, \vartheta^p_{cm})$ is the unpolarised cross section;
φ is the angle formed between the reaction plane and the direction of the photon polarisation vector;
P is the polarisation degree and
$\Sigma(\vartheta^p_{cm}, \varphi)$ is the polarisation observable called beam asymmetry. The beam asymmetry can be also defined by the relation:

$$\Sigma = \frac{1}{P}\left(\frac{d\sigma_\perp - d\sigma_\parallel}{d\sigma_\perp + d\sigma_\parallel}\right) \tag{1.8}$$

where $d\sigma_\perp$ and $d\sigma_\parallel$ are the cross sections when the reaction plane is perpendicular and parallel to the direction of the photon polarisation vector, respectively. It is clear from the 1.8 that Σ covers the range between -1 and 1.

The interest in measuring the polarisation observables, such as the beam asymmetry, is in the fact that they depend to the interference on among the reaction transition amplitudes, and they are sensitive to all contributions. On the contrary the cross section, being a sum of the square of the transition amplitudes, may be dominated by only some of them.

Several data exist for the beam asymmetry at incoming photon energies below 700 MeV for different proton polar angle in the centre of mass (fig: 1.8(a)). On the contrary only in two experiment at Yerevan in the years 1982 [33] and 1987 [34] measured the beam asymmetry for $E_\gamma > 700\ MeV$ (in the our energy range) at $\vartheta^p_{cm} = 90°$ 1.8(b).

This work provides experimental results of the beam asymmetry in the photon energy range $680\, MeV \leq E_\gamma \leq 1480\, MeV$ at proton polar angles in the centre of mass $\vartheta^p_{cm} = 24°, 55°, 90°, 125°$.

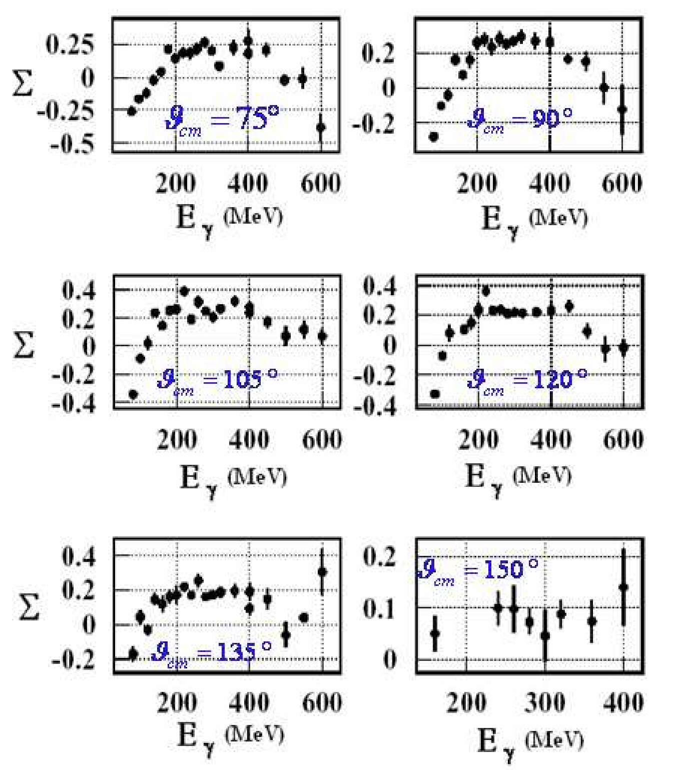

(a) Σ beam asymmetry for several ϑ^{p}_{cm} at photon energies below 700 *MeV* [32]

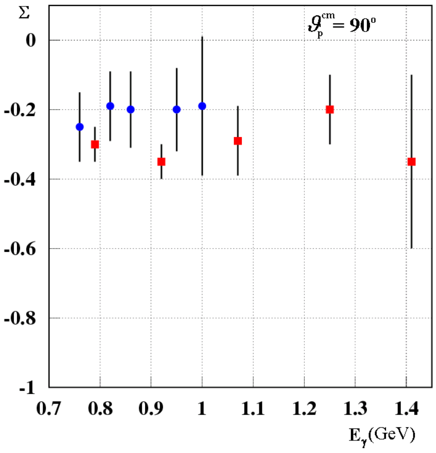

(b) Σ beam asymmetry at $\vartheta^{p}_{cm} = 90°$ in the *GeV* region from the Yaravan experiment.

Figure 1.8: Σ beam asymmetry data existing presents in literature.

Chapter 2

GRAAL: The experimental apparatus

2.1 Introduction

The GRAAL facility is located at the European Synchrotron Radiation Facility (ESRF). It consists of: a fully polarised high-energy gamma-ray beam obtained by backward Compton scattering of laser light against the high-energy electrons circulating in the ESRF storage ring; a liquid Deuteron or Hydrogen target; the LAGrANγE apparatus [1].

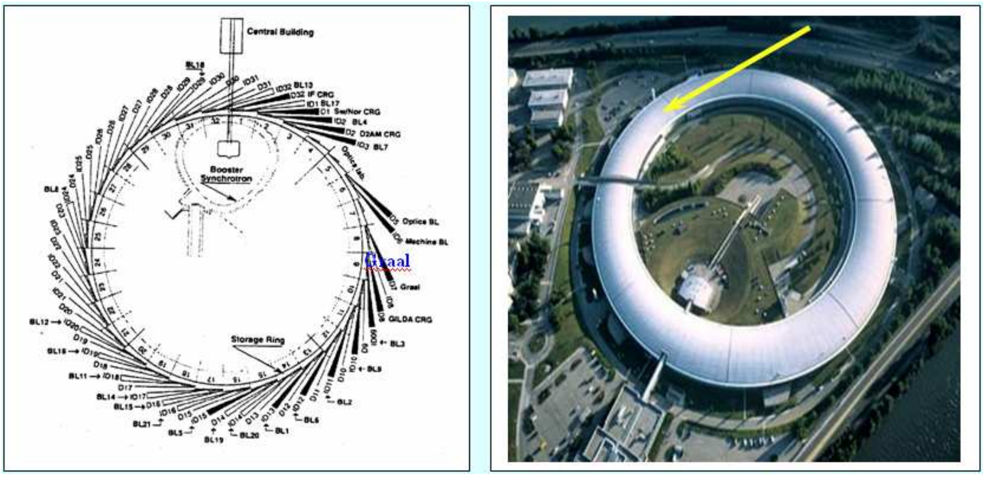

Figure 2.1: On the left, the ESRF storage ring scheme. We can distinguish the LINAC, the synchrotron and the beam lines. On the right a suggestive ESRF photo. The yellow arrow shows the GRAAL location.

---

[1] Large Acceptance GRaal Apparatus for Nuclear γ Experiment

2.2 The storage ring and the electrons beam

The ESRF a European research centres and for the production of X-rays having $\lambda \simeq 10^{-9} - 10^{-11} m$ wave length. X-rays, produced by the deflection of the electrons circulating in the storage ring, are used in many fields of science as physics of matter or biology and medicine.

The electrons are initially accelerated by a LINAC (fig:2.1) up to 200 MeV energy, they are then injected in a synchrotron that has a 300 m of circumference, in which their energy is increased to a final value of 6.06 GeV; finally they are injected in a 844 m circumference storage ring. The goal is to produce a high brillance and low dispersion beam by optimizing the electron intensity and emittancce. The result is an electron current of 150 and 200 mA, circulating in ultra-high-vacuum ($10^{-10} Torr$), and having very small dimensions of the order of some μm.

64 magnetic dipoles along the ring in order to keep the electrons with the right energy in a closed orbit. Between two consecutive dipoles there are four quadupoles and sextuple and a machine elements for the X-rays transport in the experimental hutches. In the straight section, between one dipole and the next one there are some insertion devices, like undulators and wigglers, that stimulate electrons to emit X-rays. A resonant cavity, that works with a frequency of 352 MHz, compensates the electrons energy lost by radiation.

The storage ring has different operation modes for the electron current, at maximum filling contains 900 bunches of electrons, each bunch with a duration of approximately 140 ps and with a separation of 2.8 ns from the previous one. The life time of the electron beam depends on the way of functioning of the ring, on the quality of the vacuum and on the intensity of current. The electrons interaction with the remaining gas in the vacuum line (which is about 10^{-9} $Torr$) and the interaction between the electrons, are the life time main limitation.

2.3 Project GRAAL

The GRAAL[2] project [35] differs from the other experiments present at the ESRF as it does not use X-rays, but uses the electrons of the storage ring to produce a fully polarised high-energy gamma-ray beam ($400 MeV < E < 1500 MeV$).

The experiment is installed next to one of the short straight sections of the ring, called **D7**, which has the advantage to have more space for the location of the experimental hutch since the previous section is free and not available for experiment.

The apparatus is divided in to three experimental hutches (see fig. 2.2): one with the laser, another one with target and detectors and a room for the electronics and the acquisition system. There is also a detector for gamma tagging place in the internal side of storage ring.

---

[2] GRenoble Anneau Accelerateur Laser

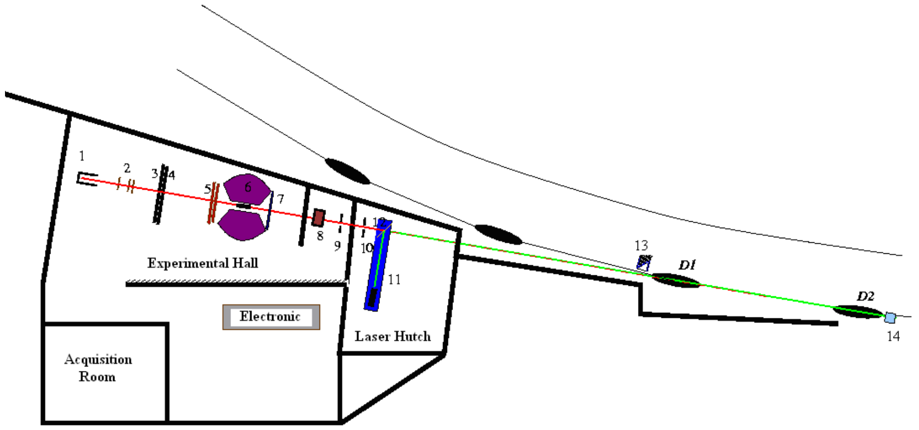

Figure 2.2: It is the GRAAL experimental area. We can distinguish: 1)The Spaghetti monitor; 2)The Thin monitor; 3)The shower wall; 4)The hodoscope wall; 5)The Plane wires chambers; 6)The BGO calorimeter with the barrel (in black), 7)The Catania disk (presently removed); 8)The clean magnet; 9)The Collimator; 10)The Copper filter; 11)The Laser, 12)The Beryllium mirror; 13)The tagger 14)The Bolometer and the interaction zone between dipoles D1 e D2.

2.4 The polarized photon beam at GRAAL

2.4.1 History

In 1963 Arutyunyan, Tumanian [36] and, independently, Milburn [37] have shown that backward scattering of light against high-energy electrons could produce high-energy gamma-rays. This has been later demonstrated by various authors [38] [39] [40] [41].

In 1967 Malvano, Mancini and Schaerf [42] pointed out that a polarised beam of gamma-rays with an energy and intensity useful for photonuclear research could be produced by the interaction, in the straight section of a storage ring, of the high electron current ciculating in it with the high photon intensity available inside a laser optical cavity. Theory became reality at National Laboratories of Frascati on the storage ring **ADONE** where a fully polarised beam of 80 MeV gamma-rays was produced and used for several years for the study of photonuclear-reactions. This early success stimulated similar activities in other laboratories. Today the technique for the production of Landon beam (that is the name of this kind of gamma-rays beams!) is well established and several working facilities exist all around the world.

2.4.2 Compton scattering kinematics

The reaction used in order to produce high-energy gamma-rays beam is the elastic scattering of photons on high-energy electron in flight [43]. In this reaction, known as Compton effect, an ultra-relativistic electron strikes against a photon as shown in pictures 2.3:

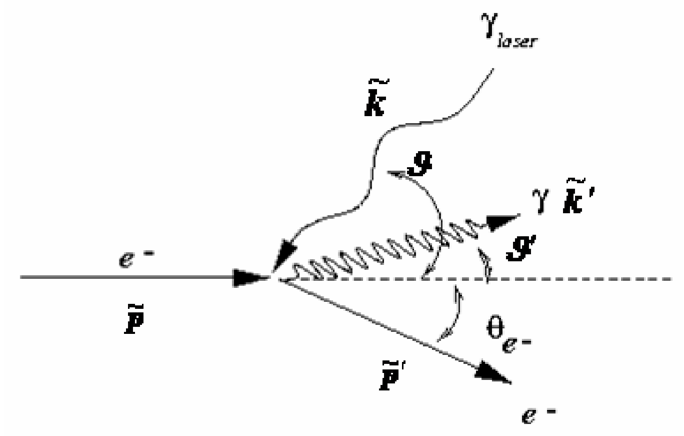

Figure 2.3: Compton scattering

From quadri-momentum conservation we have:

$$\tilde{p} + \tilde{k} = \tilde{p}' + \tilde{k}' \tag{2.1}$$

Where $\tilde{p}$ and $\tilde{k}$ are respectively the 4-momenta of the incoming electron and incoming photon, while $\tilde{p}', \tilde{k}'$ are the 4-momenta of the respective outgoing particles.

If the z axis is coincident with the direction of the incoming electron, it is possible to solve the equation 2.1 for k' in terms of:

- polar and azimuthal angles ϑ and φ of the incoming laser photon;
- polar and azimuthal ϑ' and φ' of the scattered photon;
- energies k and k' of the incident photons and of the scattered $\overrightarrow{\gamma}$;
- relativistic γ factor of the electron (with $|\vec{p}| = m\beta\gamma$ e $E = m\gamma$).

$$k' = k\frac{1 + \beta cos\vartheta}{(1 - \beta cos\vartheta') + \frac{k}{m_e\gamma}(1 + cos\vartheta cos\vartheta' + sin\vartheta sin\vartheta' cos(\varphi - \varphi'))} \tag{2.2}$$

In order to simplify the previous equation, for the GRAAL beam we can make the following assumptions:

I. The electrons are ultra-relativistic so that $\gamma = E/m_e \simeq 12000$;

II. The ultra-relativistic nature of the electrons lead to a strong Lorentz boost, this implies the in the laboratory frame the backscattered $\overrightarrow{\gamma}$ is emitted in a narrow cone with angular aperture $\Delta\vartheta \sim 1/\gamma$ around the direction ϑ' = 0.

III. The good alignment of the laser with the z axis allows to assume $\vartheta = 0$

Since $\vartheta \approx= 0$ and ϑ' we can replace in eq 2.2, $\sin\vartheta, \sin\vartheta', \cos\vartheta, \cos\vartheta$' with their Taylor series. If we take into account just to second order of the series, we obtain:

$$k'(\vartheta') \simeq k\frac{4\gamma^2}{1+\frac{4k\gamma}{m_e}+(\vartheta'\gamma)^2} = E\frac{z}{1+z+(\vartheta'\gamma)^2} \tag{2.3}$$

with: E = incoming electron energy, and

$$z = \frac{4k\gamma}{m_e} \qquad x = (\vartheta'\gamma)^2 \tag{2.4}$$

The maximum energy of the scattered photon is given by:

$$k_{max} = E\frac{z}{1+z} = E \cdot a \tag{2.5}$$

which is obtained in head-on collision where $\vartheta' = 0$. The energy of the emitted photon decreases rapidly (figure 2.4) when ϑ' increases $\gamma \gg 1$.

2.4.3 Energy resolution

We must find a way to determine the energy of backscattered photons without introducing perturbations on the beam. With the approximation $z \gg 1$ and $x \gg 1$ we have:

$$\frac{\Delta k}{k_{max}} = \frac{x}{1+z+x} \approx x \tag{2.6}$$

where $\Delta k = k_{max} - k'$
If the emitted photons cross through a collimator with half-aperture $\Delta\vartheta$,then:

$$x = (\gamma\Delta\vartheta')^2 \tag{2.7}$$

gives an estimate of the best energy resolution (FWHM) which can be obtained after the collimator. It is clear from equation 2.6 that defining the energy of the outgoing gamma-ray by its angle requires:

$$x \ll 1 \tag{2.8}$$

or an angular resolution:

$$\Delta\vartheta \ll \frac{1}{\gamma} \tag{2.9}$$

For the electrons circulating in the ESRF $\gamma \approx 12000$, and it is practically impossible to use a collimator, in facts, tha value of γ would implies a half-aperture $\Delta\vartheta \approx 10^{-4}$ Moreover, the angle between the electron on the outgoing photon cannot be defined better than the angular divergence of the incoming electrons beam. In a storage ring (with small coupling) this is dominated by angular divergence in the horizontal plane which is indicated by σ'_x. Therefore:

$$\Delta\vartheta \geq \sigma'_x \tag{2.10}$$

and we must have:

$$\sigma'_x \ll \frac{1}{\gamma} \tag{2.11}$$

At an electron energy above 2 GeV it is difficult to achieve condition 2.11. For this reason, to define the gamma-ray energy we need a different technique. The energy of the scattered gamma-ray is also given by conservation law:

$$k' = E - E' + k \cong E - E' \tag{2.12}$$

Therefore, if we know the energy of the initial electron and we measure the energy of the final one, we can determine the photon energy with an error (r.m.s.) given by:

$$\sigma^2_{k'} = \sigma^2_E + \sigma^2_{E'} \tag{2.13}$$

The magnetic elements in the ring are optimized for electrons of 6 GeV, consequently they remove from the machine lattice the electron which has produced a gamma-ray and then lost energy. The electron displacement **x** with respect to the orbit is proportional to energy lost in the Compton scattering. Therefore a measure of this displacement gives information about the gamma-ray energy. The equation:

$$k = E - E'(x) = E\frac{x}{x + a_0} \tag{2.14}$$

connects the energy of the produced photon with the displacement **x** of the electron.

A Montecarlo simulation of the photon-electron interaction in a ring straight section and of the deflected electron transport by magnetic lattice from the interaction point to a fixed point where the displacement **x** is measured by a tagger detector (see par:2.5.2), allows to determinate this equation. Simulations and measurements give for the 2.14 the value a_0 = *159.00 mm*.

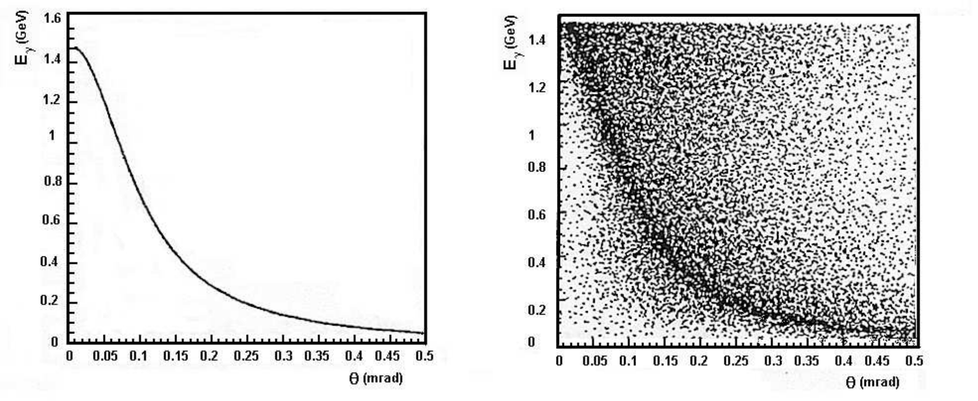

Figure 2.4: A simulation of the relation between the photon emission angle and the photon energy at GRAAL in the case: a)electron beam angular divergence is neglected; b)electron beam angular divergence is taken into account.

2.4.4 Yield

The total gamma-ray-beam intensity is given by the Compton cross-section convoluted with the laser and the electron bunch spatial density u_γ, u_e. If *dn/dk* is the total number of gamma-rays per second and per MeV, we can write [44]:

$$\frac{dn}{dk} = (1+\beta)c\frac{d\sigma}{dk}\int u_\gamma u_e dV \tag{2.15}$$

The integration in *dk* provides the rate *n* of backscattered gamma:

$$n = (1+\beta)c\sigma\int u_\gamma u_e dV = PIL \tag{2.16}$$

where

$$\sigma = \frac{8}{3}\pi r_0^2 = 6.6\cdot 10^{-25} cm^2 \tag{2.17}$$

is the classical Thompson cross-section, and:
P = the laser power in Watt;
I = the electron current in Ampere;
L = the luminosity in $s^{-1}W^{-1}A^{-1}$.

The luminosity *L* is obtained by the spatial integration of the photon and electron density distributions. We assume that the laser and the electron beams are perfectly aligned on the *z*-axis, that they overlap in the straight section and that their distributions are Gaussian in the x and y coordinates (perpendicular to the direction of the beam):

$$
\begin{aligned}
u_e &= \frac{u_{0e}}{2\pi\sigma_x\sigma_y} exp\left[-\frac{x^2}{2\sigma_x} - \frac{y^2}{2\sigma_y}\right] && (2.18) \\
u_\gamma &= \frac{u_{0\gamma}}{\pi\omega^2} exp\left[-2\frac{x^2+y^2}{\omega^2}\right] && (2.19)
\end{aligned}
$$

where:
$u_{0e} = I/ce$ is the electron density on the central trajectory;
$u_{0\gamma} = P/ck$ is the photon density on the laser axis (k in eV);
$\sigma_x = \sigma_x(z)$ and $\sigma_y = \sigma_y(z)$ is the horizontal and vertical dispersion of the electron beam which depend by the electron longitudinal position;
ω is the radial dispersion of the laser beam.

Integrating over x and y, we have for L:

$$L = \int \frac{dz}{\sqrt{\omega^2(z) + 4s_x^2(z)}\sqrt{\omega^2(z) + 4s_y^2(z)}} \tag{2.20}$$

the integral extended over length of interaction region. For the Graal project:

$$L = 2.6 \cdot 10^7 s^{-1} A^{-1} W^{-1}$$

Using the UV lines of a commercially available Argon Ion laser with:

$$P_{max} = 7W$$

and with a circulating electron current

$$I = 0.2A$$

we have a total gamma-ray flux of:

$$n = 1.15 \cdot 10^7 s^{-1} \tag{2.21}$$

which corresponds to a tagged intensity of:

$$n_L = 1.04 \cdot 10^7 s^{-1} \tag{2.22}$$

and to a tagged and collimated intensity of:

$$N = 0.9 \cdot 10^7 s^{-1}. \tag{2.23}$$

Since almost all the scattered electrons are removed from the circulating beam, the number of electrons lost per second (dN_e/dt) is equal to the number of the produced gamma-rays:

$$\frac{dN_e}{dt} = n = PLI = PL\frac{N_e e}{T} = N_e\frac{LPe}{T} = \frac{N_e}{\tau_L} \tag{2.24}$$

where

$$\tau = \frac{T}{LPe} \tag{2.25}$$

is the *beam mean life* produced by the operation of the laser and $T = 2.8\mu s$ is the revolution period in the ESRF storage ring The value for τ_L is:

$$\tau_L = \frac{2.8 \cdot 10^{-6}}{2.6 \cdot 10^{7} \cdot 7 \cdot 1.6 \cdot 10^{-19}} = 9.6 \cdot 10^{4} s = 26 hours \tag{2.26}$$

2.4.5 Polarisation of the GRAAL Beam

The helicity of extremely relativistic electrons is conserved in the interactions so that no depolarisation of the photon may occur due to electron spin-flip. For diffusion angle different from 180° a depolarisation may occur due to the transfer of orbital momentum from electron to the photon. Therefore gamma-rays moving in the direction of the electron and having maximum energy available retain the polarisation of the laser light. The polarisation of the scattered gamma can easy be changed. It is enough to change the polarisation of the laser light and this is true both for linear and circular polarisation.

For gamma-ray of lower energy scattered at small angle the polarisation is less the unit but remains large over a broad energy range (fig:2.5). The linear polarisation is larger than 0.9 down to an energy larger than $0.8k_{max}$.

Both polarisation (linear and circular) of the scattered photon are proportional to the polarisation of the laser light as follows [45]:

$$P_{\gamma}^{L} = P_{laser}^{L} \frac{(1 - \cos\alpha)^2}{2\,(\chi + 1 + cos\alpha^2)} \tag{2.27}$$

$$P_{\gamma}^{C} = P_{laser}^{C} \left| \frac{(2 + \chi)\, cos\alpha}{(\chi + 1 + cos\alpha^2)} \right| \tag{2.28}$$

with:

$$\chi = \frac{\rho^2 (1 - a)^2}{1 - \rho(1 - a)} \tag{2.29}$$

$$cos\alpha = \frac{1 - \rho(1 + a)}{1 - \rho(1 - a)} \tag{2.30}$$

where

$$\rho = \frac{k'}{k_{max}}$$

and a defined by eq:2.5.

The polarisation of Graal beam is changed by a polarisation rotator that can either change the orientation of the vertical linear polarisation ($\lambda/2$) or transform it in circular polarisation ($\lambda/4$).

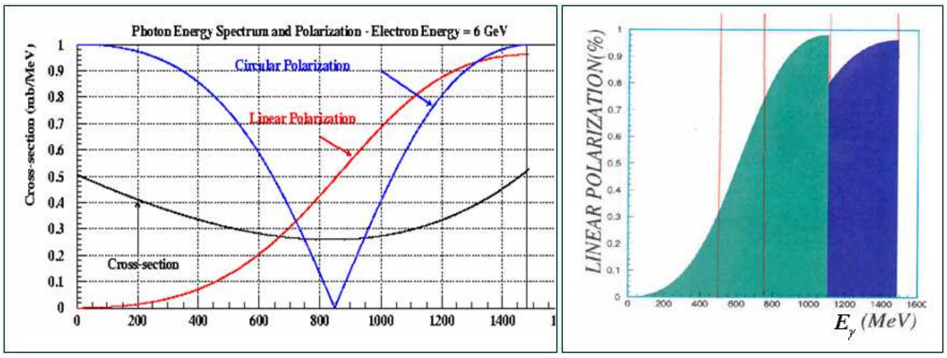

Figure 2.5: **Polarisation**: on the left side is shown the relationship between the photon energy and its circular and linear polarisation degree for back-scattered photons on 6 GeV electrons. The picture on the right is the comparison between the polarisation degree for two different kinds of laser line: visible (green) ed ultraviolet (blue).

2.4.6 The laser hutch

Outside the ESRF ring is located the GRAAL experimental hutch with the laser and the Optical System for the transport of the laser light.

The optical bench is about 30 *m* far from the area of Compoton interaction. The small size of the electron beam in the interaction zone requires that the stability in the transport of the laser beam is of the order of tens μm. This condition requires the use of mechanically very stable optical components with absolutely precise movements. The mechanical stability is ensured by a granite monolith long 6 *m* long positioned perpendicularly to the direction of the gamma-rays beam.

The laser in use is an Laser Argon Ion (SABRE-R DBW 25/7 of Coherent) which has the advantage to allow the choice of more laser wave lengths (tab:2.1) which can be selected through optical components and a prism inside the resonant cavity. In front of the laser there is a safety valve that can be operated from outside to interdict the laser light.

Two mirrors (MP1, MP2) form the periscope carrying the laser beam to the same height as that of the electrons in the ring. The position of the mirrors can be governed by a remote control system that allows to centre the laser beam on electrons with minimum movements of 0.02 μm.

In order to focus the laser beam in the electron-laser interaction region, situated at about 30 *m* from the laser, we utilise a zoom system (see picture 2.6) consisting of three lenses. Two of these lenses, L_1 and L_3, are plano-convex, and L_2, positioned between the other two, is plano-concave. The lenses can be adjusted with extreme precision in order to ensure the laser beam a minimum diameter ($\approx 300-600\,\mu m$) immediately after the last quadrupole (that serves as magnetic lens for focusing of the electrons) of straight section and before the **D1** dipole. This is to maximise the probability of interaction between the two beams which largely depends on the space density.

After entering the vacuum line of the hall, the laser is reflected by 90° by a mirror of beryllium place at 45° with respect the laser beam axis. The vacuum line has a pressure compatible with that of the storage ring ($P \approx 10^{-10} Torr$). The laser photons which did not suffer an interaction with electrons, cross the second dipole and go out from the vacuum line of the ring. Observing the counting rate of the tagging system, we can optimise the alignment between the laser and the electron beam moving the mirrors of the periscope.

The $\overrightarrow{\gamma}$ photon produced in the Compton interaction, go back in the same vacuum line and, crossed the Beryllium mirror, continue towards the experimental hall where are located the target and the LAGrANGE apparatus. Before entering the laser hall, the beam crosses a 20 *cm* long lead collimator: the aim of this device is to absorbing the X-rays produced in the synchrotron light emission by the electrons of the beam. A magnet cleans the beam from the electrons and positrons created by the collimator and finally the photons reach the target through a vacuum pipe ($10^{-5} Torr$).

The mirror at 45° is composed of Beryllium on which is deposited a thin layer of aluminium that makes it reflective. The choice of beryllium is due to its low atomic number (Z=4) that minimises the probability of absorption of photons. It is calculated that the losses of gamma-photons crossing the mirror do not exceed 5%.

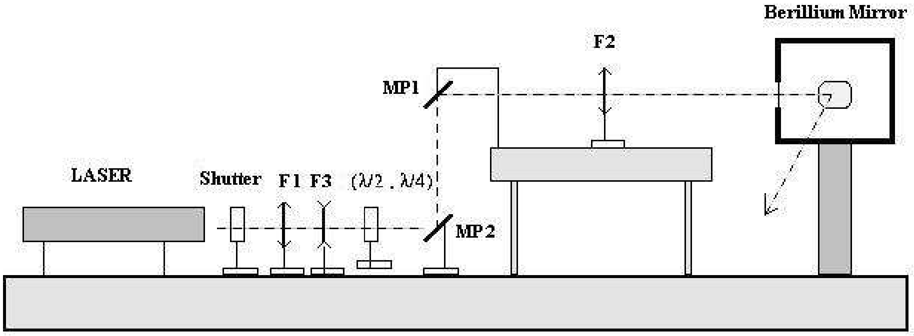

Figure 2.6: The optical bench. We can see: the laser, the shutter, the zoom system (L1, L2 and L3 lenses), the periscope (MP1 and MP2 mirrors), $\lambda/2$ or $\lambda/4$ plate, the Beryllium mirror in the vacuum line.

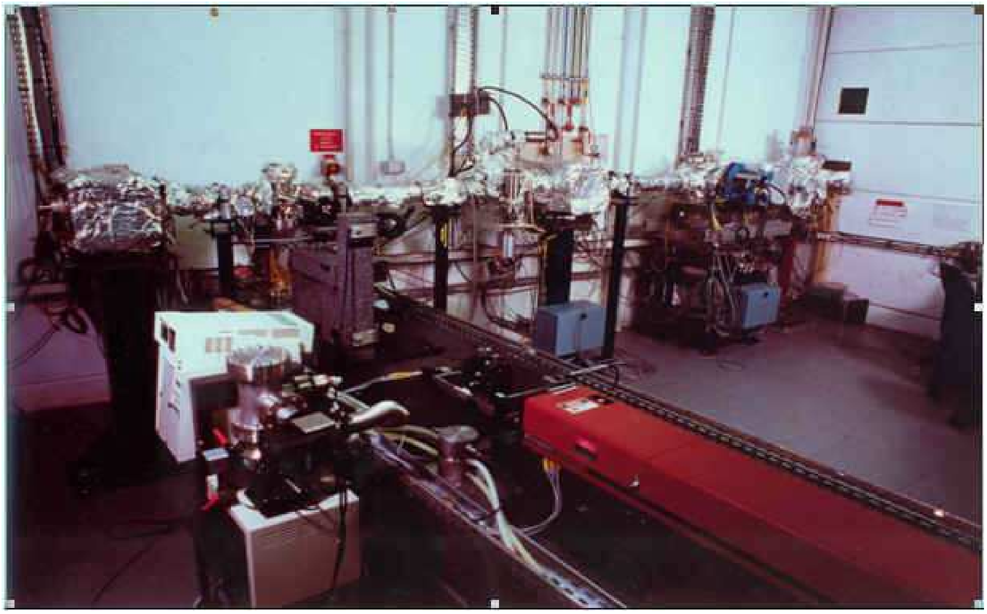

Figure 2.7: In the picture is shown the laser hutch, we can distinguish the laser the long red thing!), the periscope (in the center) and the vacuum line (the silvery pipe near the wall).

range	λ(nm)	E_γ(eV)	Maximum power(W)	E_γ^{max}(GeV)
green	514.5	2.41	13	1.1
ultra-violet	351.3	3.53	2	1.5
visible multi-line	454.5-528.7	2.34-2.73	30	1.25
UV multi-line	333.3-363.8	3.41-3.72	7	1.6

Table 2.1: Data relating to the different laser lines used. There are listed the wavelength, the energies of photon laser line, the maximum power of the line and the maximum energy of the GRAAL beam for that line.

2.5 The GRAAL beam detectors

Are an integral part of the experiment four detectors used for monitoring of the gamma-rays beam, they are:

1. Two detectors that allow to determine the flux of photons experimental hall;
2. The two tagging detectors that allow to assign an energy to each photon produced allow to give the start time to every photo-nuclear event.

2.5.1 Flux detectors

The average photon rate at GRAAL is about $10^6\gamma/s$ integrated all over the energy spectrum, so an high efficiency detectors would be affected by the pile-up. To solve this problem two detectors are located at the end of the experimental hutch, the first is called **thin monitor** and the second **”spaghetti”**.

In the figure 2.8(a) we can see the first detector made of three scintillator counters and a Al foil (2 mm thick), working as a γ converter, which is located between the first and the second scintillator. The coincidence between the last two counters in anti-coincidence with the first one is the signature for photons that have converted in aluminium. This allows to reject single electrons or e^+e^- pairs. The counters are thin in order to have a low efficiency and avoid the pile-up; this allows the monitor to work at very high photon rate.

The ”spaghetti” detector [46], shown in figure 2.8(b), is a total absorption counter with a 100% efficiency, which is affected by pile-up at usual beam intensities, but can be used to evaluate the monitor efficiency $\epsilon_{mon}(E_\gamma)$ at low rate as a function of the energy of the incident photon. Scintillanting fibres with 1mm of diameter forms the detector. These fibres are placed in a block of lead with 80 cm in depth and oriented parallel to the direction of the beam. Fibres are divided in four regions each of them coupled with a photomultiplier, and in this way, studying the energy distribution in the region is possible to check the average position of the beam.

When the laser is off, only bremsstrahlung photons are produced by the electrons on the residual gas in the ring. In this case it is possible to determine the efficiency of the thin monitor comparing the number of events detected by the two detectors. This efficiency slightly depends on the photons energy which is provided by the tagging detector and is given by:

$$\epsilon_{mon} = \lim_{N_\gamma \to 0} \frac{N_{mon}}{N_{spag}} \tag{2.31}$$

where:
N_{mon} is the number of photon detected by thin monitor;
N_{spag} is the number of photon detected by the ”spaghetti” detector.

Photon flux as a function of the energy is:

$$N_\gamma(E_\gamma) = \frac{N_{mon}(E_\gamma)}{\epsilon_{mon}(E_\gamma)} \qquad (2.32)$$

(a) Thin monitor (b) Spaghetti monitor

Figure 2.8: The flux monitor

2.5.2 The tagger

The tagging system consists of a position sensitive detector located inside a movable box, close to the stored electron beam. In order to determine accurately the energy of the photons produced in the Compton interaction, we need to measure with the greater possible precision the displacement of the electron by the central orbit. In addition we must associate to the electron a measure of time of flight to determine from which bunch it derive.

Montecarlo simulations show that the electron displacement x associated with high energy gamma-rays production, may not be known with a resolution better than $300\mu m$. This is mainly due the to angular divergence of the electron beam in the interaction point. This uncertainty in the position limits the resolution of the tagging detector.

So the general requirements for the tagging detector are:

- 300 μm position resolution;
- fast timing response, in order to discriminate in time among the electrons produced in different bunches ($\Delta t = 2.8\ ns$);
- small overall dimension in order to fit inside the detector container.

A solution to these severe constraints is provided by a μ-strip solid state detector of 128 channels of 300 μm pitch, which guarantees the required position resolution, in coincidence with a set of fast scintillating detectors, for good time resolution. The set of scintillating plastic detectors consists of two long scintillators, covering all the μ-strip detector length, and eight small scintillators, each covering 16 strips (2.9(a)). Triple coincidences from one of the short scintillators with the two long ones, synchronised with the ring RF signal,are used both as strobes for μ-strip detector signal and for timing information. In particular they provide a precise start for the time of flight of the particles impinging on the forward detectors and on the barrel. From the first plastic (called 0) we obtain, by a discriminator, a logic signal which is sent to a shift-register with the RF signal used as a clock.

The measurement of the Compton edge provides the energy resolution of the tagger detectors. In fact the position of the edge for a fixed laser line is well known from the theory, then a fit of the tagger μ-strip spectrum allows to obtain the energy calibration and an estimation of the resolution. For the GRAAL tagger we have $\sigma_{E_\gamma} = 6.8\ MeV$ corresponding to a FWHM of 16 MeV.

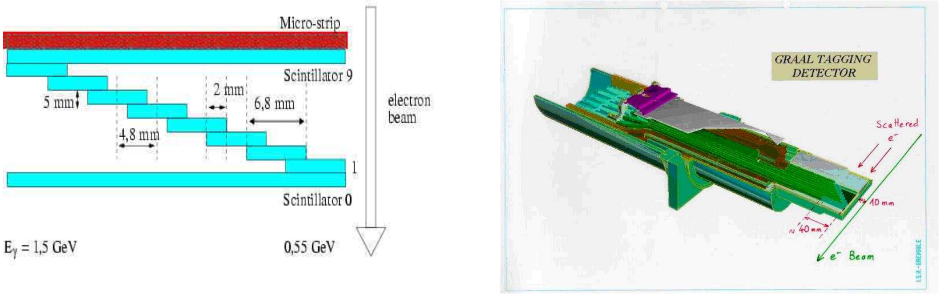

(a) Tagger scheme

(b) Tagger

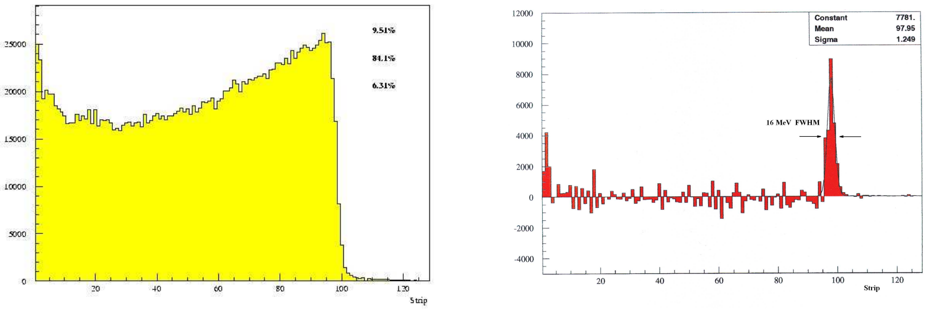

(c) Energy spectra of Compton photon

(d) Energy resolution

Figure 2.9: Figure (a) and (b) show tagger scheme, we can see the microstrips for the position measurements and the 10 scintillator for the time of flight measures. In figure is shown (c) typical energy spectrum of Compton photon.

2.6 The cryogenic target

When the gamma-ray beam arrives in the experimental hutch, just after the collimator, it passes through the cleaning magnet which deflects the charged particles produced by the photons on the collimator. A concrete wall stops these particles immediately after.

Just after the magnet, the vacuum line stars at the end of which is placed the cell containing the target of liquid deuterium. The target is fixed on the beam axis, 25 m far from the interaction region. It is composed of a liquid Hydrogen (H_2) or Deuterium (D_2) contained in a Mylar cell of three possible different lengths (3,6,12 cm) and 4 cm in diameter.

A cryostat, working with Helium cycles, lowers the cell temperature. When the cell is filled up the working temperature of the liquid target is about $17^\circ K$. The total thickness of the Mylar caps is 21 μm ($\rho = 1,39\ g/cm^3$). A photo of the target cell is show in picture2.10(a)

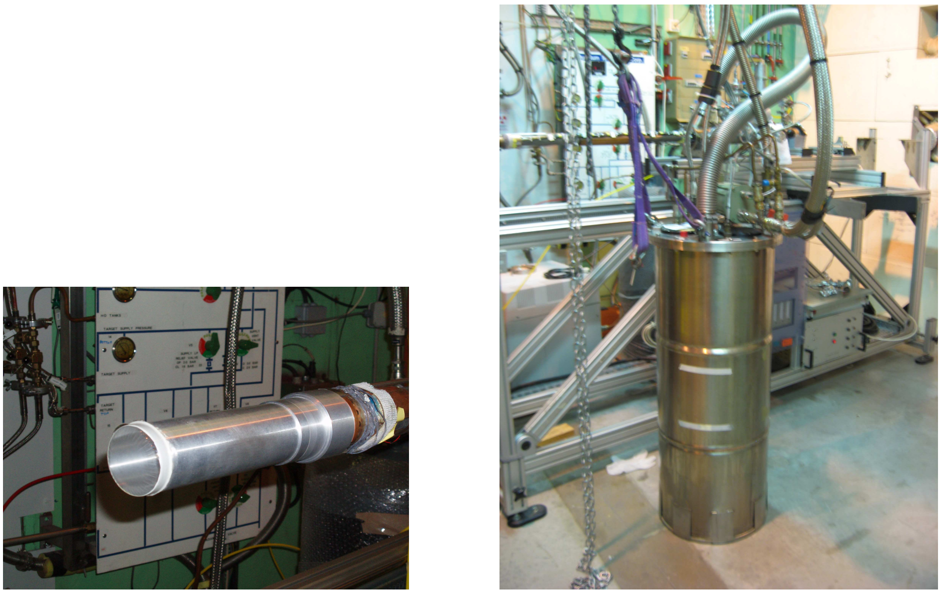

(a) Target

(b) Cryostat

Figure 2.10: Figure (a) shows the external of the target. The cylindrical cell is inside. Figure (a) shows the cryostat used to liquefy the deuterium inside the cell.

2.7 LAGrRANγE apparatus

The LAGRANγE apparatus consists of a set of detectors that surround the target and is divided into three zones (picture 2.11): the central region, where the detectors have a cylindrical symmetry, and cover the angles in ϑ between 25° and 155°, corresponding to a solid angles of $\Delta\Omega \approx 3.5\ \pi$; the forward region for $\vartheta < 25°$ ($\Delta\Omega \approx 0.2\pi$ and the backward region for $\vartheta > 155°$ ($\Delta\Omega \approx 0.2\pi$).

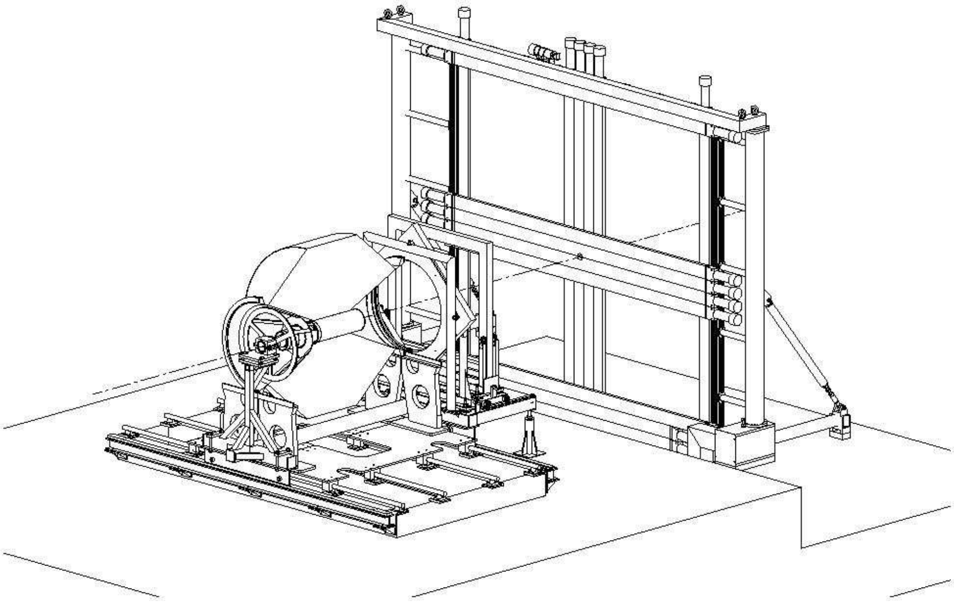

Figure 2.11: It is shown the LAGRANγE apparatus structure, we can distinguish the BGO calorimeter, the scintillator barrel, the plane wires chamber and the two layers (with vertical and horizontal bars) of the hodoscope wall

2.7.1 Central detectors

The multiwire proportional cylindrical chambers

The object of these detectors is to measure the direction of charged particles that leave the target after a nuclear reaction. Their information allow us to trace the trajectory of the charged particles detected. The two chambers, which have a cylindrical shape, surround the target along the z axis, and are placed one into the other. They cover the polar angle between 16° and 160°, the diameter of the internal and external chamber is respectively 10 *cm* and 17 *cm*. Their length is 40 *cm* and 50.5 *cm* respectively. The centre of both chambers is moved forward with respect to the centre of the target, and this increases the efficiency of detection of charged particles, which tend to be emitted in the forward direction in the laboratory frame. This is the well known relativistic effect called "Lorentz boost".

The frame of the chambers is composed of two shells 3 *mm* thick of polymetacrylic foam, a compound very light and stiff at the same time. The anodes are golden Tungsten wires, stretched alongside the z axis and having a diameter of 20 μm. The cathode are made by strips of Copper, large 3.5 *mm*, deposited on sheets of Kapton and separated from a distance of 0.5 *mm*. The Kapton foils are glued on both the internal and external shell of the chambers to form helixes wrapped up in opposite directions. Each cathode makes only one complete turn of the shell so crossing each anode wire only once. This technique allows to discriminate (in each MWPC) signals generated by the passage of more than one charged particle. The information provided by the chambers are necessary for the tracking of the charged particles, since the anode activated by the passage of a charged particle in gas in the chamber, allows us to reconstruct the azimuthal angle φ, while the information of the cathodic strips provide us the z coordinate and consequently ϑ.

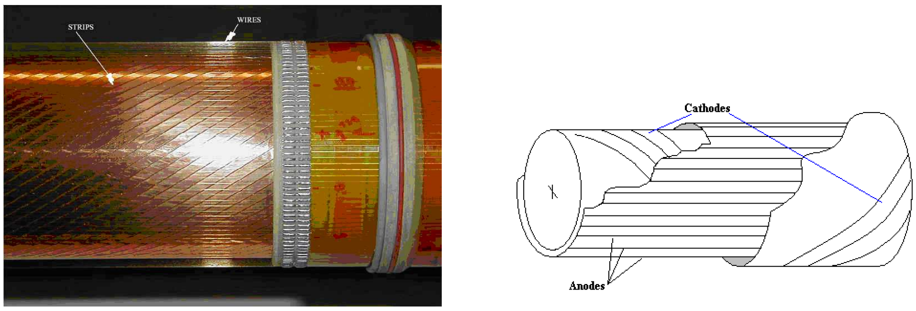

(a) Multi wire cylindrical chamber

(b) MWPS's scheme

Figure 2.12: We can see a photo (a) and a scheme (b) of the cylindrical chambers. Anode bands and cathode wire are evidenced.

dE/dx scitillator barrel

This detector is essential for measurement of the energy loss dE/dx of charged particles, has a cylindrical shape and consists of 32 plastic scintillator bars (NA102) which have a trapezoidal section. It is located around the MWCP's, each bar is placed along the z axis, has a length of 43.4 *cm* and a 5 *mm* thickness. Bars are read by a single photomultiplier placed to opposite ends to the direction of the gamma-ray beam. The internal radius of the barrel, and so its distance from the deuterium target, is 9.4 *cm*.

An electromagnetic calorimeter (see later) surrounds the barrel, and in this way a signal in it can be used to discriminate charged particles having a signal in coincidence between the two detectors, from the neutral particles that do not release signals in bars. In facts, due the little thickness of scintillators, only charged particles have high probability of depositing a certain amount of energy in the barrel.

The energy loss in the detector, in combination on the polar angle issued from the MWPC's or from the BGO calorimeter, can be used to calculate the energy lost per unit of path length. The bidimensional plot of the dE/dx versus the energy lost in the calorimeter allow to discriminate different kind of charged particles if they are not relativistic (MIP).

The time signal of this fast scintillators ($\tau \approx 2ns$) is used to distinguish the random events correlating the event generated on the target with the photon labelled by the tagger.

The BGO ball

The outer central detector is an electromagnetic calorimeter made of 480 scintillators which are composed of bismuth oxy-germanate ($Bi_4(GeO_4)_3$)[47]. Characteristic of this compound, called more simply **BGO**, is the presence of bismuth which has high atomic number (Z=83) and therefore a short radiation length, which allows the detection of high energy photons. There are other important properties of BGO that make it one of the best materials for the construction of scintillators: it is not hygroscopic and its light peak emission is about 480 *nm* (blue) which is the working point of most of the photomultipliers on the market.

The crystals (see figure 2.14(b)) have the shape of a truncated pyramid with flat section whose smaller basis, facing the target, is 2 *cm* long, while the large one has a length of 5 *cm*. The particular shape of the crystals has the advantage of optimising the collection of scintillation light emitted by the BGO. Examining the problem of the collection of light, we must take into account competitive aspects: if the light is emitted near the photomultiplier, the geometric efficiency is about 1/2, in facts the solid angle subtended is about the half of the total solid angle. However this efficiency compares with a limitation imposed by ray optics; the light ray in facts, enters in the photomultiplier window if (and only if) its angle of incidence is less than a limit angle defined by the relation:

$$\vartheta_{lim} = \arcsin \frac{n_2}{n_1} \tag{2.33}$$

Where $n_1 = 2.15$ and $n_2 = 1.45$ are the refraction index of the BGO and of the window respectively. Relation 2.33 implies that the light must also be emitted with an angle ϑ with respect to the crystal axis smaller than $\vartheta_{lim} = 41.7°$.

On the other side, if the light is emitted in a point far from the photomultiplier window, it will hit on the walls of the crystal with an angle that depends from the shape of the crystal. If the side walls were perpendicular to the bases, a ray emitted at a angle ϑ with respect to the crystal axis, will strike the wall with an angle of incidence defined with respect to the normal to the wall and given by:

$$\vartheta' = \frac{\pi}{2} - \vartheta \tag{2.34}$$

and would be reflected with this angle only if this angle is smaller than the limit angle crystal-air that is $\vartheta_{lim}^{air} = 27,7°$. This second limit angle implies an emission angle for the light: $\vartheta \leq \frac{\pi}{2} - \vartheta_{lim}^{air} = 62,3^{\circ}$ The angle ϑ'' at which the ray hits on the surface of exit from the crystal is the complementary of ϑ' so $\vartheta'' = \vartheta$ and as said before, the light would be collection only if $\vartheta \leq \theta_{lim}$ and it is clear that this condition is never satisfied. Tilting the wall of BGO by an angle β with respect to the crystal axis, the angle of incidence on the wall and therefore the angle of reflection is:

$$\vartheta' = \frac{\pi}{2} - \vartheta + \beta \tag{2.35}$$

which corresponds to an angle of impact on the photocathode:

$$\vartheta'' = \frac{\pi}{2} - \vartheta' + \beta = \vartheta - 2\beta \tag{2.36}$$

and for a ray that is reflected **n** times:

$$\vartheta'' = \vartheta - 2n\beta \tag{2.37}$$

Therefore the particular shape of the crystals allows the reflected light to enter in the photomultiplier even if it is emitted with angles greater ϑ_{lim}.

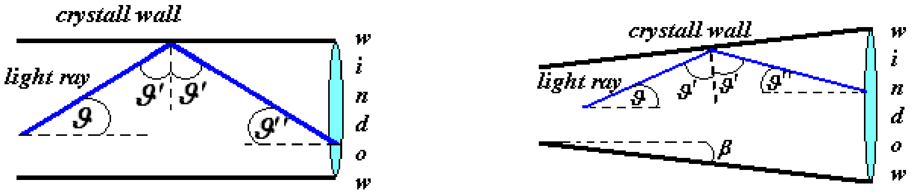

(a) Crystal with parallel side walls. The emitted ray is reflected with the same incident angle ϑ' which is the complementary of light emission angle ϑ so $\vartheta'' = \vartheta$

(b) Crystal with tilted wall. The emitted ray is reflected with the same incident angle ϑ' but $\vartheta' = \frac{\pi}{2} - \vartheta + \beta$ ant then the angle of incidence on the PM window is $\vartheta'' = \vartheta - 2\beta < \vartheta$ (focusing effect).

Figure 2.13:

The problem now is to optimise the collection of light that is not uniform inside the crystal. In fact, multiple reflections along the walls of scintillator, with the pyramid shape and the focusing effect due to the high refractive BGO index ($n \sim 2.2$), allow to the light emitted far from the photocathode has more chance to enter in it than that emitted close to it. Some studies have pointed out that about 30% of the emitted light arrives at photomultiplier by multiple reflection inside the crystal. Consequently, if the walls of the crystal are glossy, it has a greater collection of light but a less uniformity of the response. To equalise the uniformity, all crystals surface have been made less polished. This technique has the effect of lessening the light to every impact. At this point, longitudinal uniformity has been measured with automatic procedure to check that it was at least 95%.

The BGO calorimeter is designed to detect photons with energy up to 4 GeV with a resolution in energy between 2 and 3%. The total energy resolution for a photon with an energy E_γ is:

$$\Gamma(FWHM) = \sqrt{a^2 + (\frac{b}{E_\gamma})^2 + (\frac{c}{\sqrt{E_\gamma}})^2} \tag{2.38}$$

where $a = 0.17$ is a constant term, $b = 0,97$ is the noise and $c = 2.36$ is the statistical term. The constant term a includes the fluctuation in the energy leakage, the non-uniformityes in the crystal response, the intercalibration uncertainties and the thermal term evaluated with the temperature control system. At $E_\gamma = 1\ GeV$ energy resolution is $\Gamma \simeq 2\%$

The angular resolution of the detector is $\Delta\vartheta \approx 3^\circ \div 5^\circ, \Delta\phi \approx 11^\circ$, values compatible with the limited number of sectors. BGO calorimeter is able either to detect hadrons, but in this case nuclear interactions steal energy to scintillation mechanisms and the resolution decreases.

The geometry of the detector has been designed so that each particle coming from the target crosses 24 *cm* (corresponding to 21 radiation lengths) of active material in all directions. The 480 crystals are divided into 15 crowns with 32 scintillators (figure:2.14(d)); the main structure is composed of 24 baskets (3 in ϑ and 8 in φ) of Carbon fibre each containing 20 crystals (5 in ϑ and 4 in φ). The choice of carbon fibre is dictated by its rigidity and for it low gamma ray attenuation due it low Z number. Internal and external walls are of 0.38 *mm* and of 0.54 *mm* thick respectively. In order to minimise the quantity of inert material that separating the crystals. Baskets are kept together by a structures that allows to separate the calorimeter into two halves, in order to make accessible the central region.

2.8 Study of the BGO characteristics

The BGO calorimeter characteristics have been investigated, moreover has been developed an automatic technique for calibration and monitoring of the gain in order to always know the absolute calibration.

2.8.1 Temperature dependence

The BGO light output is known to decrease with increasing temperature that change the efficiency of energy conversion in light of scintillation. This variation was measured in a wide temperature range, a linear fit on the data collected allowed to assess a change of the order of 1,28% for Celsius degree around room temperature. Since a thermostatic regulator of the calorimeter is not possible due its compact geometry, it was necessary to keep under control the crystal temperature in order to estimate the possible variation of energy calibration. The detector was equipped with

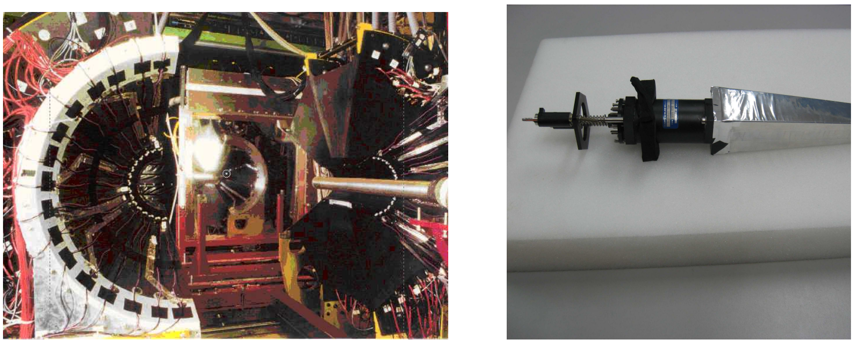

(a) The BGO calorimeter opened (b) One BGO crystal

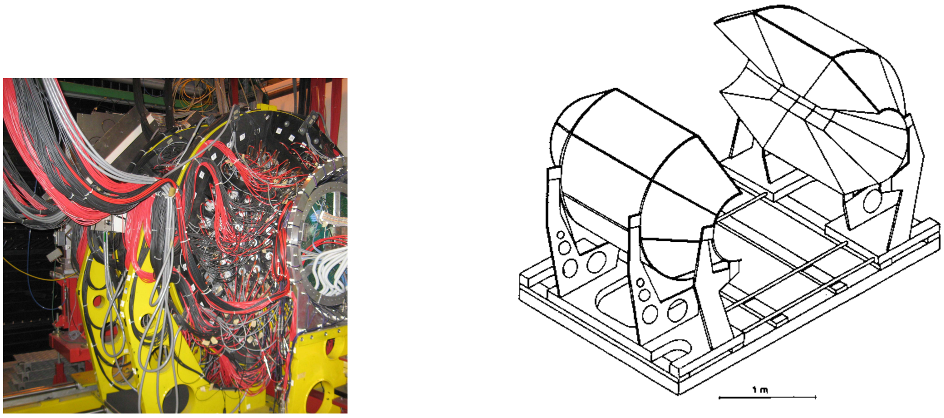

(c) The BGO calorimeter closed (d) The calorimeter scheme

Figure 2.14: Pictures (a) and (c) shows the electromagnetic BGO calorimeter separated into two halves and closed respectively. Picture (b) shows one of the 480 BGO crystal which form the calorimeter. We can see the typical pyramid shape and the photomultiplier. Figure (d) underline the baskets structure of the calorimeter.

thermal probes to record the temperature during data taking. A study of temperature changes has shown that during acquisition [48] [49], once led the calorimeter to working temperature, variations on the efficiency are negligible. The thermal contribution to the total energy resolution is about $\mathcal{F}_T \simeq 0.4\%$.

2.8.2 Calibration and automatic procedure of signal equalisation

The absolute calibration is obtained, with photons of 1.27 MeV in energy emitted from a source of Na^{22} placed inside the detector. During the calibration, attenuation on the photomultiplier signal is turned off e the peak position on the ADC, generated by photons, is registered. Therefore the response of each of the 480 crystals is equalised by an automatic procedure which, changing the applied voltage, adjust the gains of photomultipliers and sets the peaks of the ADC spectra ta a fixed channel.

If we call c_{eq} the selected channel, we can tell that the equalisation is achieved when all ADC channels ($c_i = 1, ..., 480$) are in the following range:

$$\left| \frac{c_i - c_{eq}}{c_{eb}} \right| \leq B(\%) \tag{2.39}$$

where $B(\%)$ is the precision of the procedure. To maintain the time necessary for the equalisation below the value of about one hour, the value $B(\%) = 1.5\%$ is fixed. This number only influence the value of the energy sum of all the crystals obtained through a hardware adder that drives the trigger of the experiment, but does not offer the absolute calibration resolution because in the data analysis the exact values of the calibration constants are used for the ADC-energy conversion. The choice of the equalisation channel is determined by the maximum value of the energy that must be measured, by the range within which the detector response is linear and by the effects of saturation of photomultiplier. A reasonable compromise between these factors [50] and the precision of calibration has led to the choice $c_{eq} = 64$.

2.8.3 Linearity

The automatic calibration procedure of the calorimeter in use at GRAAL is simple, fast and very efficient. In fact, it allows to determine the absolute calibration constants in less than 15 minutes and is repeated two times per day, typically while data collection is stopped for the injection of new electrons in the storage ring. The extrapolation of the calibration from the region of MeV, typical of the gamma sources which have been used, to the GeV range corresponding to the typical energies released in crystals by photons produced in the photonuclear reactions, on the contrary requires an accurate calculation of the possible non-linear deviations of electronics chain in this wide range of energy.

Using impulsed light produced by 7 led (see later 2.8.4) which could be varied of three orders of magnitude by a programmable amplifier with steps of 0.25dB, curves of linearity have been obtained for each crystal of the calorimeter. The intensity on the pulse of light on every crystal was normalised to the response reference detector of which was previously verified the excellent linearity. This allows to apply the correction factors to the measure of the energy (greater than 0,1%).

In this way it can be possible extend the absolute calibration obtained with 1.27 MeV Na^{22} gamma source, at GeV range, the result is a calibrated light source that cover a range of 1000:1.

2.8.4 Monitoring system

The calibration constant of each BGO crystal can change as a function of time for two reasons. Temperature effects in the crystal emission of the light are negligible. A change in the photomultiplier gain that can depend on the instability of high voltage or on cathode and dinodi deterioration, or on temperature variations too. To control the possible variation of the calibration constants a monitoring system, shown in picture 2.15, was built [50]. The system is composed by 7 led, one sphere that integrates and distributes the led light to 600 optical fibres. The fibres carry the pulsed leds light to the BGO crystals and to a reference NaI detector which is continuously calibrated by radioactive rising of Caesium 137. Studying the crystals response and normalising these with the variations of the led light, we can know the calibration constants variations. This procedure works two times a day, during the refill while the electrons are re-injected in the storage ring and the data taking is stopped. A software collects the data about calibration constants variations which are used in the data analysis to correct the calibration.

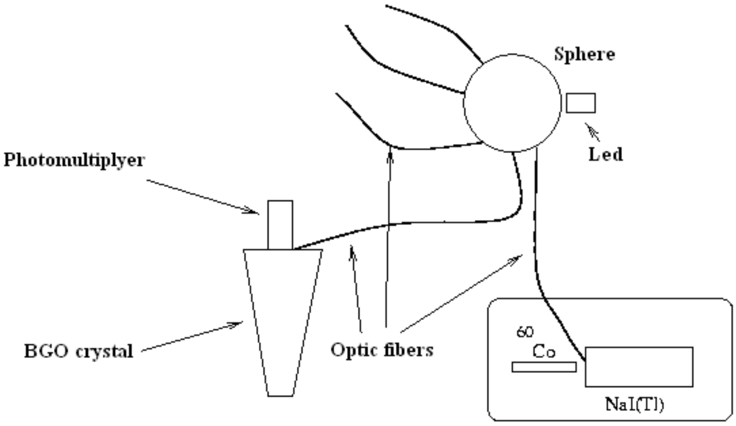

Figure 2.15: The scheme of the monitoring system.

2.8.5 Electromagnetic shower in the calorimeter

To investigate the performance of the BGO crystals for electromagnetic shower detection, one basket with 20 crystal was studied with the PHOENICS photon beam at the Bonn university [51]. Energy spectra for 258 MeV incident gamma-ray beam energy on the crystal basket were analysed. In figure 2.8.5 are shown the ADC spectra for the central crystal alone (c_{10}) (2.16(a)), for the software sum of the central 3x3 crystal matrix (Σ_9) (2.16(b)), for the software sum of the entire basket (Σ_{20}) (2.16(c)) and for the hardware sum (2.16(d)). It is clear that the best energy resolution is obtained with the hardware sum of the 20 BGO crystals; this is due to a software threshold (10 ADC channels corresponding $\approx$ 6 MeV) that was introduced in the data acquisition program in order to reproduce the GRAAL experimental set-up.

Crystal design allows a complete longitudinal electromagnetic shower containment. I this condition the resolution of the calorimeter mainly depends on the lateral energy loss, we have studied the energy dependence of lateral containment of shower by comparing the quantities (c_{10}/Σ_{20}) and (Σ_9/Σ_{20}). The results in figure 2.17 show that the central crystal contains already 80% of the shower energy, while the 3x3 matrix contains from the 95% to the 99% of the shower.

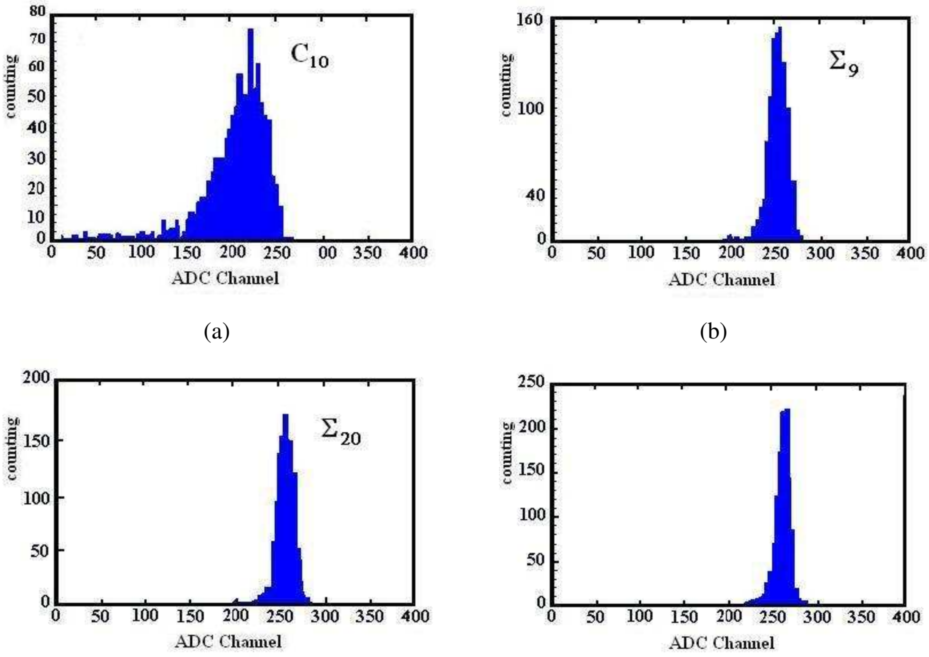

(a) (b)

(c) (d)

Figure 2.16: Spectra at 258 MeV incident energy photon.

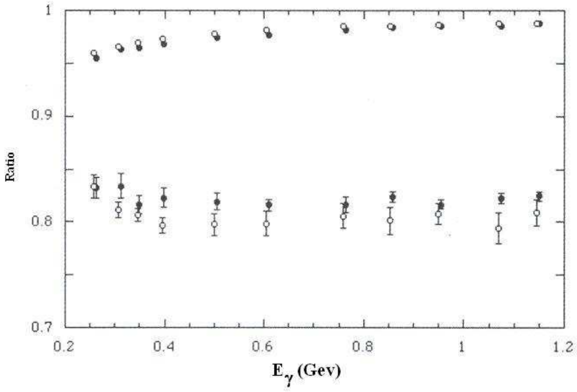

Figure 2.17: (c_{10}/Σ_{20}) and (Σ_9/Σ_{20}) values as a function of the incoming photon energy. Open point are data, full point are Montecarlo simulation. Full point are slightly shifted by 4 *MeV* for better visibility. When not visible, error bars are within the data point spot.

2.8.6 Forward detectors

The multiwire plane chambers

These two detector, are necessary for tracking of charged particles, are composed of two planes of wires (3 *mm* distance between two wires) with perpendicular directions. The first chamber has the wires oriented in the *x,y* direction while the second one in the so-called *u,v* direction at 45° respect *x-y* plane, in order to resolve the ambiguities when more than one charged particle ie emitted in forward direction.

The chambers are respectively 93.4 and 133.2 *cm* far from the target centre. Each plane is composed of gilt tungsten wires, placed between aluminized mylar cathodes. The dimensions are 960 x 960 mm^2 for the *x-y*, 1152 x 1152 mm^2 for *u-v* and their have respectively 320 x 320 and 384 x 384 wires. The space between each cathode is 10 *mm* and is filled in with an Argon-Ethane mixture (85% and 15%, respectively). A 2400 *V* voltage is applied to the wires. Under these conditions the efficiency is close to 100% and the position resolution is comparable to the wire distance.

The scintillator hodoscope

Just behind the plane chambers there is a 3 x 3 m^2 plastic scintillator wall which identifies charged particles in the forward direction. The wall is made of by two layers of 26 scintillator bars (figure:2.18) respectively vertically and horizontally oriented and it measures time of flight (TOF)on a 3 *m* distance from the target and the energy loss of charged particles. Each bar is composed of NE110A, is 11.5 *cm* wide, 3 *cm* thick and has a a photomultiplier on both extremities.

The particular structure of this detector allows the localization of detected particles, in fact vertical bars hit gives the *x* coordinate while the horizontal gives the

y one. If only one layer is hit, the missing coordinate can be recovered by the difference between the time that signal employs to arrive at the two photomultiplier on the ends of the bar.

The time of flight resolution is $\mathcal{F}_{TOF} = 600\,ps$ for ultra-relativistic particles, the detection efficiency is 100% if the particle energy is greater than a few MeV. The scintillator hodoscope allows to discriminate charged particles from neutral particles which do not leave signal in it, but only in the following detector (see later) and it allows, by the study of relation between TOF end energy deposited (ΔE), to discriminate between protons and pion too. If we know which kind of charged particle did hit the wall, we can calculate his energy using his TOF, in fact:

$$E = m\gamma \text{ with } \gamma = \frac{1}{\sqrt{1-\beta^2}} \text{ and } \beta = \frac{D}{c \cdot TOF} \tag{2.40}$$

where D is the distance between the point in the wall where the hit is detected and the target. Two central modules (for each layer) have half-circle holes (6 cm diameter) to allow the passage of the beam.

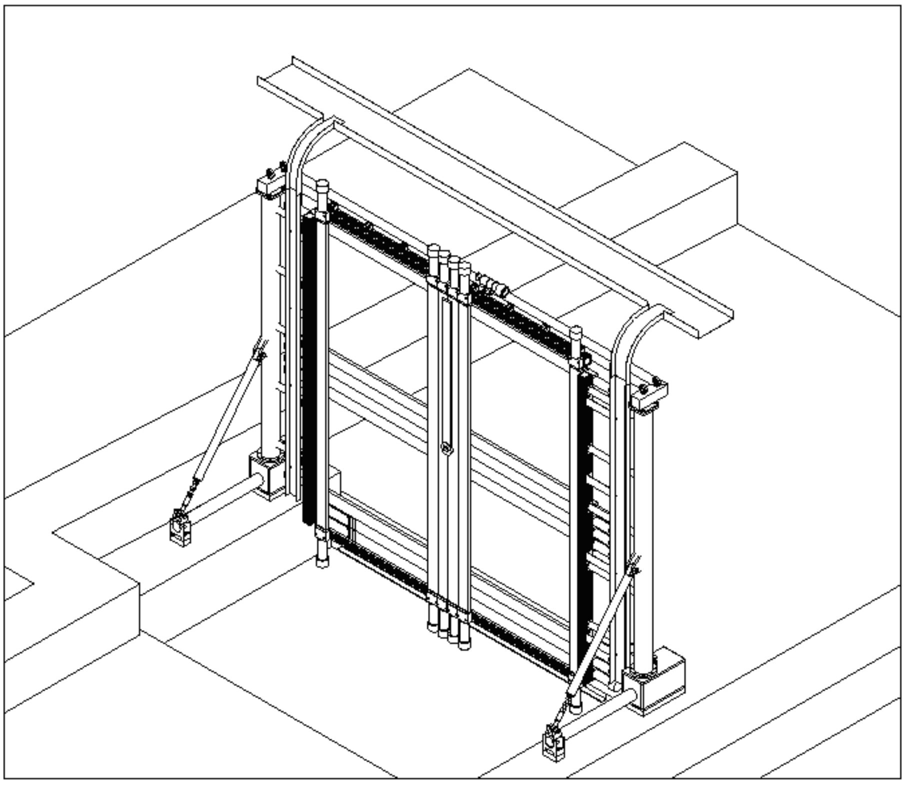

Figure 2.18: The hodoscope wall

The shower wall

A large acceptance lead-scintillator time-of-flight wall has been installed to detect photons and neutrons. The wall is an assembly of 16 modules, vertically mounted and covering all together a sensitive area of $3 \times 3\,m^2$. The module, aligned with respect to the beam are fixed $3.3\,m$ from the target. Each module is a composition of four $4 \times 19 \times 300\,cm^3$ scintillators bars, separated by 3 layers 3 mm thick of lead converter. The efficiency of the neutron detection has been evaluated with simulation and it is about 22% for a 10 Mev threshold. A photon efficiency of 92-95% was obtained with the help of a iron table positioned forward and that allow the conversion of the photons. The discrimination between the two different kind of neutral particles is obtained by the TOF. A detailed description of the shower wall and it features is reported in [52].

2.9 Data acquisition system

The GRAAL experiment acquisition system (called SAGA[3] [53]) is a hardware event builder which associates compact programmable ASIC[4] type electronics and standard electronics read by a FERA[5] bus. ASIC circuits allow analog to digital signal processing for many types of particle detectors, such anode wires and cathode strips of MWPCs, and drift chambers and also the photomultipliers. The electronics is directly placed on boards and connected to the detector in order to reduce the number of interconnections and, therefore, the risk of failure due to connectors. The data transfer is performed by a 32 bit ECL bus linking all the detectors, a SUN workstation controls all detector settings by the ASIC bus. Once the buffer is transferred in the shared SUN memory, it can be recorded on tapes (10 *Gbyte*) of size or processed by the spectra building program, running on the station.

Five of the twelve detectors (tagger, barrel, shower wall, spaghetti, thin monitor) are controlled by the FERA electronic system. Their calibration and monitoring is performed by a traditional CAMAC system on an Alpha Station, operating with VMS. FERA bus is read by the ASIC bus through the FASIC module, a C program has been written to set the parameters (as thresholds, delays, amplitudes, etc.) of electronic modules located on different boards. It runs on the SUN station with a powerful graphical interface called SL-GMS.

The data acquisition time depends on the largest conversion time (4 μs for the audio converter), on the bus speed (5 ns/m) multiplied by two VME period ($125ns$). For about 100 events this time amount at $17,5\mu s$, giving, in this way, a transfer rate of about 23 $mbyte/s$, that has to be compared to the ETHERNET transfer limit ($600Kbyte/s$). The trigger frequency being about 200 Hz, the number of lost events is thus negligible.

---

[3] Systéme Acquisition Graal Asic

[4] Aplication Specific Integrated Circuit

[5] Fast Encode Readout ADC

2.9.1 The trigger

The acquisition system is composed of different triggers, which comes from either physical or beam events. All of them are in coincidence with the tagging detector. An energy deposition in the BGO larger than 120 MeV in coincidence with an electron signal in the tagging detector, triggers the data acquisition for the physical events.

In figure 2.19 is shown the scheme of the BGO-tagger trigger. For each crystal crown of the BGO calorimeter, the 32 photomultiplier signals are sent to a mixer (C.A.E.N. 5Y493). Each signal is attenuated and duplicated: one of the signals (A) is used to enable the acquisition, while the other signal (B) is delayed by $300\,ns$ and then sent to ADC. The sum of the 15 crows are added all together to obtain the value of the energy deposited in the calorimeter. If this sum is greater then 120 MeV, it is sent to a constant fraction discriminator that transform it to a time-window. If there is a logical coincidence between this time-window and a signal in the tagger, the acquisition is enabled. This energy threshold eliminates almost all the electromagnetic background radiation from the target and it is used for the photoproduction of meson that decay into photons.

Channels with three charged particles are triggered by the following conditions: at least two particles in the forward hodoscope and at least one particle in the central barrel. This trigger allows to study the photoproduction of strange meson ($K\Lambda$ and $K\Sigma$) as well as the charged decay of other mesons (η, ω).

Two other triggers rule the beam acquisition: the first is the coincidence between the second and third scintillator of the thin monitor in anti-coincidence with the first one. The second is an energy threshold on the *spaghetti*. Another trigger starts events with thin monitor and *spaghetti* detector coincidence. These triggers allow to calculate the monitor efficiency and the beam flux.

2.9.2 Data taking

Each period of data taking is divided into runs. The run length is about four hours long, depending on the trigger and on the intensity of the laser line. During each run the two laser states are alternated with the bremsstrahlung mode. The timing is:

- ➟ 20 minutes for horizontal polarisation;
- ➟ 18 minutes for vertical polarisation;
- ➟ 5 minutes for bremsstrahlung.

For each trigger and each polarisation or bremsstrahlung state, the acquisition records on a module of scales the total number of events. In particular the monitor, *spaghetti*, and time scales are read to calculate the beam flux for each of the three states.

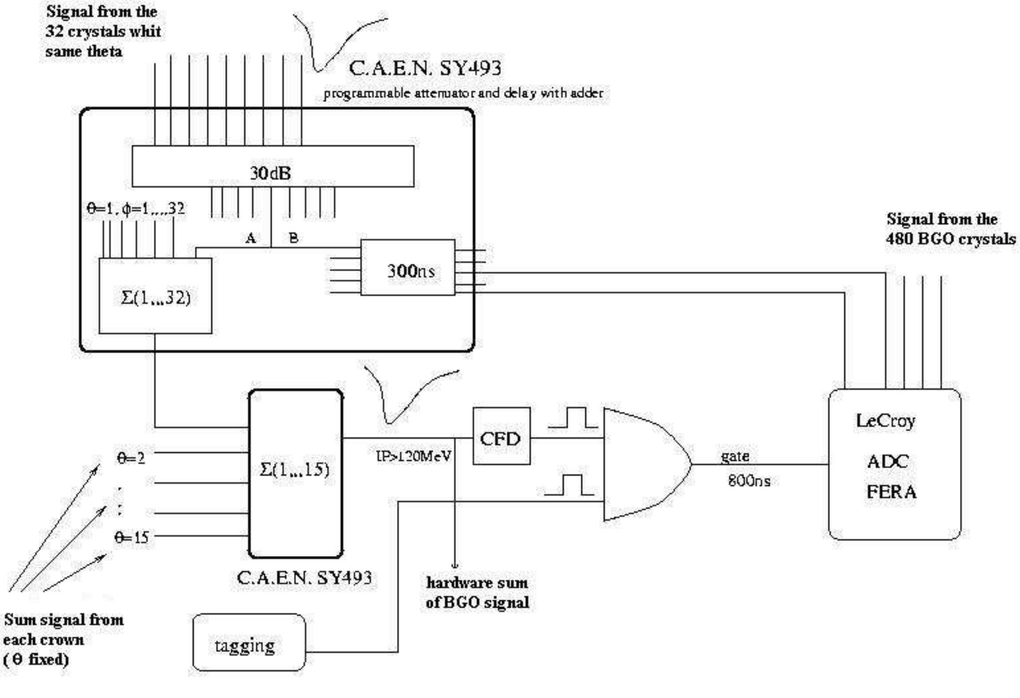

Figure 2.19: Trigger BGO-Tagger

Chapter 3

Simulation and analysis software

3.1 Introduction

In this chapter the chain of software codes used for data analysis and for photoreaction simulations are described. We will describe in higher detail which have been specifically developed for the study of deuteron photodisintegration.

The analysis codes are written in **FORTRAN77** language,which is suitable for the implementation of mathematical equations. The software output is arranged in a variable length vector set (*n-tuple*), compatible with the graphical analysis software PAW [54] .

Figure 3.1 shows the software codes chain scheme of the GRAAL experiment. Simulated and experimental data are arranged in the same format by the two upper branches of the chain, and they converge in Prean code. This allows to analyse them and coherent comparison between simulation and experiment.

3.2 Simulation software

The two codes Laggen and Lagdig form the simulation software chain. The Laggen output file (*namefile.hit*) contains all physics information (such as energy loss, time of flight, etc.) that are originated by the particles in the detectors. With the Lagdig code, we study the apparatus response and, using the calibration curves of each detector, we generate the digitalised output (ADC, TDC, etc.) in the same format of the output of data acquisition software. In the Lagdig code all the experimental effects which can influence the detector response, such as experimental resolutions or the signal attenuation inside the detectors are inserted.

3.2.1 Laggen

This simulation software is composed of two parts: an events generator that simulates the photonuclear interaction of the GRAAL beam inside the target; the Geant

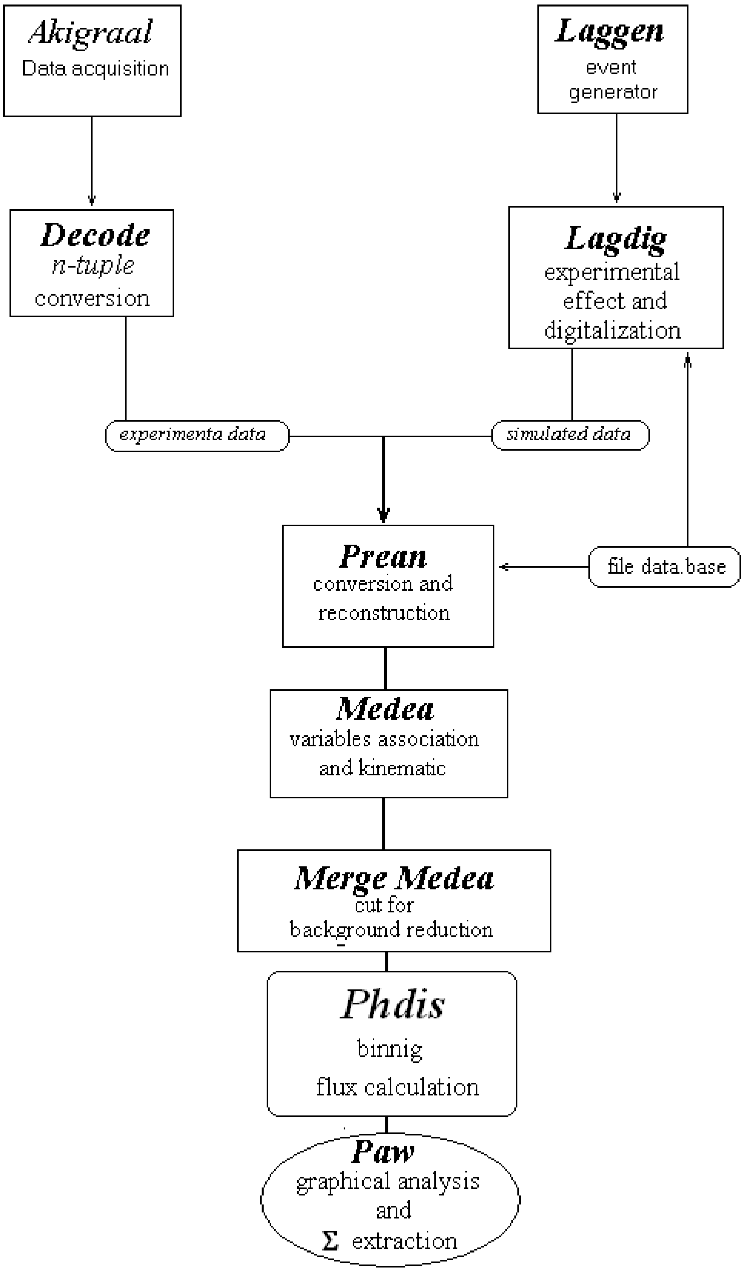

Figure 3.1: GRAAL software codes chain.

package (release 3.2.1) [55] used to describe the LAGRANγE apparatus and to simulate particles interaction with all detectors.

The event generator is a Montecarlo code and it was written for the GRAAL experiment. It extracts the incoming photon energy following the experimental shape of the collimated Compton backscattered gamma-ray beam (figure:3.2. Then it uses this energy value to initiate photoreaction generation routine.

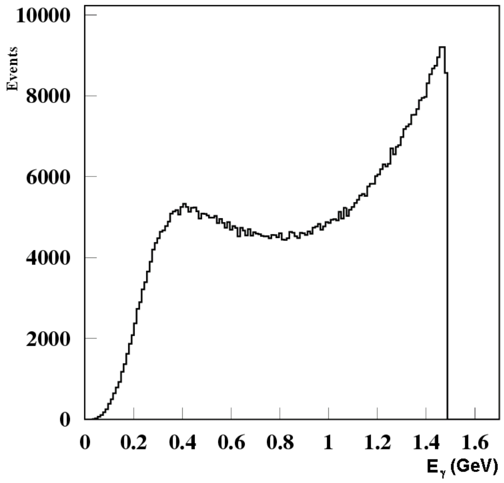

Figure 3.2: The figure shows the tipycal Compton energy spectrum used by the events generator to extract the energy of incoming photons.

The generator [56] allows to simulate 23 reaction channels on the proton, 14 on the neutron, 3 coherent reactions on the deuteron and 4 on the ^3He. All reaction channel are listed in table 3.1. Total and partial cross sections of many reactions are well known with a precision of about 10% therefore data used by the generator are derived from the literature. For those reactions having a small cross section and for which the literature data are scare, the total cross sections are arbitrary set at 1 *μbarn* on the whole energy spectrum. The 37 channels on the single nucleon, present in the event generator, correspond to all known reactions in the GRAAL energy range ($0.6 \div 1.5$ *GeV*).

An input file (*laggen.dat*) contains the specific requests of the simulation parameters: the reaction channel, the laser line, the target length, the number of events. Many other kind of parameters such as a specific angle for the final particle emission or a specific incoming photon energy may be chosen. Simulation of many channels simultaneously is also possible.

The code starts extracting the incoming photon energy and calculating the total energy in the initial state being the target fixed as an input parameter. In the case that more than one channel is simulated, each reaction channel is extracted with a probability that is obtained as the ratio of the total cross sections of that reaction to the sum of the total cross section values of all selected reactions. The vertex of the reaction is extracted according to the convolution of the gamma-ray beam and the target shapes Energy and emission angle of the final state particle are extracted according to the differential cross section data.

Information provides by the photonuclear simulation routine are transferred to the the Geant package, that simulates for each outgoing particle, the propagation inside the active materials of the detectors. The geometry and the materials which form the apparatus, are described in detail inside specific routines. Geant describes for each final state particle, the electromagnetic interaction with the detectors and uses the Fluka [57] and Mikap [58] codes for the adronic interactions. If a particle in the final state is unstable, the package simulates its decay and follows the dacay products in their interaction with detectors.

The program termitates when the number of simulated events is equal to the value fixed in the *laggen.dat* file. Laggen provides an output file with an n-tuple format that can be analysed using the Paw package.

Index	**Reaction**	**Index**	**Reaction**
1	$\gamma + p \rightarrow \pi^+ + n$	23	$\gamma + p \rightarrow \pi^+\pi^- + \pi^0 + p$
2	$\gamma + p \rightarrow \pi^0 + p$	24	$\gamma + p \rightarrow \pi^+\pi^+ + \pi^+ + n$
3	$\gamma + n \rightarrow \pi^- + p$	25	$\gamma + n \rightarrow \pi^+\pi^- + \pi^0 + n$
4	$\gamma + n \rightarrow \pi^0 + n$	26	$\gamma + n \rightarrow \pi^+\pi^- + \pi^- + n$
5	$\gamma + p \rightarrow \Delta^{++} + \pi^-$	27	$\gamma + p \rightarrow \pi^+\pi^+ + \pi^- + \pi^- + p$
6	$\gamma + p \rightarrow \Delta^+ + \pi^0$	28	$\gamma + n \rightarrow \pi^+\pi^+ + \pi^- + \pi^- + n$
7	$\gamma + p \rightarrow \Delta^0 + \pi^+$	29	$\gamma + p \rightarrow \Lambda + K^+$
8	$\gamma + n \rightarrow \Delta^+ + \pi^-$	30	$\gamma + p \rightarrow \Sigma^0 + K^+$
9	$\gamma + n \rightarrow \Delta^0 + \pi^0$	31	$\gamma + p \rightarrow \Lambda + K^0 + \pi^+$
10	$\gamma + n \rightarrow \Delta^- + \pi^+$	32	$\gamma + p \rightarrow \gamma + p$
11	$\gamma + p \rightarrow \rho^0 + p$	33	$\gamma + p \rightarrow \eta' + p$
12	$\gamma + p \rightarrow \rho^+ + n$	34	$\gamma + p \rightarrow \pi^+\gamma + n$
13	$\gamma + n \rightarrow \rho^- + p$	35	$\gamma + p \rightarrow \pi^0\pi^0 + p$
14	$\gamma + n \rightarrow \rho^0 + n$	35	$\gamma + p \rightarrow \gamma + p$
15	$\gamma + p \rightarrow \pi^+\pi^- + p$	36	$\gamma + p \rightarrow \phi^0 + p$
16	$\gamma + p \rightarrow \pi^+\pi^0 + n$	37	$\gamma + p \rightarrow K^+ + K^- + p$
17	$\gamma + n \rightarrow \pi^+\pi^- + n$	51	$\gamma + d \rightarrow \pi^0 + d$
18	$\gamma + n \rightarrow \pi^0\pi^- + p$	52	$\gamma + d \rightarrow p + n$
19	$\gamma + p \rightarrow \eta + p$	53	$\gamma + d \rightarrow \eta + d$
20	$\gamma + n \rightarrow \eta + n$	55	$\gamma +^3 He \rightarrow \Delta^{++} + n + n$
21	$\gamma + p \rightarrow \omega + p$	56	$\gamma +^3 He \rightarrow \pi^0 + d + p$
22	$\gamma + n \rightarrow \omega + n$	57	$\gamma +^3 He \rightarrow \pi^+\pi^- + d + p$
		58	$\gamma +^3 He \rightarrow Dibarion + p$

Table 3.1: Reactions channels allow by the events generator. The index on the left is the value that must be inserted in the *laggen.dat* file to select the reaction.

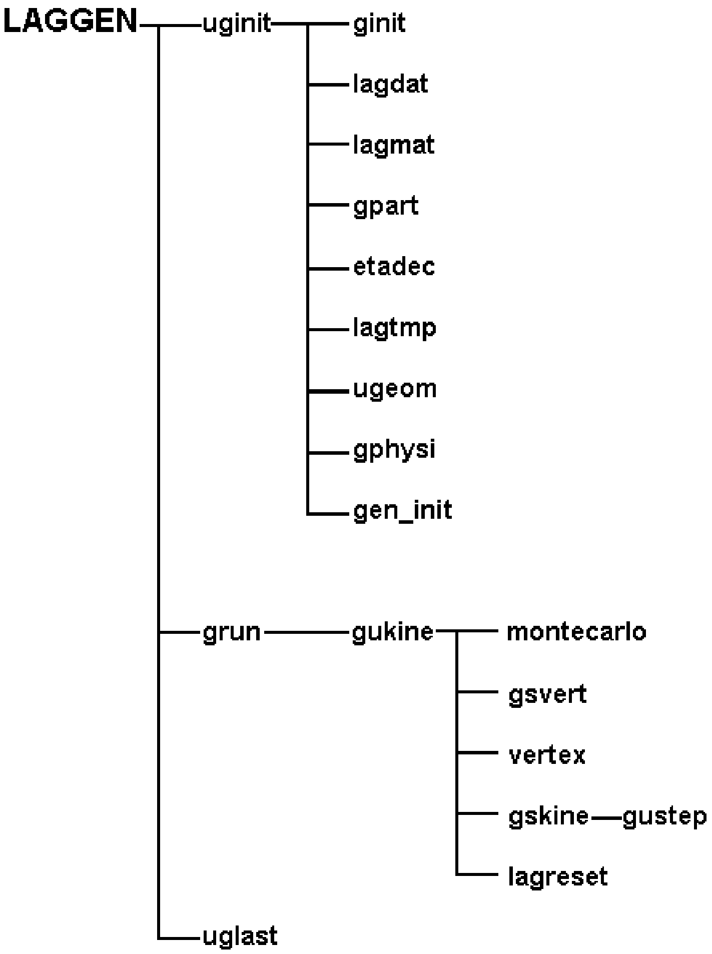

Figure 3.3: The LAGGEN routines scheme. We see the two main parts: *uginit* for the description of the apparatus and *grun* for the events generation and their interaction with the detectors.

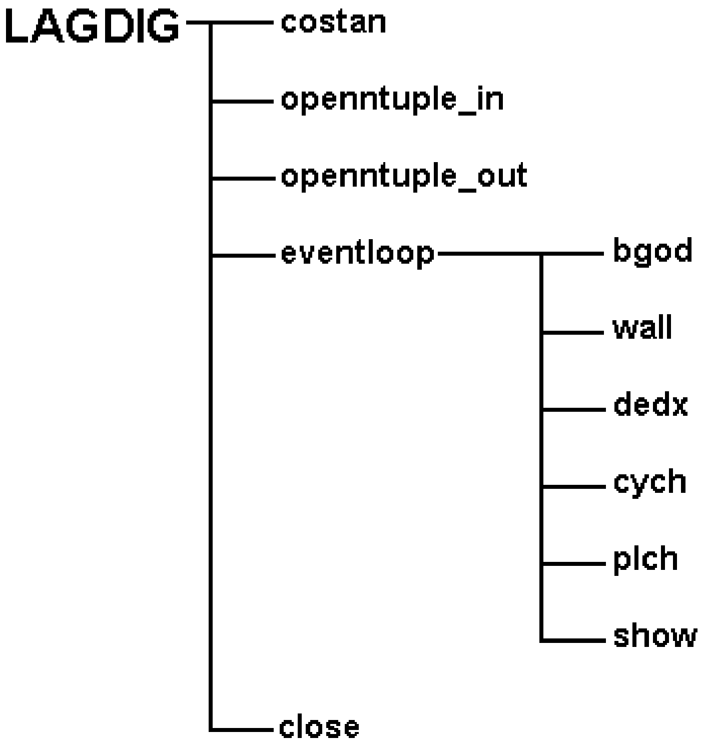

Figure 3.4: The LAGDIG routines scheme.

3.2.2 LAGDIG

The LAGDIG code simulates the electronic response of the LAGRANγE apparatus to the events generated by LAGGEN. It take into account all the experimental effects connected with the intrinsic detector response, such as light attenuation, dispersion and all the effects due to electronic treatment of signal such as electronic noise or signals fluctuations. The output file contains the digital response of each detector: ADC and TDC converted for each the scintillators, logical data for wire chambers, etc. The output file is written with the same logic of the *n-tuple* file produced by DECODE (pra: 3.3), except for some simulation variables that are saved in specific memory blocks.

LAGDIG contain a routine (*costan*) (fig:3.4) that reads the files *data.base* which specifies for each detector: alignment parameters of the LAGRANγE apparatus, the detectors efficiency, threshold discrimination, detector ADC conversion constant. The same information's are used in LAGGEN for the simulation of the physical response of detectors and in PREAN for the reconstruction of the event physical variables (see3.4).

The main routine *eventloop* iterates on the events. This routine uses some of the digitalization subroutines specifically written for each detector. From the gamma-ray energy the distance of the Compton scattered electron from the the electrons beam main orbit is calculated. From this information the corresponding $\mu-$strip channel of the tagger detector is calculated. Separate code (called BEAM) simulates the electron beam trajectories inside the storage ring in order to know the spatial distribution of the scattered electrons on the tagger $\mu-$strips. This distribution is used inside LAGDIG to take into account the experimental spatial spread of the electrons.

The second step is the analysis of BGO response, (routine *bgod*). For each BGO crystal, the pedestal corresponding to the centre of the ADC peak obtained in absence of signal due to the noise of electronic chain is written in the calibration file. The software subtracts this pedestal from the ADC channel so that the channel 0 corresponds to the absence of signal. The half width of the peak (about 3 channels at 2.2 MeV) is the threshold above which is possible to distinguish a signal from the noise. The value of this threshold is imposed on the simulated signal inside the calorimeter crystals in order to consider only the crystals in which the energy deposited is greater than this limit. Then, knowing the conversion factor a between energy deposited and the ADC channel, the respective ADC channel is assigned to each crystal by the relation:

$$ADC = aE_i^{dep} \tag{3.1}$$

where E_i^{dep} is the energy deposited in the i-th crystal.

LAGDIG analyses then the response of the hodoscope wall, of the scintillator barrel and of the shower wall using the corresponding routines *wall, dedx* e *show*. The procedure is the same: the energy lost in the plastic scintillator (E^{dep}) is converted into scintillation light which fraction of which reaches the photomultipliers (one for each scintillator in the barrell and two for each one in the walls). The signals are attenuated by a factor which depends on the particle impact point, then they are retarded too. In fact, the scintillation light has to travel across the plastic bar but the emitted light intensity decays exponentially as a function of the distance from the photomultiplier.
If:
x = distance impact point-photomultiplier;
L = plastic length;
β = attenuation constant
the light that may arrive to the photocathode is equivalent to an energy given by the law:

$$E(\vartheta, x) = E^{dep} \cdot e^{-\beta \frac{x}{L}} \tag{3.2}$$

then the ADC channel will be:

$$ADC = bE = bE^{dep} \cdot e^{-\beta \frac{x}{L}} \tag{3.3}$$

where the parameter b is experimentally determined.

In the case of the two walls, the program also takes into account the case that two signals are produced at the same time in the same bar. In this case, the energy detected will be the sum of the two particles lost energy, while for the time of flight we choose the smallest. For both walls is also taken into account the attenuation due to the hole in the central bars.

In the last step, LAGDIG studies the cylindrical (*cych)* and plane (*plch)* chambers. From the localization of the energy lost in the gas, the program determines the wire mainly stimulated by the electromagnetic avalanche. For the cylindrical chambers, charge distribution on each cathode is calculated considering the avalanche statistical dipersion. Electronic gain and dispersion are applied on each strip, then the value of the main strip is recorded with the near ones.

3.3 DECODE

The files coming from the LAGRANγE acquisition system, contain the entries of each photonuclear event with the informations about the start time and the counting scale for both polarisation states and the ASIC and FERA setting.

DECODE software digitises data in a CWN (Column Wise Ntuple) file, which can be read by PAW package and allows automatic data compression. The code records the data without selection but it checks the correct acquisition data structure. At this point the program creates a specific BGO calibration file and control file for each detector. The run is now ready to be processed by the preanalysis program.

3.4 PREAN

This program uses detectors calibrations files separately provides run by run on the digital experimental data provided by DECODE program, or by LAGDIG simulated data. This code has been written to reconstruct the physical variable associated to the signal in the detectors. As seen at 2.5.2, the tagger plastics signal is associated with a Compton backscattering event only if it is in time with the corresponding nuclear event in the experimental hall. Using the PREAN we can also study data recorded as out of time on the tagging

As in LAGDIG, there is a routine (*constan*) which reads the file containing calibration data and all the information for analysis. For experimental data the program uses specific calibration files for each *run*; for simulation files PREAN uses always the same calibration file that LAGDIG uses for the simulation. The *data.base* file there provides a threshold value for a single BGO crystal, this allow to consider only the crystal response that has an deposited energy greater than a fixed value. The central part of the program is the routine *readevents*, it starts by analysing the signal in the tagger (subroutine *anapm_tag*) searching the coincidence between one of the short plastic scintillator (1-8) and the logical "AND" between the two long ones (0,9). If this coincidence exists, the program checks that it is time with the nuclear event in the target then rebuilds the information about the time of flight start signal. The subroutine *anastrip_tag*, calculates for each signal in the microstrip, the emitted photon energy using equation 2.2, and associates signals in adjacent strips into cluster.

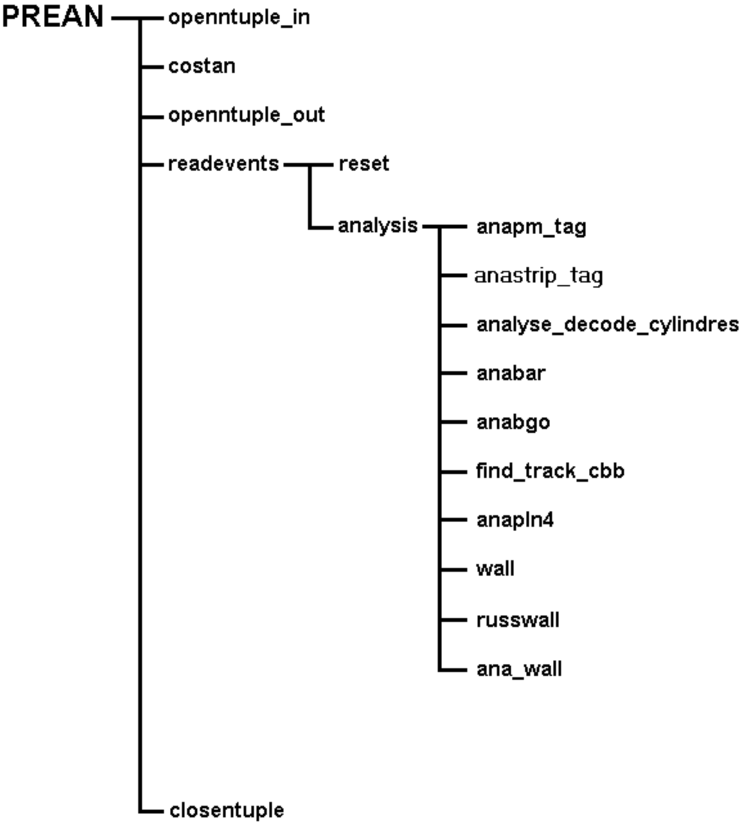

Figure 3.5: The Prean routine scheme.

3.4.1 Events reconstruction in the central detectors

Prean analyses the Lagranγe detectors signals starting from the barrel response. The subroutine *anabar* reads the detector calibration constants and converts ADC and TDC spectra into energy deposited and time of flight. It also makes a check to control if the ADC signal is above to the noise discrimination threshold and if the TDC is in coincidence with the tagging signal an then with a backscattered $\overrightarrow{\gamma}$. An index (*ind_bar*; tab:3.2) which characterises the information is associated to each signal in the barrel.

The program analyses the BGO calorimeter signals. It looks for the crystal that gave a signal greater then the software threshold (written in *data.base*) and de-

ind_bar	**ADC**	**TDC**
0	Energy value is over the noise/signal threshold imposed for the discrimination.	Barrel time signal in coincidence with the tagger signal.
-1	Energy value is over the threshold imposed for the discrimination noise/signal.	The signal is not in time with the tagger detector.
-5	Under threshold. It cannot be distinguished from the noise.	Barrel time signal in coincidence with the tagger signal.
-6	Under threshold.	Not in time.

Table 3.2: The index *ind_bar* which represents the information about the ADC and TDC signal in the scintillator barrel.

fines this crystal as ”active”; then it converts the ADC channels into the respective energy values (measured in GeV). Active crystal energies are saved in the matrix *adepth(it,ip)* which identifies the crystal by two indexes *it* and *ip* associated respectively to the angle ϑ and φ. When a particle hits a crystal, it generates an electromagnetic shower that involves a set of BGO crystals. It is necessary to select inside the map *adepth* a group of crystals (called *cluster*) that were activated by the shower of one particle. Two strategies were developed to solve this problem [59]. The first is called *contiguity method*, and it work in this way: starting from the lowest *(it,ip)* in the *adepth* matrix an algorithm checks if any of the adjacent crystals is in the list of the active crystals. If yes the neighbours ere associated to cluster number 1 and the scan proceeds with further neighbours until a pattern of contiguous crystals can be followed. Then the first crystal in the list, that is not attributed to the cluster 1, is taken as the seed of cluster number 2 and the procedure of associating neighbours and further neighbours cells is repeated until contiguity can be maintained. When all active crystals are associated to a cluster the procedure stops. This is the simplest and faster of clustering methods, but cannot avoid energy spills, satellite cluster and merging showers.

The second method (called *cellular automata method* is an algorithm based on transition rules equivalent to those of Breton [60]. The *m* active crystals are ordered in a list by descending value of the energy deposited inside the crystal E_{cry}. This means that the first crystal in the list is the absolute maximum as regards energy. The procedure then, finds the relative maxima, i.e the crystals that have detected an energy higher than any of the adjacent cell and marks them progressively $1, 2..., j, ...n$. This means that, since the list is written and examined in descending order, the absolute maximum will be the seed of cluster number 1, the second highest relative maximum will be the seed of the cluster number 2 an so on. A this point we have *n* cluster containing a single crystal and the energy of the cluster E_{cl} will be energy deposited inside the crystal E_{cry}. In the following steps each established cluster j is examined in descending E_{cl} order. When a crystal, that is not yet assigned to a cluster, is neighbour to more crystal already assigned to different cluster, it will be attributed to the cluster that have the highest E_{cl} and its E_{cry} is added to E_{cl} of that cluster. The procedure is iterated until there are no more neighbours to any of the n cluster to infect. At any step the list of cluster is re-ordered and examined by descending E_{cl} so that the cluster with higher cumulative energy has priority in infecting new adjacent cells. The main advantage of this procedure whit respect to the *contiguity method*, is the ability of separating merging shower that deposit energy in a set of contiguous crystals but with distinguishable maxima.

When the cluster identification is done, for each of this are calculated:

- the number of crystals that form the cluster (*multiplicity*);
- the cluster energy as a sum of the single crystals energies;
- ϑ and φ angles estimated as a weigh average of the single ϑ_i e φ_i of the crystals centres. The weight is the ratio between energy deposited inside the $i-th$ crystal and its volume.

Subsequently the cluster energy is correct to taking in saccount the effects of:

1. threshold imposed on the crystals;
2. errors due to the cluster reconstruction method;
3. electromagnetic shower losses in the external calorimeter crown.

For each BGO clusters a confidence index, *ind_bgo*, is defined. It is initially set at 0 and then it is switched to -3 if there are more then 30 clusters in the calorimeter or if there are more then 50 crystals in a single cluster or if the energy cluster is greater than 2 Gev.

Signals released in the cylindrical wire chambers are analysed by the subroutine *analyse_decode_cylindres*. At first, the analysis consists in the identification of all tungsten wires and all copper strips that released a signal. Then the analysis continues with the study of hits in each chamber separately.

For each chamber, in fact, the association of hits in internal cathode with hits in anode is performed. Each association identifies one point in the space and his position relative to the centre of the target. The same procedure is used for the association of hits in the external cathode with hits in anode.

When all spatial information have been extracted for each point, the analysis consists in trying to associate points obtained from anode-internal cathode association with points obtained from anode-external cathode association. The association happens for the two points less spacing and the procedure continues for remaining points. When spacing is greater then 0.35cm, no association is performed.

This procedure is realised for each chamber distinctly.

In this way we have identified the points (and their coordinates: (x_int, y_int, z_int) (x_ext, y_ext, z_ext)) in which charged particles cross the detector.

The last step of the analysis of signals in cylindrical wire chambers is the association between points identified for the internal chamber with points identified for the external one. To do this, a comparison between polar coordinates is performed. So the last association consists in the choice of two points for which the difference $|phi_ext - phi_int|$ is the less one and the procedure continues for remaining points. When the polar difference is greater then 8°, no association is performed.

If the last association has been performed, we know two points in the space of each charged particle trajectory. So we can describe the exact trajectory of each charged particle using the coordinates $(x_int; y_int; z_int)$ and $(x_ext; y_ext; z_ext)$.

Closed the information reconstruction, Prean begins a classification of the events looking for an association among the signal in the three central detectors.

The standard criteria is based on comparison between the azimuthal and polar angles of the signals. For each event in the cylindrical chamber, the program makes a control of the BGO clusters angles; if the two differences $\vartheta_{BGO} - \vartheta_{cyl}\text{and}\varphi_{BGO} - \varphi$ "fall" near 0 with a fixed error, the signals from the two detectors are associated (MWPC-BGO signal) with the passage of the same charged particle. Then the program checks the signals in the barrel, comparing in the same way the φ angles for a possible association with the MWPC-BGO signal.

When the association MWPC-BGO fails, the program analyses the scintillator barrel signals for a possible correlation MWPC-BARREL. In this case the event is associated with the passage of a charged particles that does not arrive in the calorimeter. This charged particle is called *lost particle* and we only know the angular coordinates of their tracks.

For all the BGO cluster that are not correlated with a MWPC signal, the program searches a BGO-BARREL association and eventually defines the signal as a charged particles with a MWPC inefficiency. If it is impossible to associate a BGO cluster with the other central detectors, the cluster is tagged as a neutral particle signal (photon or neutron).

It is important to stress that the program associates all detectors signals also if they are below threshold or out of time. All the information about the signal forming the track are saved in a index called *itipo_track*

3.4.2 Events reconstruction in the forward direction

The last step of Prean is the analysis of the Lagranγe forward detectors. The subroutine *anapl4* studies the signals and traces the charged particles that activated the four planes of the planar wire chambers. The UV-XY association defines a track which is identified by the *cltot* index reported in table 3.3.

The subroutine *wall* evaluates the energy lost inside the hodoscope wall bars by a charged particle and the time signal of the two layers. In the data analysis the cases in which the particle hits both layer or only the first one are considered. In the first case, the two activated bars (one horizontal and one vertical) give the x and y coordinates. In the second one the hit bar provides the y coordinates while

cltot	**Meaning**
0	All the hits in the four planes are associated in a track.
-1	A hit is missing in one of the four planes, but the track is rebuilding using the three avaible hits.
1,2, 3	There is one extra-hits in 1,2 or 3 planes.
9	More than 3 extra-hits.
10	No track is reconstructed because there are too many activated wires

Table 3.3: The index *cltot* and its meanings.

the x coordinate is calculated from difference between the scintillation light time of flight for the photomultipliers on each side of the bar:

$$x = \frac{1}{2} v \cdot |tof_1 - tof_2| \tag{3.4}$$

v= light velocity inside the scintillator.
tof_1, tof_2= the times of flight measured by the two photomultipliers.

The energy deposited in the bars (obtained from the conversion of the ADC channel using the calibration constants) must be corrected for the light attenuation on the distance l between the impact point and the photomultiplier; from the 3.3 we can write:

$$E^{dep} = \frac{ADC}{a} \cdot e^{\beta \frac{l}{L}} \tag{3.5}$$

After the reconstruction of the signals in each detector we search for the geometrical association between MWPC's signals and the hodoscope wall signals. To do this, we have defined in PREAN the coordinates x_{pc-hw} and y_{pc-hw} of the trajectory projection on the hodoscope wall of the event detected by the chambers with coordinates $(x_{pc}; y_{pc})$. If $(x_{hw}; y_{hw})$ are the coordinates detected by the wall, we can construct the follow variables:

$$\Delta x = \frac{|x_{pc-hw} - x_{hw}|}{11.54} \tag{3.6}$$

$$\Delta y = \frac{|y_{pc-hw} - y_{hw}|}{11.54} \tag{3.7}$$

where 11.54 is the width (in *cm*) of the wall bars. We consider all possible combinations of the signals on the planar chambers and the hodoscope wall and we choose the combination giving the smallest value of the quantity:

$$\Delta C = \sqrt{\Delta x^2 + \Delta y^2} \tag{3.8}$$

and which satisfies the condition

$$\Delta C < 1.5 \tag{3.9}$$

The upper limit 1.5 was chosen after on the base of simulation study.

In the same way, Prean studies the shower wall signals and try to associate them with the other two detectors. The result of this work is saved in the index *iass_trf* shown in table 3.4.

At the end of the program Prean, an n-tuple *namefile.pol* is filled with all the track variables both for the central and the forward detectors (deposited energy, $x - y$ coordinates, angles, time of flight...) The output file, as all files of the software chain, can be analysed with the Paw package. These files represents the input for the programs written for analysis of a specific channel. For deuteron photodisintegration the program Medea, that is described later, was written.

PC	**OW**	**RW**	*iass_trf*	**Classification**
1	1	1	7	Charged particle.
1	1	0	6	Charged particle stopped in the hodoscope wall.
1	0	1	5	Charged particle with hodoscope wall inefficiency.
1	0	0	4	Noise in MWPC.
0	1	1	3	Charged particle with wire chambers inefficiency.
0	1	0	2	Noise in hodoscope wall.
0	0	1	1	Neutral particle.

Table 3.4: The result of tracks reconstruction in the forward detectors is saved in the index *iass_trf*.

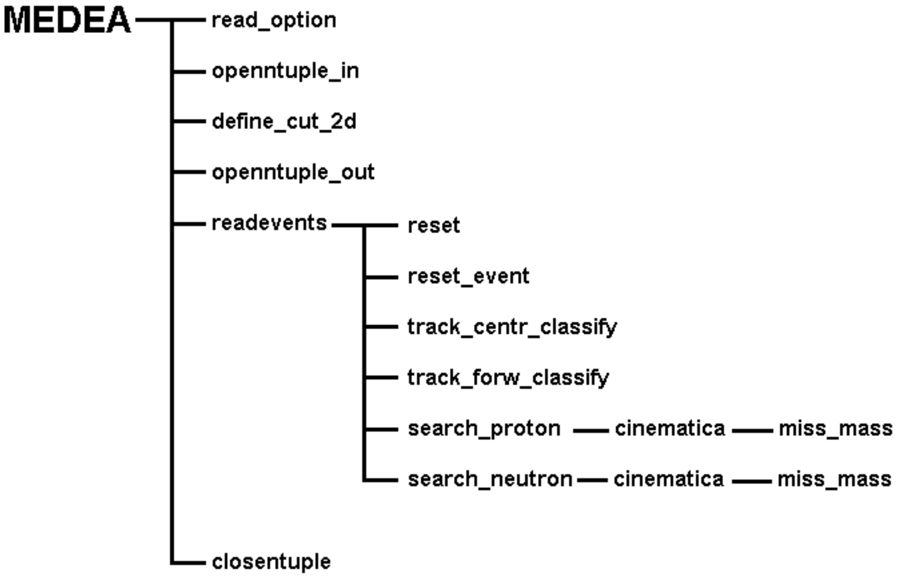

Figure 3.6: The MEDEA routine scheme.

3.5 MEDEA

MEDEA is a new software; it is articulated in several routines, as shown in figure 3.6, and it was written for the kinematical reconstruction of the photonuclear reactions (based on simulated o experimental data) that were pre-analysed with PREAN. The program makes also some preliminary event cuts for the deuteron photodisintegration event pre-selection.

Working strategy is simple: MEDEA starts with the initialisation of some memory blocks (*openntuple_in, opentuple_out*), then it reads the data from *Prean* output files (*readevents*). *Track_centr_classify* and *track_forw_classify* are the routines that we use to catalogue the detected particles of each event and to associate them with the physical variables such as particle energy and angles.

Starting from the central detectors signals, MEDEA identifies the particles scanning the information coming out from the BGO and the barrel. Comparing the specific energy loss (dE/dx) detected in the barrel, with the energy deposited in the calorimeter, it is possible to distinguish two different populations (picture 3.7). In fact charged particles loose energy following the Bethe-Bloch law:

$$-\frac{dE}{dx} = Kz^2\frac{Z}{A}\cdot\frac{1}{\beta^2}\left[\frac{1}{2}ln\frac{2m_ec^2\beta^2\gamma^2T_{max}}{I^2} - \beta^2 - \frac{\delta}{2}\right] \qquad (3.10)$$

where:
T_{max} = highest kinetic energy which the particle can transfer to an electron in a single collision;
Z = atomic number;
A = mass number;
I = average excitation energy;
δ = density correction constant.

In the figure 3.7) we can observe two trends: one, is characterised by a constant value of energy loss of about 2.05 MeV/cm, which is typical of the particles at the ionisation minimum (MIP) such as charged pions of 100 MeV kinetic energy. The other population show the typical $(1/\beta^2)$ slope and it is composed of non-relativistic protons.

In the region above 0.5 GeV, the two populations mix up because protons start to became relativistic. In this region it is hard to distinguish the two kinds of particles from this strategy of analysis.

The particles that produced a good signal in the barrel and in the BGO (independently if there is a signal in the MWPC's) are tagged from PREAN as charged particles. MEDEA, with the subroutine *define_cut_2d* and CUT_2D makes a cut on the two kinematical regions in order to select the largest number of protons with the smallest pions contamination. The cut is developed by simulations studies, and its result can be observed in picture 3.7. The result of the cut is saved in a index (*iclass_p*) that can be used in the event selection.

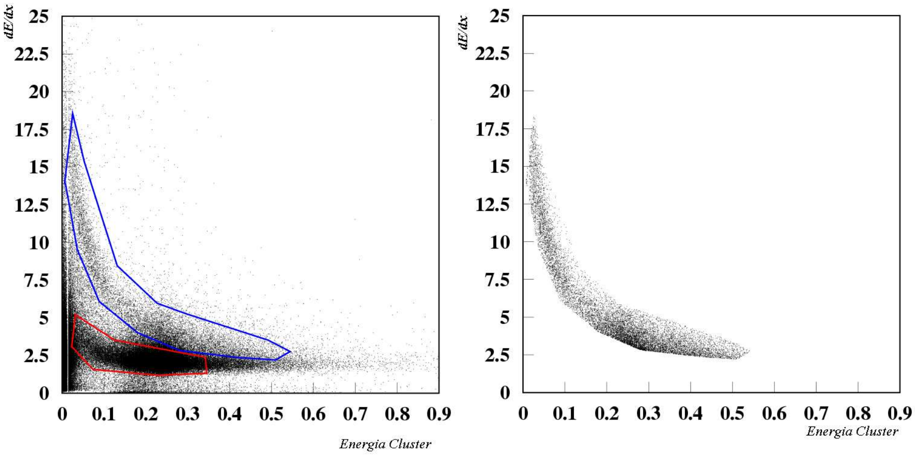

Figure 3.7: The figure shows the bidimensional plot of the energy deposited in the barrel (dE/dx) versus the energy deposited in the BGO cluster On the left, before the cut, we can see the different population; on the right we can see the result of the cut for the proton selection.

For the tracks that did not show a signal in the BGO (or have a signal under threshold) but only in the MWPC's and in the barrel, the graphical method described before cannot be used. These events are probably correlated with the passage of slow (and heavy) charged particles.

Medea analyses all the possible combinations of a signals in the MWPC's and in the BGO, that do not have a good response in the scintillator barrel and the tracks with a signal in the MWCP's only. The last case represents the events that show a signal in the BGO calorimeter only. We stress that it is not possible to discriminate photons from neutrons in the calorimeter, a preselection criterion for neutrons is the condition that the cluster has low multiplicity[1] When a neutron crosses the calorimeter, it produces a cluster which contains no more than 4-5 crystals. Unfortunately low energy photons can also produce low multiplicity cluster.

For charged particles detected in the forward region ($\vartheta < 25°$), Medea combines the two information of time of flight and the energy loss in the hodoscope wall. Picture 3.8 shows the behaviour of the energy deposited in a bar by a charged particle in function of its TOF. Since the TOF$\sim 1/\beta$, we can distinguish 4 different regions:

- a first region in which the energy loss grows up with the second power of the time of flight. It is the characteristic behaviour of Bethe-Bloch function for non-relativistic particles ($\beta << 1$). This region is associated with the passage of protons with a kinetic energy less than their mass (938 MeV);
- in the second region, the deposited energy is inversely proportional to the square value of TOF, and directly proportional to the particle kinetic energy. This is the case of a charged particle that stops in the detector.

---

[1] Number of crystals in the cluster

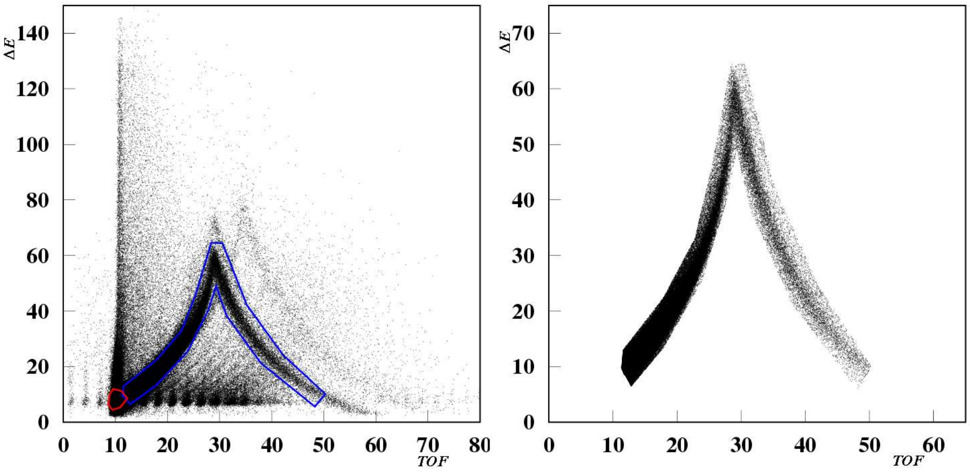

Figure 3.8: The bidimensional plot for the deposited energy in the hodoscope wall (ΔE) versus the time of flight (TOF) before the cut for the proton selection (left) and after the cut(right).

- The third region is characterised by a constant energy released in the detector. They are MIP particles lighter than the proton, i.e. pion.

- The last region shows a time of flight less than 11 *ns* are ultra-relativistic particles ($\beta \approx 1$).

In picture 3.8 is emphasised the graphical cut that the program uses for the identification of the charged particle track. As for the central tracks a label in which is registered the result of the cut is created. .

The last step of the identification consist in analysing forward neutral signals. A study of the time of flight allows to discriminate (figure 3.9) photons from neutrons. The photons, move at light velocity and have fixed TOF values ($\Delta t = L/c \sim 11$ *ns*), and can easily be distinguished from the neutrons that are slower and cover a continuous time of flight spectrum.

All the other central or forward detectors track that not are described before are labelled like ”*noise*”.

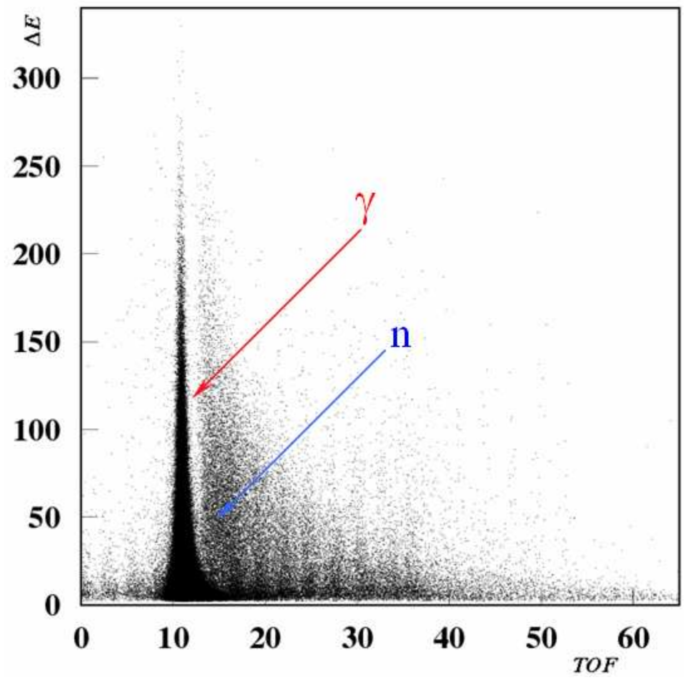

Figure 3.9: The bidimensional plot for the deposited energy in the shower wall (ΔE) versus the time of flight (TOF) for the neutral track ($iass\_trf$=1). It is clear the difference between the TOF spectrum of the photons that is a peaked distribution around 11 ns and the neutron TOF spectrum that is continuous and grater than 15 ns.

3.5.1 The routine "*search_proton*"

At this point, we have a set of labelled tracks for each event. Therefore the program makes some preliminary cuts on the total number of particles (tab: 3.5) and calls the routine *search_proton*. For each event, the routine makes a loop on the total number of charged tracks and creates a vector in which all the particle physical variables such as angles, TOF, dE/dx, and energy deposited in the calorimeter are arranged for each track . From the measured variables the subroutine calculates the total energy (in the hypothesis that the particle is a proton) using the formula:

$$E_p = T_p + m_p + \frac{dE/dx}{2\sin\vartheta_p} \tag{3.11}$$

where:
T_p is the energy deposited in the calorimeter;
m_p is the proton mass;
dE/dx is the energy deposited in the scintillator barrel;
ϑ_p is measured proton angle.
And for the forward protons:

$$E_p = m_p \cdot \gamma \tag{3.12}$$

with: β defined by equation 2.40 in which $D = 301.53\,cm$ is the distance from the target centre to the hitted point on the hodoscope wall.

From the total energy, the program calculates the spatial momentum modulus $p_p = |\overrightarrow{p_p}|$ and its components:

$$\begin{aligned} p_p &= \sqrt{E_p^2 - m_p^2} && (3.13)\\ p_{px} &= p_p \sin\vartheta_p \cos\varphi_p && (3.14)\\ p_{py} &= p_p \sin\vartheta_p \sin\varphi_p && (3.15)\\ p_{pz} &= p_p \cos\vartheta_p && (3.16) \end{aligned}$$

We evaluate some variables important for the data analysis. Deuteron photodisintegration is a two body reaction (one photon and one nucleus in the initial state, one proton and one neutron in the final state) so that, from the initial quadri-momenta $\widetilde{p_\gamma} = (0, 0, E_\gamma, E_\gamma)$, $\widetilde{p_D} = (0, 0, 0, m_D)$ and from the proton quadri-momenta $\widetilde{p_p} = (\overrightarrow{p_p}, E_p)$ of the final state, it is possible to determine the physical variables of the particles that fulfils the conditions imposed by a two body reaction. These variable are:

- ✓ Missing particle mass;
- ✓ Missing particle angles;
- ✓ Missing particle energy.

MEDEA uses the subroutine *cinematica* and called by *search_proton*. Two methods are developed in this subroutine: the first uses (in addition to E_γ) three final state measured variables, E_p, ϑ_p and ϑ_p and calculates:

1. Missing energy by energy conservation law:

$$E_{miss} = E_\gamma + m_D - E_p \tag{3.17}$$

2. missing particle momentum components:

$$\begin{aligned} p_{x\_miss} &= -p_{px} && (3.18) \\ p_{y\_miss} &= -p_{py} && (3.19) \\ p_{z\_miss} &= E_\gamma - p_{pz} && (3.20) \end{aligned}$$

   and its modulus:

$$p_{miss} = \sqrt{p^2_{x\_miss} + p^2_{z\_miss} + p^2_{z\_miss}} \tag{3.21}$$

3. the angles ϑ_{miss}, φ_{miss} from the formulas:

$$\begin{aligned} \vartheta_{miss} &= \arctan \frac{\sqrt{p^2_{x\_miss} + p^2_{y\_miss}}}{p_{z\_miss}} && (3.22) \\ \varphi_{miss} &= \arctan \frac{p_{y\_miss}}{p_{x\_miss}} && (3.23) \end{aligned}$$

4. The missing particle mass:

$$m_{miss} = \sqrt{E^2_{miss} - p^2_{miss}} \tag{3.24}$$

Since the charged particle may not be a proton or may not come from a disintegration, the quantity under square root in 3.24 may be negative. For these reasons we will select only the events for which $E^2 - p^2$ is positive

The second method for the computation of the missing particle variables uses only the measured angle ϑ_p. Starting from the Lorentz transformations:

$$E_p = \gamma\left(E^*_p - \beta \cdot p^*_p \cos\vartheta^*_p\right) \tag{3.25}$$

$$p_p \cos\vartheta_p = \gamma\left(p^*_p \cos\vartheta^*_p - \beta \cdot E^*_p\right) \tag{3.26}$$

that describe the laboratory frame variables (p_p, E_p) as a function of the same variables in the centre of the mass system ($p^*_p, \vartheta^*_p, E^*_p$). E^*_p is unambiguously determined when the energy of the incoming photon is fixed, by the equation [61]:

$$E_p^* = \frac{s - (m_p^2 - m_n^2)}{s\sqrt{s}} \tag{3.27}$$

with the relativistic invariant:

$$s = m_D^2 + 2E_\gamma m_D \tag{3.28}$$

that represents the square of the CMS total energy.
Inverting the equations 3.25 and 3.26 to obtain $p_p^* \cos\vartheta_p^*$, we have:

$$\gamma p_p^* \cos\vartheta_p^* = \frac{1}{\beta}\left(\gamma E_p^* - E_p\right) \tag{3.29}$$

$$\gamma p_p^* \cos\vartheta_p^* = p_p \cos\vartheta + \gamma\beta E_p^* \tag{3.30}$$

comparing the two expressions we obtain:

$$\frac{1}{\beta}\left(\gamma E_p^* - \sqrt{p_p^2 + m_p^2}\right) = p_p \cos\vartheta_p + \gamma\beta \cdot E_p^* \tag{3.31}$$

where the substitution $E_p = \sqrt{p_p^2 + m_p^2}$ was done.
Isolating the square root:

$$\sqrt{p_p^2 + m_p^2} = \gamma E_p^* \left(1 - \beta^2\right) - \beta p_p \cos\vartheta_p \tag{3.32}$$

then calculating the square value of both sides:

$$\left(1 - \beta^2 \cos^2\vartheta\right) p_p^2 - \frac{2\beta}{\gamma} E_p^* p_p \cos\vartheta - \left(\frac{E_p^*}{\gamma}\right)^2 + m_p^2 = 0 \tag{3.33}$$

For a fixed ϑ_p, this is a second degree equation in the variable p_p, and we can solve it:

$$p_p(\vartheta) = \frac{-b(\vartheta) \pm \sqrt{b^2(\vartheta) - 4a(\vartheta) \cdot c}}{2a(\vartheta)} \tag{3.34}$$

where:

$$\begin{cases} a(\vartheta) = (1 - \beta^2 \cos^2\vartheta) \\ b(\vartheta) = \frac{2\beta}{\gamma} E_p^* \cos\vartheta \\ c = m_p^2 - \left(\frac{E_p^*}{\gamma}\right)^2 \end{cases}$$

Equation 3.33 allows only one positive solution and the program automatically choose this solution and from the value of $p_p(\vartheta)$, using formula 3.13-3.24, calculates all the other variables (E_p, ϑ_{miss}, etc...).

As we will see later (4.2) the two most important backgrounds in deuteron photodisintegration analysis are the π^+ and π^0 photoproduction on the proton with a spectator neutron ($\gamma + p(n) \rightarrow \pi^+ + n(n)$; $\gamma + p(n) \rightarrow \pi^0 + p(n)$). In order to study these backgrounds, we recalculate in MEDEA the missing variables in the hypothesis that the detected charged particles are produced in these two reactions. All the variables are saved in specific memory blocks.

3.5.2 Neutron searching

The last subroutine of MEDEA is "*search_neutron*". It works like "*search_proton*", making a loop on the detected neutral tracks of each event. In the routine, we order in a vector of tracks the forward neutron track followed by the central neutral ones. For the first kind of track we estimates the energy (E_n) using equation 2.40, while for the central ones it is not possible to use energy deposited in BGO because it is only an unknown fraction of the total neutron energy. In any case the program saves the BGO energy information. For all neutral tracks, the program (as for the charged ones) calls the subroutine *cinematica* for the computation of missing particle variables in the two cases: a neutron from deuteron photodisintegration, a neutron from π^+ quasi-free photoproduction on the proton.

The neutron detection efficiency of the LAGRANγE apparatus is low ($\sim 20 \div 30\%$), for that reason if no neutral tracks are detected, the program saves the event anyway to maintain the statistic as large as possible.

At the end of the iteration on the events the output file (*namefile.med*) is filled with all particles significant variables and then it is closed (*closentuple*. The n-tuple produced is ready to be analysed with PAW and processed by final selection program. We underline that MEDEA makes only a preliminary cuts (table: 3.5) and it classifies the tracks detected in the apparatus, computing all the physical variables allowed.

Cut	**Description**
ngood_charged = 1	The total number of "good" charged tracks
ntot_charged ≤ 5	The total number of charged tracks
nforw_neutron ≤1	The total number of forward neutrons tracks (TOF ≥ 11 *ns*)
ncentr_neutral ≤ 4	The total number of neutrals track (only signal in BGO)

Table 3.5: The (very) preliminary cut made by MEDEA on the events.

Chapter 4

$\gamma, D \rightarrow p, n$ reaction analysis

4.1 Introduction

This chapter is dedicated to the description of the analysis for the unambiguous selection of deuteron photodisintegration reaction events in the GRAAL data. The analysis strategy was developed studying the Medea preselected events and it leads to three methods whose results may be compared.

4.2 Simulation results

In order to understand how to extract deuteron photodisintegration events with the smallest background contamination, two simulation files were generated using Laggen. They contain respectively 700000 events with all channels allowed by the event generator and 1000000 simulated photodisintegration events. Simulation files pass through the whole software chain (Lagdig, Prean and Medea), and the final output is analysed using the package Paw. The study of the simulated data allows to check on the reconstruction obtained in the analysis software, and to evaluate the selection efficiency.

4.2.1 High energy protons

In photoproduction reactions, most of the energy in the centre of mass is used for meson creation or nucleon excitation. In the deuteron photodisintegration on the contrary, all the energy is shared between the proton and neutron; for this reason one of the two nucleons may have high energy. We already said that for the neutron in the forward direction the time of flight allows for the calculation of its energy, while in the central region the BGO information is not useful. On the other side, a high energy proton emitted with an angle $\vartheta_p > 25°$ and detected by the BGO calorimeter, does not release all its kinetic energy in the detector, but passes through the crystals and escapes from the back side of the detector. For this reason the energy measured by the calorimeter is only a fraction of the total proton energy.

This effect (due to the finite crystal dimension) clearly emerges when we make a comparison between the energy measured in the calorimeter (E_{meas}) and the proton energy calculated from its measured angle (E_{calc})(see sec:3.5.1). In picture 4.1 we can observe that a proton with kinetic energy greater than 0.5 GeV escapes from the BGO calorimeter. For this kind of particles, the detected energy is an incomplete information, then all missing variables calculated with the first method (like missing particle mass) cannot be used. The "escaping protons problem" also implies that the graphical cut based on the comparison between E_{clus} and dE/dx (sec:3.5; fig:3.7) does not work for high energy protons; for this reason we decided not to use it.

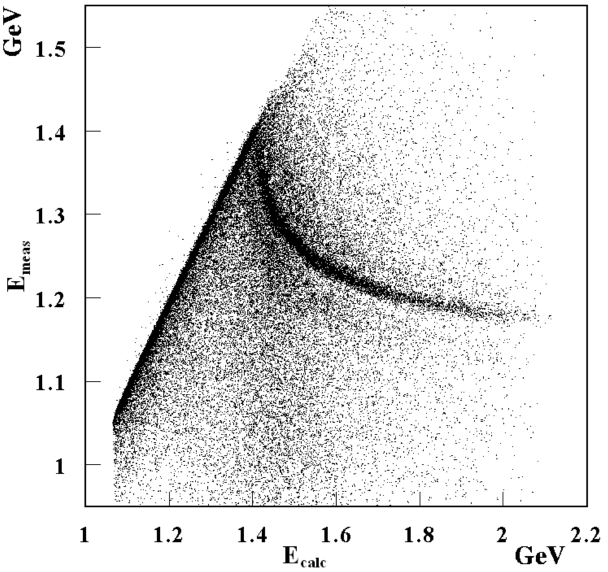

Figure 4.1: The energy measured in the BGO calorimeter (E_{meas}) versus the energy of the particle (E_{calc}) calculated from its polar angle in the hypothesis that it is a proton. 1.4 GeV total energy protons do not stop in the BGO calorimeter, and release in the crystal an energy fraction governed by the Bethe-Block formula (3.10). The figure shows that the relation betwen the measured and the calculated variable is linear until $E_p = 1.4\ GeV$, then E_{meas} decreases as the inverse of the energy E_{calc}. We also see as the proton becomes a MIP around 1.8 GeV of total energy.

To solve this problem, a new graphical cut was developed comparing experimental and simulated data. Unfortunately deuteron photodisintegration statistics in the experimental data is too low and the typical trend of E_{meas} Vs E_{calc} is not visible (figure 4.2(a)). On the contrary charged pion distribution, clearly appear in the experimental and in the simulated data and they are comparable (pictures 4.2(b) 4.2(c)). In this way it is reasonably legitimate to use a graphical cut on the bidimensional plot E_{meas} versus E_{calc} developed on simulated results also for the experimental data. The result of the cut is shown in figure 4.2(d).

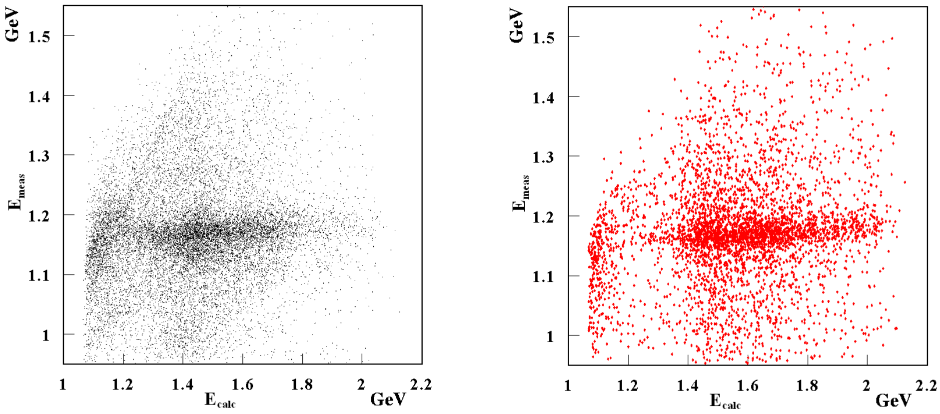

(a) Experimental data.

(b) simulated π^+ photoproduction data.

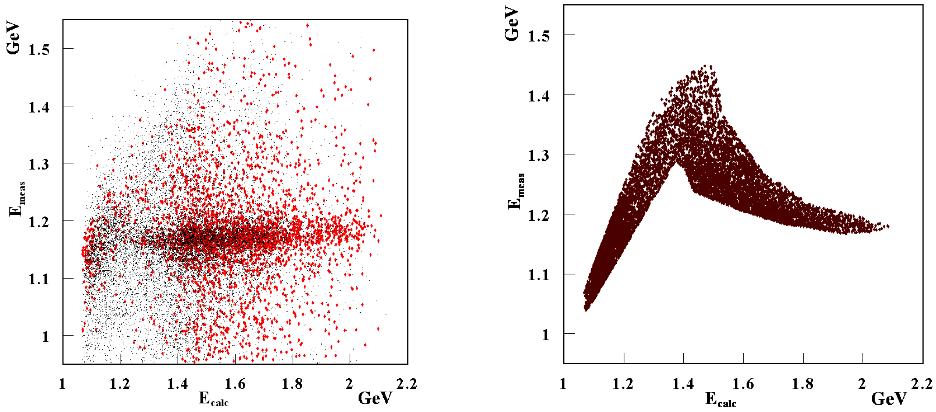

(c) comparison between experimental data (black marker) and simulated pion data (red marker).

(d) The results of the cut on the experimental data.

Figure 4.2: The figures show the distribution of the energy measured in the BGO (E_{meas}) versus the energy of the particle (E_{calc}) calculated from its polar angle in the "photodisintegration hypothesis". In the experimental data (a), proton distribution is not clearly visible due the low statistics of the deuteron photodisintegration reaction, but the charged pion distribution is evident. The simulation (b) points out that the π^+ is well simulated and the comparison with the data (c) ensure that the distribution is the same. We can define a cut on this bidimensional plot using the simulated data.

4.2.2 Background

Two reactions are the main background in the photodisintegration analysis. These are the charged and neutral pion photoproduction on the quasi free proton inside the deuteron:

1. $\gamma + p(n) \rightarrow \pi^0 + p(n) \rightarrow \gamma\gamma + p(n)$
2. $\gamma + p(n) \rightarrow \pi^+ + n(n)$

In the first reaction, one of the two photons from the π^0 decay may remain undetected, and the analysis of the event shows only a proton and neutral track. In the case when the photons are detected in the forward region the problem does not occur because they are easily discriminated from neutrons. When the neutral track is detected in the BGO calorimeter it is only possible to impose kinematical constrains to the neutral particle, like the coplanarity between the charged and the neutral track. The two final state particles, in facts, are emitted on the same plane ($\varphi_1 - \varphi_2 = 180°$) while in the π^0 production the proton is coplanar with the meson but not with the two decay photons. For this reason a cut on the coplanarity between the charged signal and the neutral one is also imposed. Analysis of the simulated data suggests a selection according to the relation:

$$\arccos[\cos(\varphi_p - \varphi_n - 180)] \leq 10° \tag{4.1}$$

where the arcocosine is necessary to consider also events differing of $-180°$.

Simulated events point out that the largest π^0 contamination occur when the proton is emitted in the forward direction. This kinematical region allows to use the proton energy information that is well determined by the TOF. Figure 4.4(b) shows the missing particle mass distribution for the forward proton calculated from the proton energy for photodisintegration and for π^0 production simulated data. A 1.1 GeV upper limit on the value of the missing mass is enough to suppress the neutral pion background contamination (figure 4.4(c)). The cut on the coplanarity, together with the cut on the missing mass and the following cuts:

1. number of photons in forward equal to zero, to verify absence of forward photon signal;
2. number of the neutral cluster in the BGO calorimeter less than 2, to exclude events with two neutral signal (the two π^0 decay photon);
3. neutral cluster multiplicity less equal than 4 to reduce the probability to mistake a photon with a neutron in BGO neutral cluster.

totally suppress the π^0 background.

The suppression of the charged pion background is not simple, because of two problems. The first one is that it is a coplanar reaction except for a smearing due

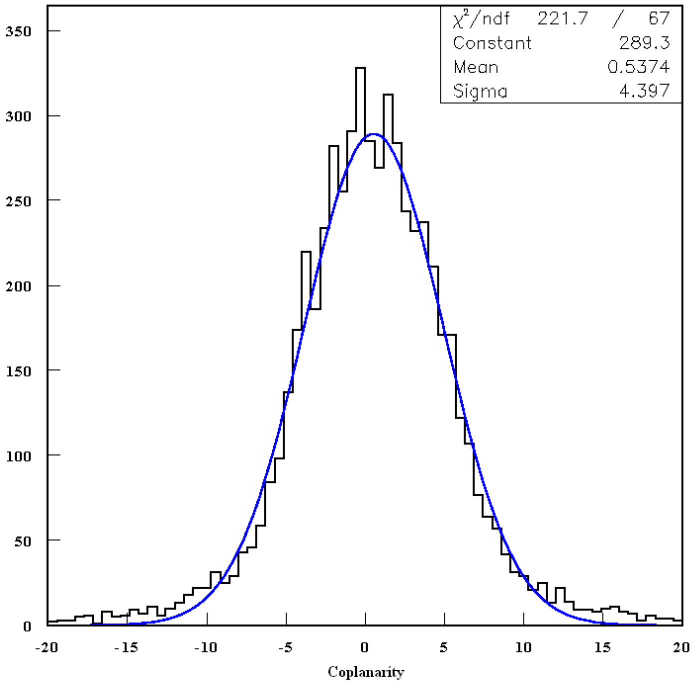

Figure 4.3: The distribution of the quantity $\varphi_p - \varphi_n - 180$ in a photodisintegration simulation. The fit suggest the upper limit 10° of the coplanarity between the proton and the neutron.

to the Fermi motion of the nucleons inside the deuteron. For this reason the cut 4.1 does not work well as for π^0 photoproduction. The second problem is that the missing particle of the charged pion is exactly the neutron. Charged pions, after loosing all their kinematic energy, decay into an electron and neutrino or are absorbed in BGO nuclei, generating a cluster in the calorimeter including more than five crystals. A cut on the charged cluster multiplicity reduces the π^+ background but it is not sufficient and we need to improve the strategy for the event selection.

4.2.3 (π^+, n) and (p, n) angular distribution

As told before, if we fix the initial conditions (E_γ and m_D) we can fully describe the final state for a two body reaction from the ϑ angle of one of the emitted particles (except for the azimuth orientation of the reaction plane). The LAGRANγE apparatus, with the MWPC detectors, allows to measure the angles of charged particles with high precision; on the contrary the proton and the pion energy are not well detected in BGO calorimeter. For these reasons we have developed a selection criteria based only on the angular information. To do this we studied the angle distribution of the charged particles ϑ_{ch} as a function of the neutron angle ϑ_n for the pion photoproduction on the proton and for the deuteron photodisintegration. Figure 4.6 shows theoretical curves for fixed incoming photon energy values. The difference of ϑ_{ch} Vs ϑ_n correlation for the two reactions is clear and a mixing up exist only when

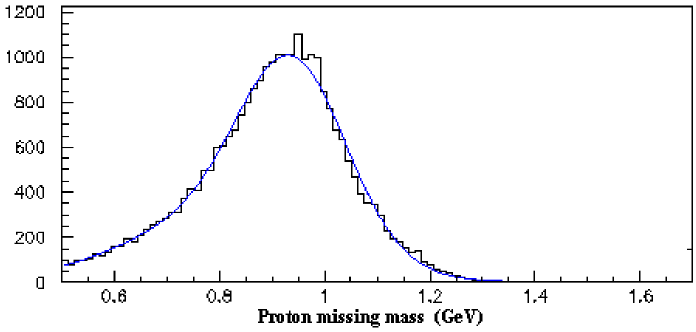

(a) Forward proton missing mass for the photodisintegration

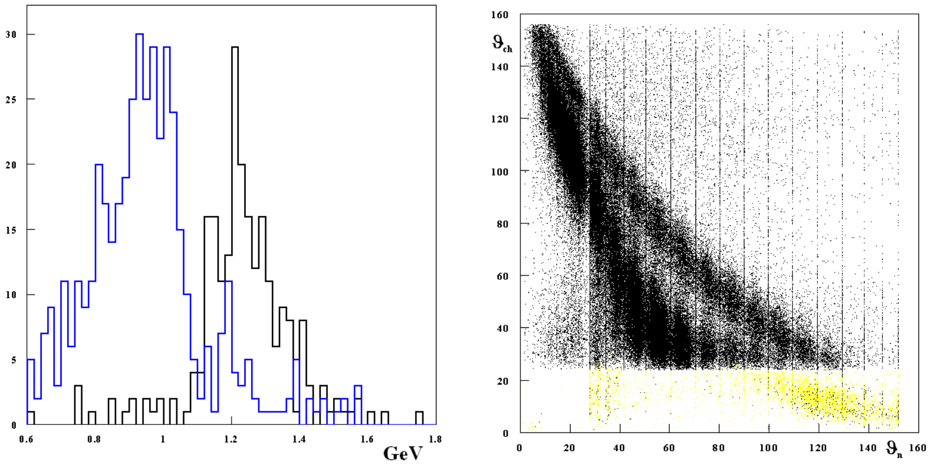

(b) Forward proton missing mass for the two reactions

(c) π^0 background suppression

Figure 4.4: In figure (a) the missing mass distribution for simulated photoreaction when the proton is emitted in the forward direction is reported. The distribution has the peak at 940 MeV (neutron mass $\sim$ 939 MeV). Figure (b) shows the comparison between the missing mass distribution for photodisintegration reaction (blue) and π^0 photoproduction (black). Figure (c) shows ϑ_{ch} versus ϑ_n (see next section 4.2.3) distribution for experimental data. The yellow points are the π^0 that are evidenced by the cut on the forward proton missing mass.

the neutron goes in the forward direction. In this kinematical region we can use the calculated missing variable from the neutron detection. The neutron energy, is well determined by the TOF then we can use the missing mass from the neutron to resolve the π^+ proton ambiguity. In figure 4.5(a) the missing mass from the neutron in the shower wall for simulated deuteron photodisintegration event and for simulated π^+ photoproduction are shown. A $1.1\ GeV$ upper limit on the missing mass from the neutron is imposed on the experimental data, and in figure 4.5(b) we can see how this cut well selects the proton from the charged pion.

Results of simulated data analysis are shown in figure 4.7, and they prove that events from the two reactions are distributed around their respective theoretical curves. The events distributions are well separated but the pions distribution are more spread due the Fermi motion of the proton target inside the deuteron nucleus. The experimental data (figure 4.8) show that the charged particles follow the same behaviour of the simulation and for this reasons we have decided to concentrate our analysis on the polar angle variables.

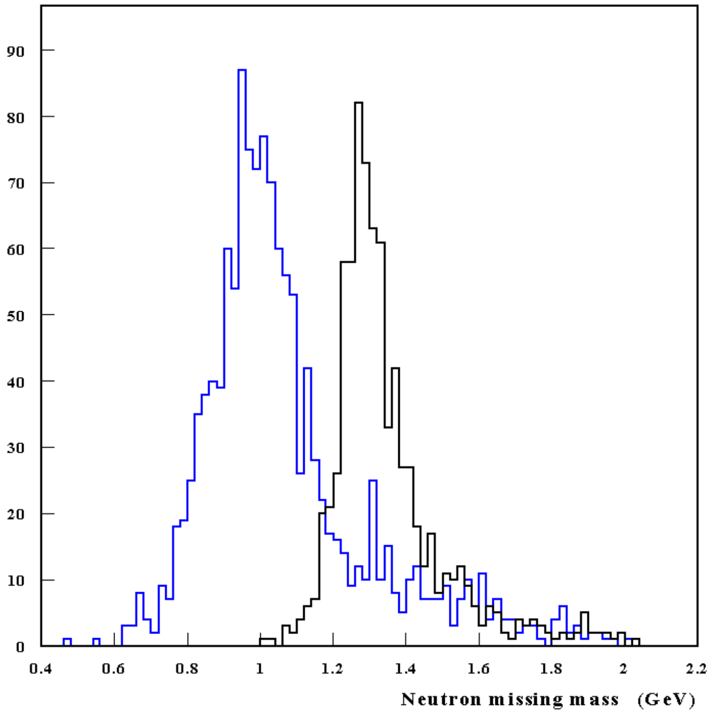

(a) Forward neutron missing mass

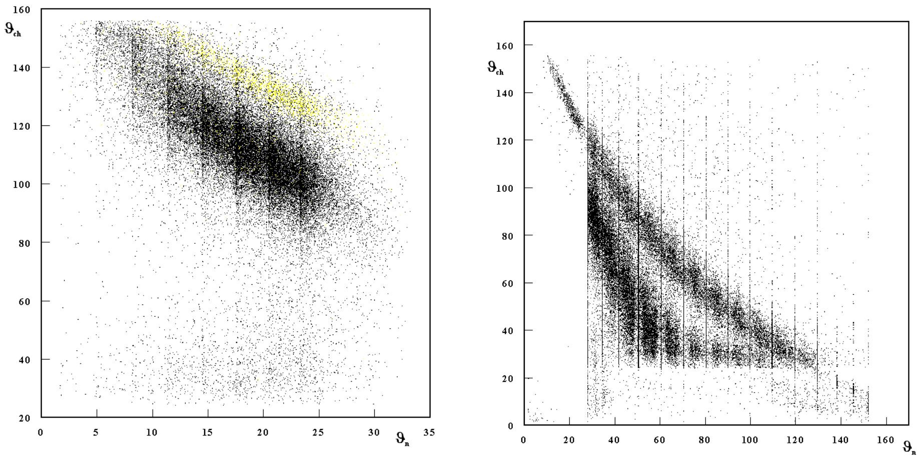

(b) ϑ_{ch} versus ϑ_n for the neutron in the forward region

(c) ϑ_{ch} versus ϑ_n

Figure 4.5: In figure (a) the missing mass distribution for simulated photoreaction events when the neutron is emitted in the forward direction are reported. The neutron energy is calculated from the TOF. The two distributions, corresponding to deuteron photodisintegration (blue) and π^+ photoproduction reaction (black), are well separated. Figure (b) shows the results of the cut; the yellow marker are events selected by the cut and they are protons. Figure (c) shows ϑ_{ch} versus ϑ_n distribution for experimental data with the application of the cuts for π^+ and π^0 background.

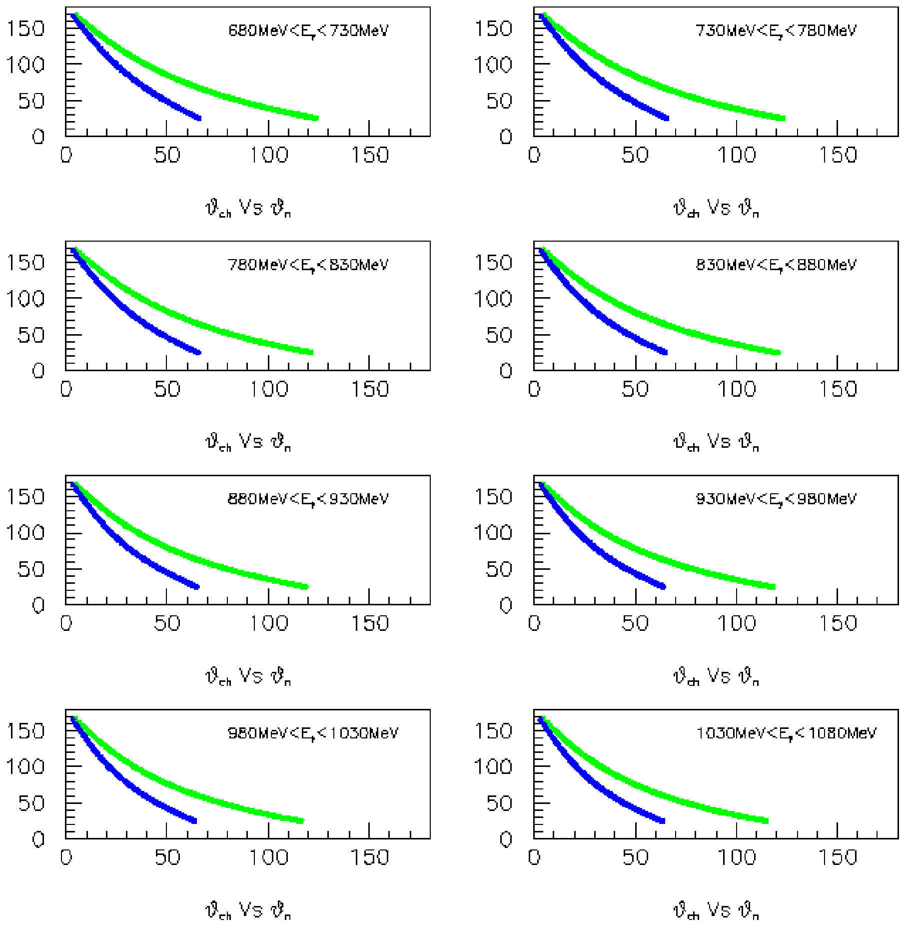

Figure 4.6: Theoretical curves of charged polar angle ϑ_{ch} versus neutron polar angle ϑ_n for the deuteron photodisintegration and for the π^+ photoproduction calculated for several energies of the incoming photon.

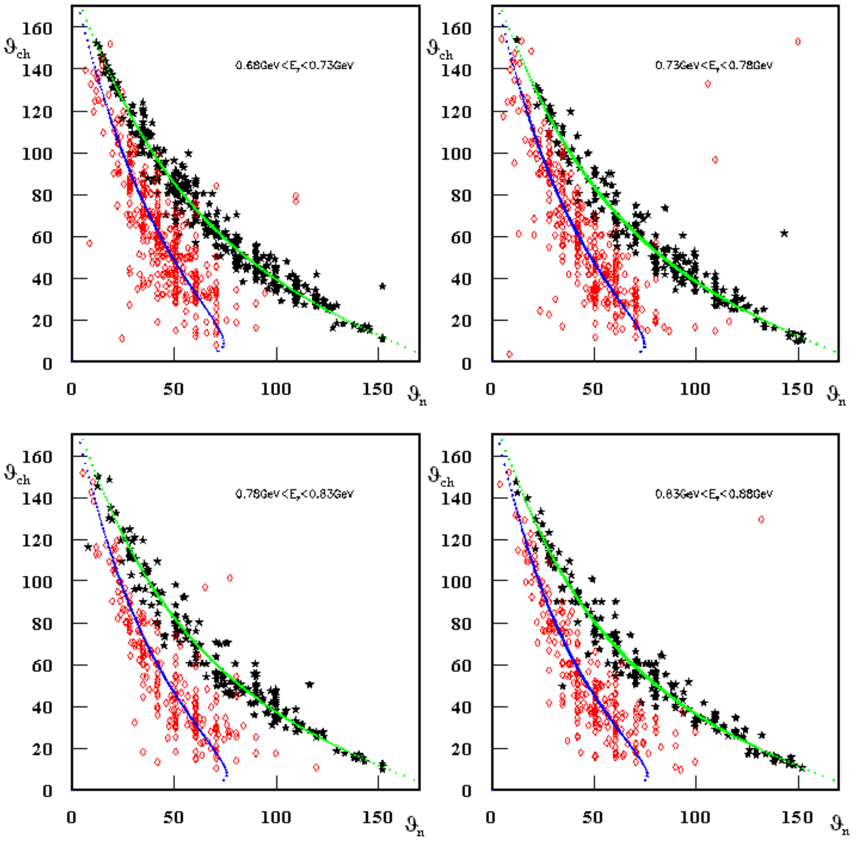

Figure 4.7: The figures show the ϑ_{ch} versus ϑ_n simulated data distribution for deuteron photodisintegration (black stars) and for π^+ production (red rhombs) with the superimposition of their respective theoretical curves.

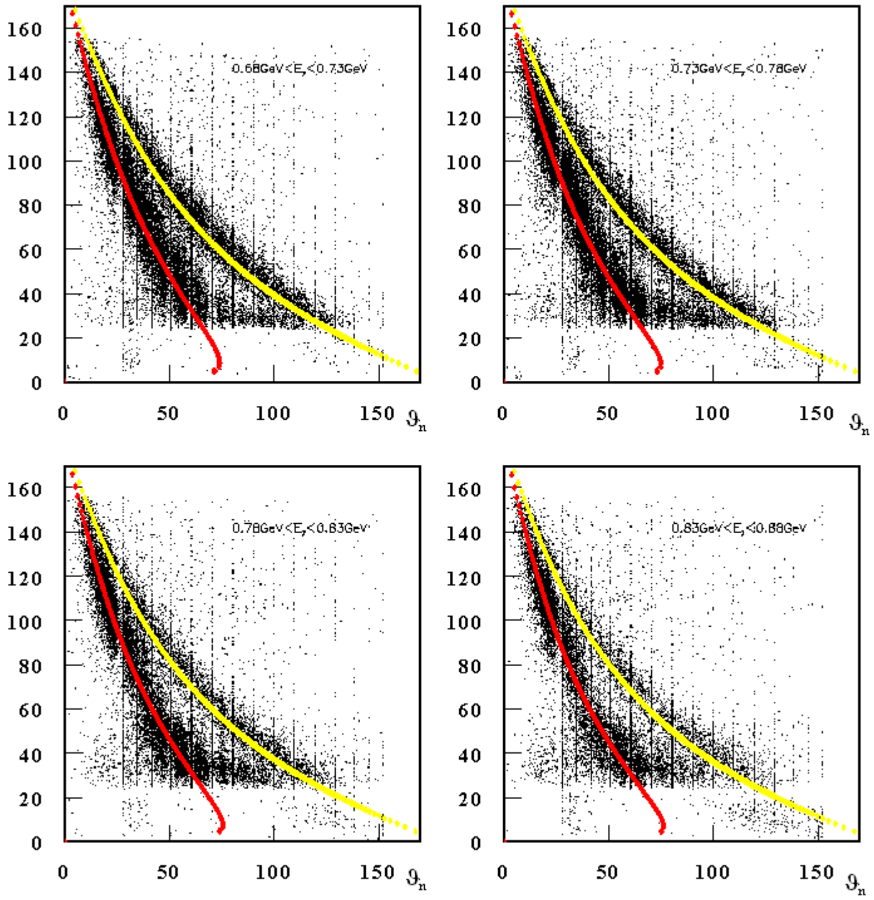

Figure 4.8: The figures show the ϑ_{ch} versus ϑ_n experimental data distribution with superimposition of their respective theoretical curves. The behaviour is the same than in the simulated data. The two different distribution (π^+ and proton) are clearly visible, the mix up in the neutron forward region is solved with a cut on the neutron missing mass (figure 4.2.2).

4.3 MERGE MEDEA and PHDIS

We developed the MERGE MEDEA code in order to impose the cuts on the coplanarity and on the missing mass from the neutron and the proton in the forward region as discussed before. With this program we also sum all the experimental data files (*run*) in a single output file (*nomefile.mmd*). The events in the final *n-tuple* are almost totally composed of deuteron photodisintegration and π^+ photoproduction. In facts, the cuts allow the reduction of the background due to the other reactions (such as π^0 photoproduction) in the selected events. From the simulations we have estimated that the contribution to the noise of this residual background is less than 1%, lower than the "natural" background of the apparatus ($\sim 2\%$), measured when the gamma-ray beam impinges on an empty target.

PHDIS is the last program of the GRAAL software chain. We use it for the calculation of the gamma photon flux in each energy bin. We will extract the beam asymmetry for some energy and proton polar angle in the centre of mass bin and for that we must know the number N^i_γ for each polarisation state that are in the *i-th* energy bin. Using the calibration file for the tagger detector, we know for each period of data taking at which energy each μ-strip corresponds. For each run, PHDIS reads the files in which are written the number of electrons that have activated the *j-th* strip ($j = 1, 128$). With the calibration file we can calculate its energy and at which energy bin the strip belongs, then the program increases the number N^i_γ for that bin. We also calculate the mean energy of the bin and the mean polarisation degree of the bin.

PHDIS code allows also to sum different MERGE MEDEA output files, in this way we can add new experimental data (from recent data taking) without reloading the entire set of data runs.

4.4 The events selection methods

To calculate the number $N_p(E_\gamma, \vartheta_p, \varphi_p)$ of the photodisintegration events for each photon energy, and proton polar and azimuthal angle and for each polarisation state ($p = H$ horizontal or $p = V$ vertical), we have studied an developed three analysis methods described in the following sections. We will compare the results of the three methods in order to understand the quality of the analysis.

4.4.1 The $\Delta\vartheta$ fit.

Starting from the request that one neutron is detected in the forward direction or one neutral cluster is detected in the BGO calorimeter, we have defined the quantity:

$$\Delta\vartheta = \vartheta_p^{miss} - \vartheta_n \tag{4.2}$$

where ϑ_p^{miss} is the missing particle angle in the hypothesis that the charged particle is a proton emitted in photodisintegration reaction. It is clear that for the photodisintegration events the variable defined in 4.2 should be distributed around 0°, while, for π^+ events $\Delta\vartheta > 10^\circ$. In figures 4.9, 4.10 and 4.11 we plot $\Delta\vartheta$ distribution for fixed photon energy, ϑ_p and φ_p bins[1], and two Gaussian distribution can be identified. A fit with a double Gaussian function allows to know the parameters of the two distributions (mean value and σ). The integration of the two Gaussian functions gives the number of the for the two reactions. This analysis strategy allows to subtract the π^+ background from the deuteron photodisintegration. We have selected events that presents only a charged signal in the central region because in the forward region the statistics is to low and it does not allow for a fit. For the same reasons (low statistic) this method works well only in the first three energy bin ($E_\gamma < 1.1\,GeV$)

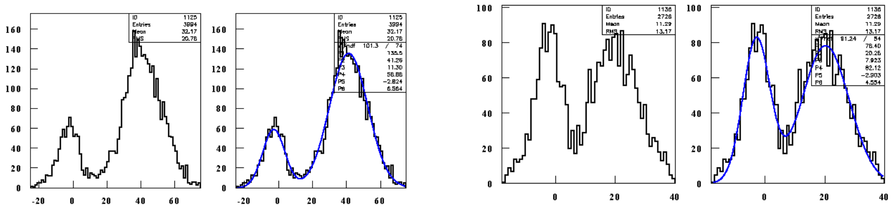

(a) $\vartheta^p_{cm} = 55^\circ$ (b) $\vartheta^p_{cm} = 90^\circ$

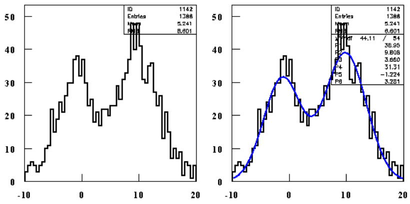

(c) $\vartheta^p_{cm} = 125^\circ$

Figure 4.9: The $\Delta\vartheta$ distribution in the first energy bin ($E_\gamma = 700\,MeV$) for the ϑ^p_{cm} bin in the central region

---

[1] To calculate the asymmetry we must know the number or deuteron photodisintegration events in each photon energy, ϑ_p and φ_p bins. Then we have to fit the $\Delta\vartheta$ distribution for each of these bins in which the statistic is sufficient. This imply 3x3x8=72 fits! We report here only some of this figures: for all the 3 photon energy beam and all the 3 ϑ_p bin, but only for the first φ_p bin.

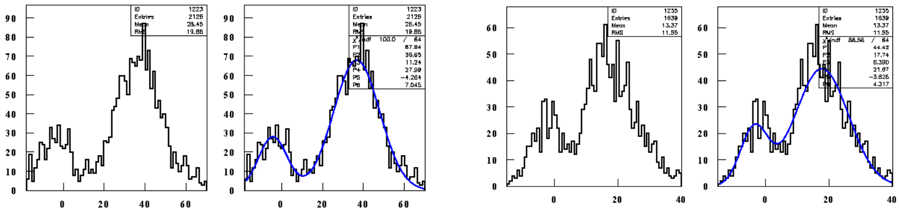

(a) $\vartheta^p_{cm} = 55°$ (b) $\vartheta^p_{cm} = 90°$

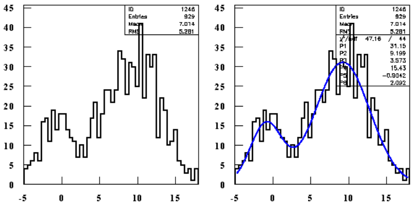

(c) $\vartheta^p_{cm} = 125°$

Figure 4.10: The $\Delta\vartheta$ distribution in the second energy bin ($E_\gamma = 900\,MeV$)for the ϑ^p_{cm} bin in the central region

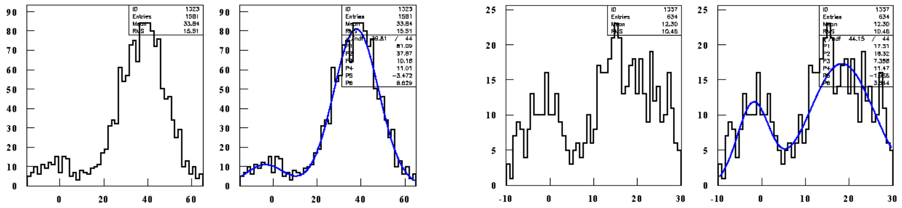

(a) $\vartheta^p_{cm} = 55°$ (b) $\vartheta^p_{cm} = 90°$

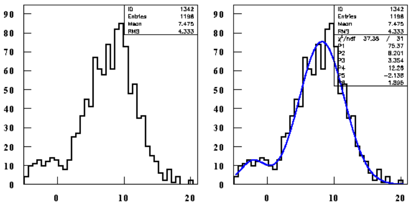

(c) $\vartheta^p_{cm} = 125°$

Figure 4.11: The $\Delta\vartheta$ distribution in the third energy bin ($E_\gamma = 1055\,MeV$)for the ϑ^p_{cm} bin in the central region

4.4.2 The $\Delta\vartheta$ cut

As we saw the π^+ photoproduction and the photodisintegration reactions are well separated in their ϑ_{ch} versus ϑ_n angular distribution (figure 4.6-4.8). Thanks to the preliminary cuts we can suppress most of the other background reactions. While the energy information from the TOF measured in the forward wall enables to discriminate the $\gamma p(n) \to \pi^0 p(n)$ and $\gamma p(n) \to \pi^+ n(n)$ reactions from the photodisintegration channel using the missing mass information from the nucleon detected in the forward region. Most of the residual background come from the $\gamma p(n) \to \pi^+ n(n)$ reaction when both charged and neutral final particle are detected in the BGO and in the central part of the detectors. We decided to select deuteron photodisintegration using a cut on the bidimensional plot ϑ_p versus ϑ_n. The cut was studied on the simulation data for each energy bin and the result is shown in figure 4.4.2, it selects a narrow distribution around $\Delta\vartheta = 0$. The number of selected events can be compared with the result of Gaussian integration to have an estimation of the its efficiency.

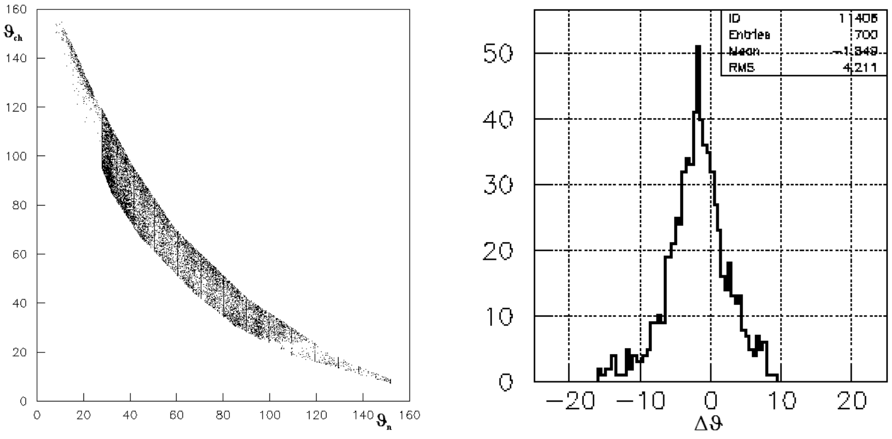

(a) Bidimensional graphical cut

(b) $\vartheta_{ch} - \vartheta_n$

Figure 4.12: Figure (a) shows the bidimensional graphical cut on the ϑ_{ch} versus ϑ_n distribution. Figure (b) shows how this cut works on the $\Delta\vartheta$ distribution.

4.4.3 $\Delta\vartheta_n, \Delta\vartheta$ product selection

Since we madethe request that one neutron is detected, we decided to investigate the possibility to use neutron polar angle information. For this reason we have studied the quantity:

$$\Delta\vartheta_n = \vartheta_n^{miss} - \vartheta_p \tag{4.3}$$

Simulations results shown that in the product of the two quantities $\Delta\vartheta_n$ and $\Delta\vartheta$ the pion photoproduction is distributed as a constant background that is very simple to fit and subtract. Moreover a cut on the upper limit $\Delta\vartheta_n \cdot \Delta\vartheta < 150$ applied on the simulation data together with all the other cuts discussed before, eliminates most of the residual background (less than 1%) and then no fit are request (fig: 4.13).

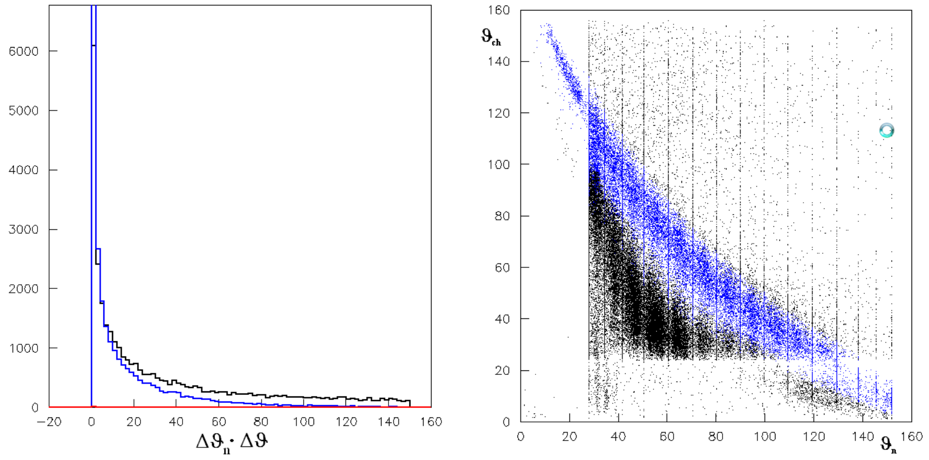

(a) $\Delta\vartheta_{ch} \cdot \Delta\vartheta_n$ (b) ϑ_{ch} versus ϑ_n

Figure 4.13: Figure (a) shows the $(\Delta\vartheta_{ch} \cdot \Delta\vartheta_n)$ distribution for: experimental data (black), simulation of deuteron photodisintegration (blue) and simulation of pion photoproduction (red). Figure (b) shows ϑ_{ch} versus ϑ_n distribution. Blue markers are the event selected by the cut.

4.5 The beam asymmetry

Being N_H and N_V the number of photodisintegration selected events when the polarisation direction of the incoming photon is horizontal or vertical respectively, the following relations can be written:

$$N_H = N_{\gamma_H} N_A \frac{\rho l}{A} \left(\frac{d\sigma}{d\Omega} \right)_{unp} \varepsilon \cdot (1 - P\Sigma(E_\gamma, \vartheta_p) \cos 2\varphi) \tag{4.4}$$

$$N_H = N_{\gamma_V} N_A \frac{\rho l}{A} \left(\frac{d\sigma}{d\Omega} \right)_{unp} \varepsilon \cdot (1 + P\Sigma(E_\gamma, \vartheta_p) \cos 2\varphi) \tag{4.5}$$

where:
N_{γ_H} = number of incoming photon with horizontal polarisation;
N_{γ_V} = number of incoming photon with vertical polarisation;
$N_A = 6,022141 \cdot 10^{23} mol^{-1}$ Avogadro number;
A = mass number (2.014 for deuteron);
ρ = target density ($\rho_D = 0.169 g/cm^3$);
l = target length;
$\left(\frac{d\sigma}{d\Omega} \right)_{unp}$ = differential cross section for the reaction;
ε = detection and reconstruction efficiency;

P = polarisation degree of the photon;
Σ = beam asymmetry.

In order to evaluate the quantity Σ, we can take into account the following relations:

$$\frac{\frac{N_H}{N_{\gamma H}}}{\frac{N_H}{N_{\gamma H}} + \frac{N_V}{N_{\gamma V}}} = \frac{1}{2} \cdot (1 - P\Sigma \cos 2\varphi) \tag{4.6}$$

$$\frac{\frac{N_V}{N_{\gamma V}}}{\frac{N_H}{N_{\gamma H}} + \frac{N_V}{N_{\gamma V}}} = \frac{1}{2} \cdot (1 + P\Sigma \cos 2\varphi) \tag{4.7}$$

They are independent from the efficiency ε, from the target parameters and from the unpolarised differential cross section. For a fixed energy value of the incoming photon and for a fixed diffusion proton angle, known the polarisation degree of the beam, is possible to make a fit of the distributions 4.6 - 4.7 as a function of φ. From the results of the fit, we can estimate the value of the product $P\Sigma$ for each energy and ϑ bin and extract the Σ asymmetry. Figure 4.14 shows the typical cosinusoidal behaviour of the quantities 4.6 - 4.7.

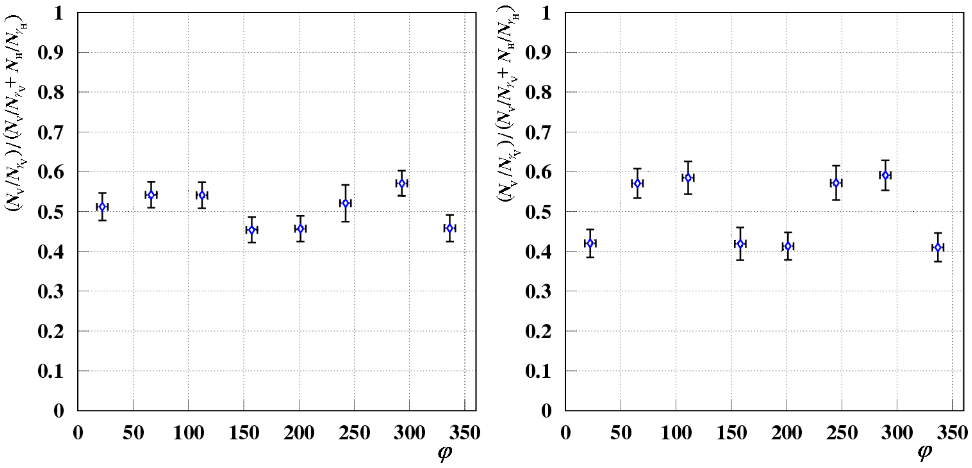

Figure 4.14: The figure shows the distribution of the quantities 4.6-4.7 as a function of φ. The cosinusoidal behaviour clearly appear

Chapter 5

Analysis results

5.0.1 Introduction

We have analysed all the photoreaction data taken from 1999 to 2006 at the GRAAL facility on deuteron target (1061 run). Using the three methods described in the last chapter (par: 4.4.1, 4.4.2, 4.4.3) we have extract the beam asymmetry for 5 energy bins and 4 ϑ_p bins. During the years we have increased the laser energy from the visible line to UV line to explore more high energy region ($E^{\gamma}_{max} \sim 1.5\ GeV$) In order to have enough statistic we have decided to sum both laser line data (UV and visible period) and we estimate the average polarisation degree as explain in the paragraph 4.3.

5.1 Measurament of the beam asymmetry

The analysis described in the previous chapter, allows to determine the number of photodisintegration events (N_V or N_H) for a given polarisation state of incoming photon for a fixed energy, ϑ_p, and φ bin. For each bin we have calculated the ratio:

$$F(E_\gamma, \vartheta_p, \varphi) = \frac{\frac{N_V}{N_{\gamma V}}}{\frac{N_H}{N_{\gamma H}} + \frac{N_V}{N_{\gamma V}}} = \frac{1}{2} \cdot (1 - P\Sigma \cos 2\varphi) \tag{5.1}$$

From the given definition 4.7, we expect that the distribution 5.1 as a function of the azimutal angle, at fixed energy and ϑ proton angle, should show the following behaviour:

$$F(\varphi) = \frac{1}{2}(1 + A\cos 2\varphi), \text{ where } A = P\Sigma \tag{5.2}$$

Using the Paw package, we have fitted the distribution of the experimental data, and we have extracted the parameter $A(E_\gamma, \vartheta_p)$. Thus, known the polarisation average degree for each energy bin, we have determined the value of Σ using the relation:

$$\Sigma(E_\gamma, \vartheta_p) = \frac{A(E_\gamma, \vartheta_p)}{P(E_\gamma)} \tag{5.3}$$

We have done this calculation following the three different analysis already described in the sections 4.4.1 4.4.2 4.4.3. We have then compared the results.

5.2 Results

Figure 5.1-5.3 show some of the fit that we have done for the extraction of the product $P\Sigma$. We also present the result for the Σ beam asymmetry from the three different methods compared 5.4. The results at $\vartheta^p_{cm} = 90°$ are also compared with the previous results of Adamian 5.5.

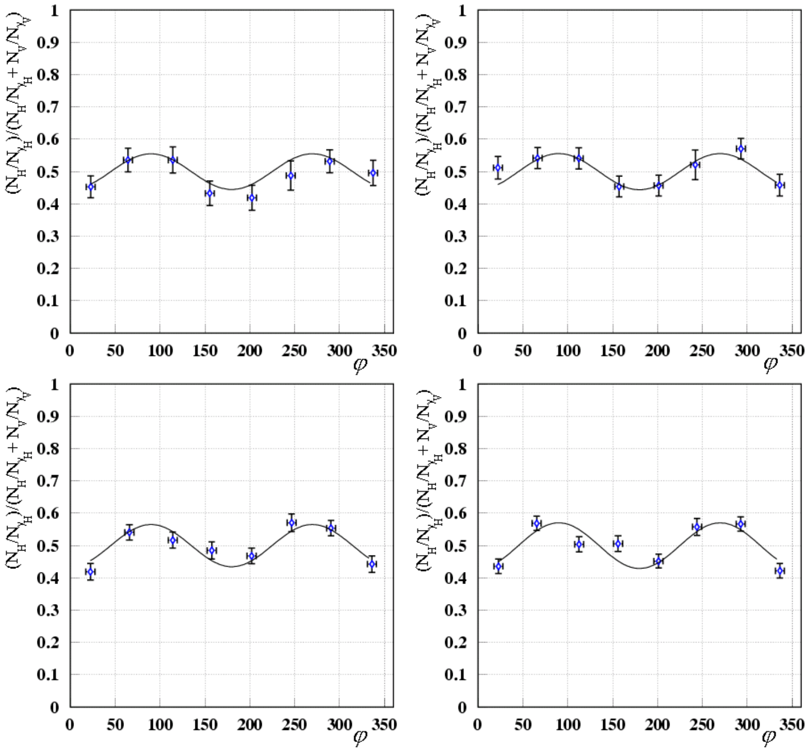

Figure 5.1: The fit for the extraction of the product $P\Sigma$.

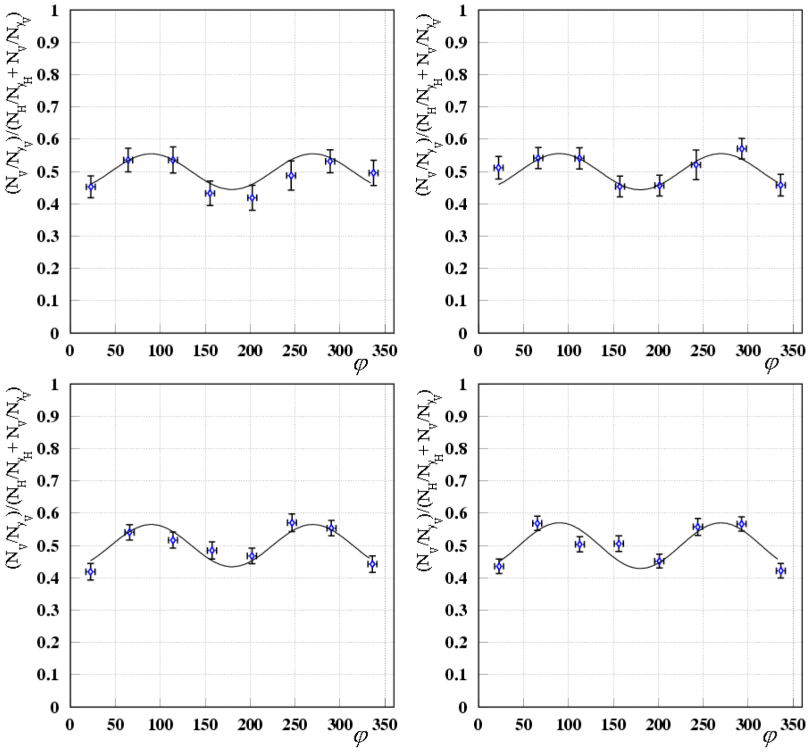

Figure 5.2: The fit for the extraction of the product $P\Sigma$.

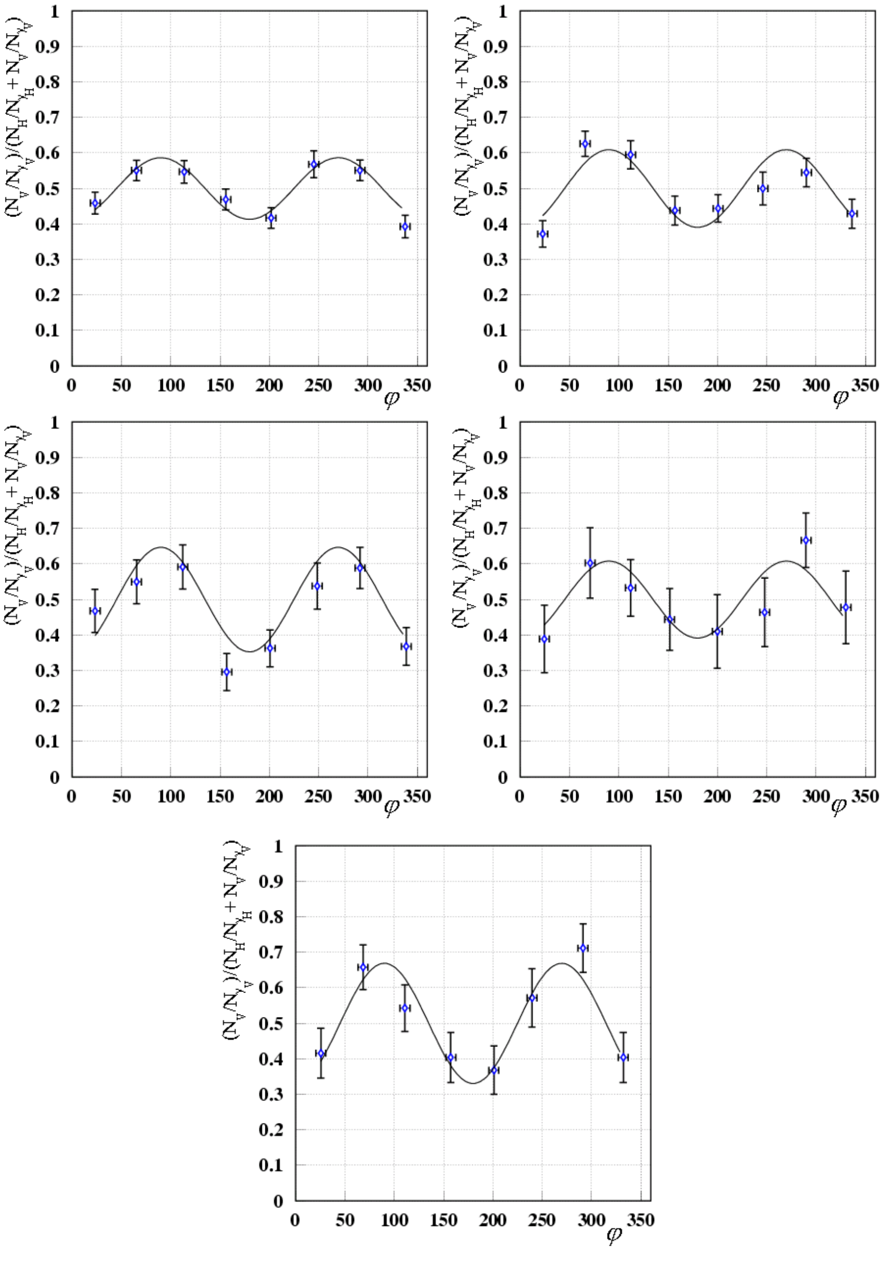

Figure 5.3: The fit for the extraction of the product $P\Sigma$.

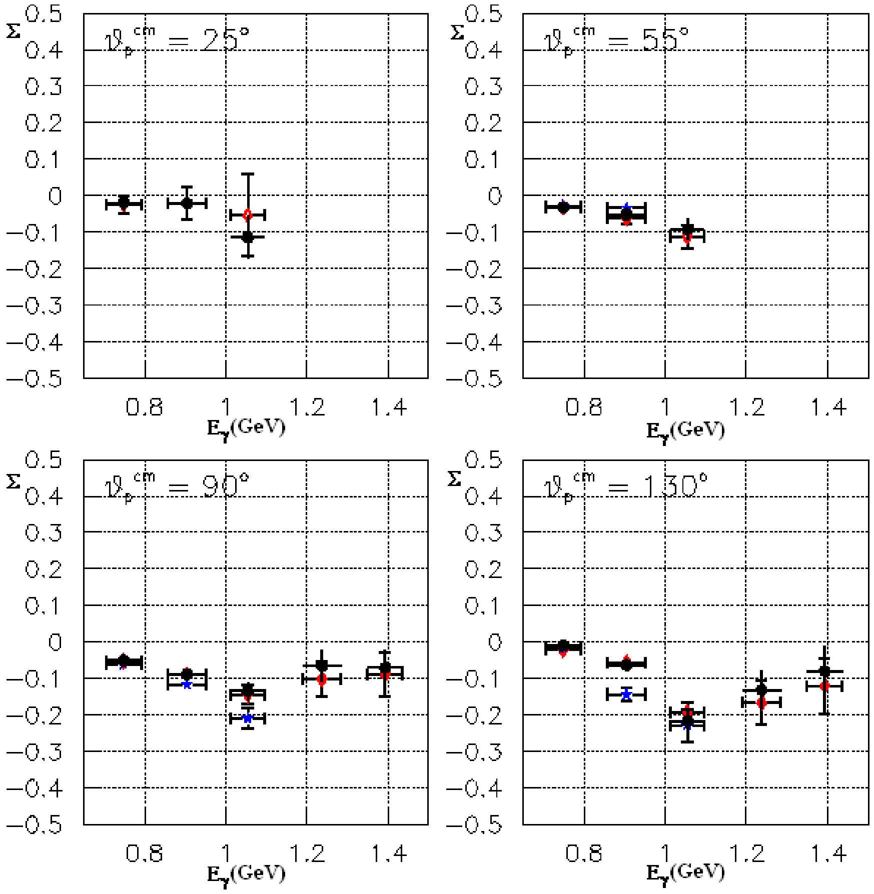

Figure 5.4: The comparison among the results for the Σ beam asymmetry extracted using the three analysis methods:"$\Delta\vartheta$ fit" (blue stars); "$\Delta\vartheta$ cut" (black points); "$\Delta\vartheta_n \cdot \Delta\vartheta$ cut" (red rhombus). The values are compatible in the error bars.

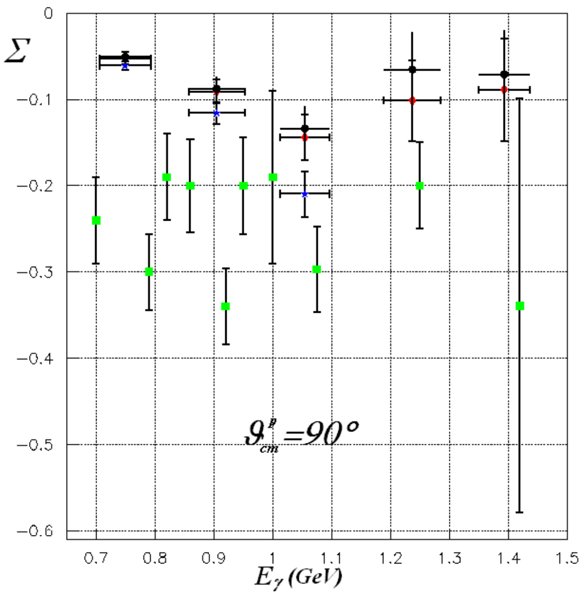

Figure 5.5: Our results compared with the Adamian ones (green squares) for $\vartheta^p_{cm} = 90°$. Our data are: ”$\Delta\vartheta$ fit” (blue stars); ”$\Delta\vartheta$ cut” (black points); ”$\Delta\vartheta_n \cdot \Delta\vartheta$ cut” (red rhombus). There is not agreement among our analysis result and the Adamian work.

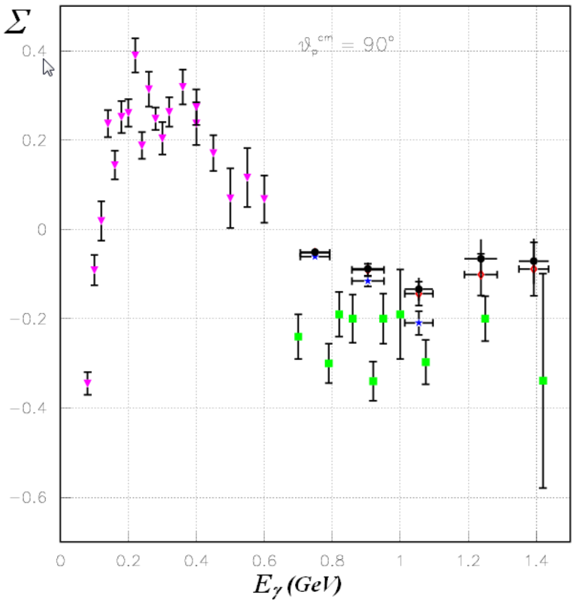

Figure 5.6: Comparing our results with the data existing at $\vartheta^p_{cm} = 90°$ for incoming photon energies below the GRAAL range (violet triangles), clearly appear the better agreement with the trend of the beam asymmetry with respect to the Adamian ones (green squares). Our data are: ”$\Delta\vartheta$ fit” (blue stars); ”$\Delta\vartheta$ cut” (black points); ”$\Delta\vartheta_n \cdot \Delta\vartheta$ cut” (red rhombus). There is agreement only for the data over the Gev region.

5.3 Conclusions

We extracted the Σ beam asymmetry for five energy bins ($E_\gamma = 0.75\,GeV$, $E_\gamma = 0.90\,GeV$, $E_\gamma = 1.05\,GeV$, $E_\gamma = 1.24\,GeV$ and $E_\gamma = 1.39\,GeV$) and for four proton polar angle bin ($\vartheta^p_{cm} = 25°$, $55°$, $90°$ and $130°$) using three different methods. The "$\Delta\vartheta$ fit" works well only in the lowest three energy bins with the proton in the central region because the high statistics allows for a fit. This method provides 9 experimental points for the Σ beam asymmetry. The other 2 method appear to work well in every energy bins for $\vartheta^p_{cm} = 90°$ and $130°$, but only in the lowest three energy bins for $\vartheta^p_{cm} = 25°$ and $55°$. Each of these methods provide 16 experimental point for the Σ beam asymmetry. The results are compared between each other and they point out that the method give value of Σ compatible whitin the error bars.

Our data represent the first measurement for the Σ beam asymmetry in the gamma-ray energy range $0.70\,GeV \leq E_\gamma \leq 1.45\,GeV$ for proton polar angles different from 90°. In this photon energy range the deuteron is undergoing a transition from the region in which conventional hadronic degrees of freedom describe the physics to a region in which quark degree of freedom are more appropriate. Up to now the physics that connect the two region does not exist. For this reason no theoretical calculation are available for the Σ beam asymmetry across the GeV.

Bibliography

[1] J. Chadwick and M. Goldhaber, Nature (1934) 134 237.

[2] H. Bethe, Rev. Mod: Phys. (1999) 71 S6.

[3] J. M. Laget, Nucl. Phys. A 312 265 (1978).

[4] W. Leidemann and H. Arenhövel, Nucl. Phys A 465 573 (1987).

[5] H. Tanabe and K. Ohta, Phys. Rev. C 40 1905 (1989).

[6] T-S. H. Lee , Few Body Syst, Supplement 6 526; Argonne National Laboratory Preprin PHY-6886-TH-91; Argonne National Laboratory Preprin PHY-6843-TH-91.

[7] M. Schwamb and H. Arenhövel, Nucl. Phys. A 690 682 (2001); Nucl. Phys. A 690 647 (2001); Phys. Rev. Lett. B 420 255 (1998).

[8] Y. Kang,, Ph.D. Thesis Bonn (1993).

[9] LEGS Collaboration, Phys. Rev. C 52 1995 R455.

[10] R. Crawford et al., Nucl. Phys. A 603 1996 303.

[11] S. I. Nagoryi, Yu A. Kasatkin, I. K. Kirichenko, Sov. J. Nucl. Phys. 55 189 (1992).

[12] A. E. L. Dieperink, S. I. Nagoryi, Phys. Lett. B 456 9 (1999).

[13] K. Yu Kazakov, S. Shimovsky , Phys. Rev. C 63 014002 (2000).

[14] C. E. Carlson, Nucl. Phys. A 508 481c (1990).

[15] K. Maltman, N. Isgur, Phys. Rev. Lett. 50 1827 (1983).

[16] K. Maltman, N. Isgur, Phys. Rev. D 29 952 (1984).

[17] S. J. Brodky, G. R. Farrar , Phys. Rev. Lett. 31 1153 (1973); Phys. Rev. D 11 1309 (1975).

[18] G. P. Lepage, S. J. Brodsky, Phys. Rev. D 22 2157 (1980); Phys. Rev. D 24 2848 (1981).

[19] V. Matveev,et al., Nuovo Cimento Lett. 7 719 (1973).

[20] S. J. Brodky, J. R. Hiller, Phys Rev. C 28 475 (1983); Phys. Rev. C 30 412(E) (1983).

[21] L. L. Frankfurt, G. A. Miller, M. M. Sargsian, M. I. Strikman; Phys. Rev. Lett. 84 (2000) 3045-3048

[22] L. A. Kondratyuk, et al., Phys. Rev. C 48 2491 (1993).

[23] V. Yu Grishina, et al., Eur. Phys. J A 10 355 (2001).

[24] V. Yu Grishina, et al., Eur. Phys. J A 10 355 (2001).

[25] R. Crawford, et al., Nucl. Phys. A 603 (1996) 303.

[26] J. Napolitano, et al., Phys. Rev. Lett. 61, (1988) 2530.

[27] S.J. Freedman, et al., Phys. Rev. C 48 (1993) 1864.

[28] J. E. Beltz, et al., Phys. Rev. Lett. 74, (1995) 646.

[29] C. Bochna, et al.,Phys. Rev. Lett. 81, (1998) 4776.

[30] E. C. Schulte, et al., Phys. Rev. Lett. 87, (2001) 102302-1.

[31] R. Gilman, et al., CEBAF Experiment E99-008 (1999).

[32] V. G. Gorbenko, Yu. V. Zhebrovskji, et al., Nucl.Phys. A381 330-342 (1982) .

[33] F. V. Adamian, et al., JETP Lett. 39, 239 (1984).

[34] F. V. Adamian, et al., Eur Phys J. A 8, 423-428 (2000).

[35] D. Babusci, L. Casano, A. D'Angelo, P. Picozza, C. Schaerf, and B. Girolami., *Project GRAAL: the Scientific case*. Il Nuovo Cimento Vol. 103 A, N.11.

[36] F. R. Arutyunyan and V. A. Tumanian, Phys. Lett., 4 (1963) 238; Sov. Phys. Us., 83 (1964) 339.

[37] R. H. Milburn, Phys. Rev. Lett., 10 (1963) 75.

[38] V. N. Bayer and V. A. Khoze, Sov. J. Nucl. Phys., 2 (1969) 238.

[39] O. F. Kulikov, et al., Phys. Lett., 13 (1964) 344.

[40] C. Bemporad, et al., Phys. Rev. B, 138 (1965) 1546.

[41] J. Ballam, et al., Phys. Rev. Lett., 23 (1969) 498.

[42] R. Malvano, et al., *Some consideration on the possibility of obtaining a quasi-monochromatic polarised photon beam from laser-electron scattering in the storage ring Adone*. LFN-67/48 (1967).

[43] A. D'Angelo, O. Baralini, V. Bellini, P. Levi Sandri, D. Moricciani, et al., *Generation of Compton backscattering γ-ray beams*. Nucl. Instr. & Meth. A 455 (2000) 1-6.

[44] G. Matone, P. Picozza. D. Prosperi, A. Tranquilli, C. Schaerf, et al., Lect Notes Phys.62 (1977) 149.

[45] D. Babusci, G Giordano, G. Matone *Photon polarization properties in laser backscattering*. Phys. Lett. B 355 (1995) 1-8

[46] V. Bellini, S. Bianco, M. Capogni, B. Girolami, et al., *Experimental study of high-energy resolution lead/scintillating fiber calorimetry in the 600-1200 MeV energy region*. Nucl. Instr. & Meth. Phys. A 386 (1997) 254-258

[47] *The BGO Collaboration Progress Report*. 1990, LFN -90/084(R).

[48] F. Ghio,et al., Nucl. Instr. & Meth. Phys. A 370 396 (1996).

[49] A. D'angelo, R. Di Salvo, V. Bellini, P. Levi Sandri, D. Moricciani, L. Nicoletti, A. Zucchiatti, C. Schaerf, P. Rossi, et al., *The temperature monitor system of a BGO calorimeter*. Nucl. Instr. & Meth. A 403 (1998) 22-30.

[50] D'angelo, R. Di Salvo, V. Bellini, B. Girolami, P. Levi Sandri, D. Moricciani, L. Nicoletti, A. Zucchiatti, C. Schaerf, er *The GRAAL high resolution BGO calorimeter and its energy calibration and monitoring system.* Nucl. Instr. & Meth. A 403 (1998) 71-86

[51] P. Levi Sandri, F. Ghio, A. D'angelo, R. Di Salvo,C. Schaerf, et al., *Performance of a BGO calorimeter in a tagged photon beam from 260 to 1150 MeV.* Nucl. Instr. & Meth. A 370 (1996) 396-402

[52] V. Kouznetsov , et al., *A large acceptance lead-scintillator time-of-flight wall for neutral and charge particles.* Nucl. Instr. & Meth. A (2001).

[53] D. Barancourt, et al., *The data acquisition system for the GRAAL experiment at the ESRF in Grenoble.* Nucl. Instr. & Meth. A 388:226 (1997)

[54] *PAW, Physics Analysis Workstation*, CERN program Library Long riteup, Q121 (1993).

[55] *GEANT, Detector Description an Simulation Tool*, CERN program Library Long Writeup.

[56] P. Corvisiero, et al., *Simulation of Photon-Nucleon Interaction*, Nucl. Instr. & Meth. A346 433 (1994).

[57] *FLUKA*, program Library Long Writeup.

[58] *MIKAP*, program Library Long Writeup.

[59] A. Zucchiatti, et al., Nucl. Instr. & Meth. A452 536 (1999)

[60] V. Breton, et al., Nucl. Instr. & Meth. A362 478 (1995)

[61] R. Hgedorn , *Relativistic Kinematics* W.A. Benjamin inc. (1964)